Title
Chemical Engineering of Nanomaterials for the Delivery of Biomolecular Cargo

Author
Jackson, Christopher

Publication Date
2022

Peer reviewed|Thesis/dissertation

Chemical Engineering of Nanomaterials for the Delivery of Biomolecular Cargo

by

Christopher Tonnu Jackson

A dissertation submitted in partial satisfaction of the

requirements for the degree of

Doctor of Philosophy

in

Chemistry

in the

Graduate Division

of the

University of California, Berkeley

Committee in charge:

Professor Markita Landry, Chair
Professor Matthew Francis
Professor David Schaffer
Professor Ke Xu

Spring 2022

Chemical Engineering of Nanomaterials for the Delivery of Biomolecular Cargo

Abstract

Chemical Engineering of Nanomaterials for the Delivery of Biomolecular Cargo

by

Christopher Tonnu Jackson

Doctor of Philosophy in Chemistry

University of California, Berkeley

Professor Markita Landry, Chair

Nanomaterials have the potential to play a significant role in the development of new biotechnology for diverse applications, including agricultural genetic engineering, biological sensing, nanomedicine, optics, and more. Therefore, a robust, fundamental understanding of their material properties and the techniques to engineer these properties is a key area of scientific interest.

In this dissertation, we explore several key areas where the chemical engineering of nanotechnology, particularly single walled carbon nanotubes (SWNTs), can have a significant impact. We first broadly explore emerging trends in some of the most promising near-infrared luminescent materials and applications. In particular, we focus on how a more comprehensive understanding of their intrinsic material properties might allow researchers to better leverage these traits for innovative and robust applications.

Further, we focus on the ways in which nanomaterials can address some of the most critical challenges of CRISPR genome editing in plants through improvements in cargo delivery, species independence, germline transformation and gene editing efficiency. We identify major barriers preventing CRISPR-mediated plant genetic engineering from reaching its full potential, and discuss ways that nanoparticle technologies can lower or eliminate these barriers.

Next, we present mechanisms to optimize DNA loading on SWNTs with a library of polymer-SWNT constructs and assess DNA loading ability, polydispersity, and both chemical and colloidal stability. We demonstrate that polymer hydrolysis from nanomaterial surfaces can occur depending on polymer properties and attachment chemistries, and we describe mitigation strategies against construct degradation. Given the growing interest in delivery applications in plant systems, we also assess the stress response of plants to polymer-based nanomaterials and provide recommendations for future design of nanomaterial-based polynucleotide delivery strategies.

We then adapt our findings from the development of polymer-SWNTs towards the synthesis of protein-functionalized SWNTs and the covalent attachment of DNA cargo. Specifically, we explore the development of streptavidin-biotin chemistry as a potential alternative to other existing nanoparticle-biomolecule delivery systems and offer exciting opportunities for future research.

Finally, we explore the federal regulatory challenges in the United States that limit scientific innovation and unduly hinder the widespread production of genetically engineered crops, like those we propose to develop throughout this thesis. To address these shortcomings, we propose policy recommendations including the consolidation of federal regulatory communication and a unified web platform for commercial approval applications.

Cho Ông Ngoại

Contents

List of Figures

List of Tables

Acknowledgments

Thank you to my advisor, Markita Landry, without whose guidance none of this would be possible. Beyond her scientific expertise, she has been one of the kindest and most understanding mentors I could have asked for, going above and beyond to encourage my research, professional, and personal growth. I am forever grateful that she took a chance on me.

Thank you to my other dissertation committe members, Professors Matt Francis, David Schaffer, and Ke Xu, for their support and feedback on this work. I am also grateful to my qualifying committee members, Professors Graham Fleming, Junqiao Wu, Kwabena Bediako, and David Limmer, for their support.

This work has greatly benefited from the contributions of many collaborators and financial supporters. Thank you to the team at BASF, including Anne-Marie Kuijpers, Baochun Li, Nadine Kaiser, Katelijn Dhalluim, Derek Drost, Joshua Speros, and Emir Islamovic. Further thanks to our partners at the Carnegie Institution for Science and Lawrence Berkeley National Lab, including Destiny Davis, Tallyta Silva, Purva Karia, Suryatapa Ghosh Jha, William Dwyer, Olivia MacDonald, Daniel Ginzburg, Christine Aquino, David Ehrhardt, Sue Rhee, and Jenny Mortimer. My work has been funded by the National Science Foundation Graduate Research Fellowship Program.

Thank you to the entirety of the Landry Lab for welcoming me and creating an environment that has been a joy to come to every day. This work would not have been possible without the support of every lab member - in particular, thanks to Jeffrey Wang, Natalie Goh, and Eduardo González-Grandío, who have been essential collaborators and teachers during my time in the lab. Additionally, thank you to Sejal Krishnan, who has been an outstanding mentee and contributor to this work.

I would not have made it through graduate school without the support and friendship of so many others. A heartfelt thank you to the members of my cohort, without whom I would not have survived my first semester of classes or qualifying exams. I have also been lucky to find many communities across campus and beyond who have inspired and fulfilled me over the past several years. In particular, thank you to the Berkeley Energy and Resources Collaborative, Science Policy Group at Berkeley, National Science Policy Network, Engineers & Scientists Acting Locally, and the Asian American and Pacific Islander Standing Committee for an abundance of friendships and opening my eyes to a whole new world of possibilities beyond the bench.

A heartfelt thank you to the many friends who have helped me throughout graduate school. In particular, thank you to Brandon Smith for dragging me out of the lab for much-needed runs and pastries, and to Alissa Barber, for being a daily source of joy and friendship.

Most importantly, words cannot express my gratitude for my family, especially my parents, Raymond Jackson and Thuthu Tonnu, and my grandparents. Their unwavering support throughout the ups and downs of graduate school and their sacrifices throughout my life have made it possible for me to pursue a PhD.

Chapter 1

Engineering near-infrared luminescent materials

1.1 Chapter abstract

Near-infrared (NIR) luminescent materials have emerged as a growing field of interest, particularly for imaging and optics applications in biology, chemistry, and physics. However, the development of materials for this and other use cases has been hindered by a range of issues that prevents their widespread use beyond benchtop research. This chapter explores emerging trends in some of the most promising NIR materials and their applications. In particular, we focus on how a more comprehensive understanding of intrinsic NIR material properties might allow researchers to better leverage these traits for innovative and robust applications in biological and physical sciences.

1.2 Introduction

The search for new luminescent materials that emit in the NIR region, from ~700 to 2500 nm, has rapidly expanded in recent years. In contrast to their counterparts that emit at shorter wavelengths, mostly in the visible spectrum, NIR emissive materials possess a number of unique advantages. NIR light can penetrate biological tissues with minimum interference due to reduced absorption and scattering by tissues, such as skin and blood, in this wavelength range[1]. Further, because water absorbs in the visible spectrum, NIR emissive materials enjoy enhanced bioimaging capabilities[2]. In principle, the energy involved with the generation and decay of excited species in NIR emission is much smaller than for UV or visible emission[3], which limits the number of side reactions that may take place, increasing the expected stability of NIR materials and devices. Materials that absorb and emit in the NIR region

Chapter 1 is reproduced from work previously published as Jackson, C. T.; Jeong, S.; Dorlhiac, G.F.; Landry, M. P. Advances in engineering near-infrared luminescent materials. iScience 2021, 24 (3), 102156. https://doi.org/10.1016/j.isci.2021.102156.

can be used for inexpensive laser diode excitation, as photodetectors, and as optical sources themselves. Collectively, these properties allow for a diverse range of potential applications, including biological imaging, therapy, communications, and display technologies.

However, there remain a number of outstanding problems that hinder the applicability of these NIR materials outside of laboratory conditions, particularly *in vivo*. Typically, these materials have suffered from poor stability, low quantum yield, and limited tunability; a brief comparison of these challenges, alongside other material properties across different NIR materials, is provided in Table 1.1. Solutions to these problems are necessary for the deployment of NIR-emitting materials in commercial applications and for broader in-laboratory use and therefore this remains an area of ongoing research. As these tools are used by a growing and diverse community of researchers, it is critical to examine the underlying chemistry and physics that enable their successful development and deployment. A better understanding of these intrinsic material properties, particularly across different types of NIR-emitting materials, will ultimately drive research toward new applications.

Here, we explore the photophysics of NIR emission in organic dyes, carbon nanomaterials, inorganic nanoparticles, and proteins, with a focus on how NIR emitters can be tailored to overcome new challenges faced by the NIR research community. We further examine the opportunities to apply NIR-emitting materials in light sources and detection to enable the next generation of optoelectronic devices.

1.3 Organic dyes

Organic dyes that are optically active in the NIR region of the electromagnetic spectrum have a longstanding history of use in imaging, targeting, and treatment in biological systems. Upon excitation by an energy source, electrons transition from the highest occupied molecular orbital (HOMO) to the lowest unoccupied molecular orbital (LUMO). By tuning the length of the unsaturated carbon chains and the makeup of chemical groups that act as electron sinks within the dye, electrons can be delocalized to tune the light that is emitted following this excitation (Figure 1.1).

Therefore, to achieve emission in the NIR, it is necessary to develop dyes with intramolecular π-conjugated systems and substituent electronic effects[4]. High energy absorption and emission (300–600 nm) can be attributed to π-π^* and n-π^* transitions of conjugated structures, whereas lower energies (600–1400 nm) are typically due to intramolecular charge transfer between peripheral donors[5]. Small molecule organic dyes are particularly useful due to their well-defined and tunable structures; here we will focus on four categories: cyanine, donor-acceptor-donor (D-A-D), aza-BODIPY, and EXC dyes (Figure 1.2).

Cyanine

Cyanine-based dyes have been used extensively in bioimaging, with indocyanine green (ICG) being an NIR dye with emission at ˜830 nm clinically approved by the FDA since 1959;

Table 1.1: Comparison of properties of NIR luminescent materials.

Material	**Size**	**Absorption spectrum**	**Absorption coefficient (M^{-1} cm^{-1})**	**PLQY (%)**	**Photo-stability**	**Fluorescence wavelength tunability**	**Lifetime**
SWNT	>0.1 μm (length), ˜1 nm (diameter)	Discrete bands	$>10^7$	0.01-0.1	+++++	High[a]	10-100 ps
La NP	10-50 nm	Discrete bands	10^3-10^4	1-30	+++++	Low	μs-ms
˜QD	2-10 nm	Broad bands	10^5	1-100	+++	High	ns-μs
Organic dye	˜1 nm	Discrete bands	10^5	0.3-6	++	Medium	0.1-100 ns
Protein	1-3 nm	Discrete bands	10^4-10^5	4-14	++	Low	˜0.5-1 ns

[a]Fluorescence wavelength is determined by chirality of SWNT; however, chirally pure SWNT has not been fully established commercially.

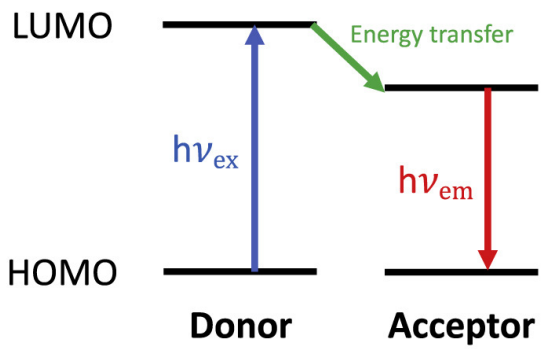

Figure 1.1: Modulation of the HOMO-LUMO gap via tuning of molecular structure.

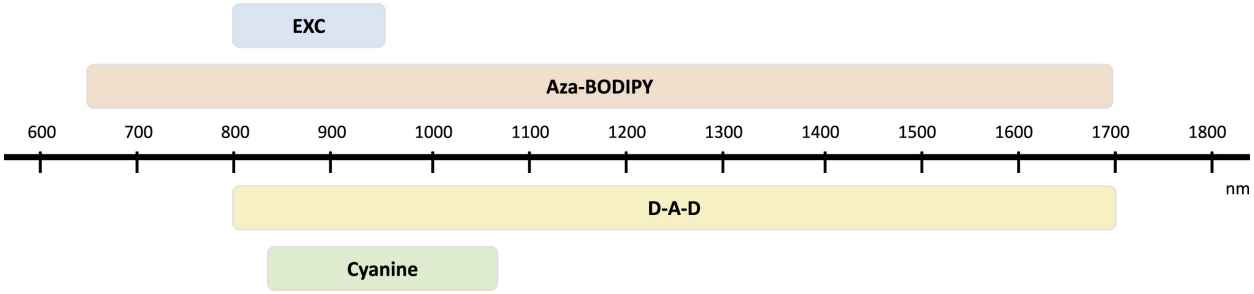

Figure 1.2: Schematic illustrating the reported tunable emission wavelength range of various classes of organic dyes.

however, ICG suffers from low quantum yield (QY) in aqueous solution, poor stability, rapid clearance, and cytotoxicity[6,7]. To address these issues, while drawing from the ICG structure that affords a high absorption coefficient, recent cyanine dyes use a polymethine scaffold, consisting of heterocycles linked by a methine chain[8]. Traditional cyanine dyes have spanned the visible and NIR-I region by increasing the length of the methine chain. Cosco et al. demonstrated that by using a 7-dimethylamino flavylium heterocycle, the emission of these cyanines can be controllably red-shifted even further, to 1064 nm[8,9]. Other work has similarly drawn from the ICG structure to develop polymethine dyes with absorption and emission in the NIR-II region. Whereas ICG absorbs and emits in the NIR-I region, substitution of the nitrogens in the ICG structure for oxygens leads to NIR-I excitation and NIR-II emission; substitution with sulfurs leads to both excitation and emission in the

NIR-II region[10].

To address issues of low QY, a rigid molecular structure can be adopted to minimize nonradiative decay. Li et al. demonstrated that modifying the ICG structure with a conjugated methine chain and cyclohexene and sulfonic groups could enhance its water solubility and stability. This yielded a dye (FD-1080) with a QY of 0.31% (increased to 5.94% in fetal bovine serum) that can be excited at 1064 nm and emitted at 1080 nm (Figure 1.3)[11]. This excitation in the NIR-II region allows for deeper penetration depth and higher resolution *in vivo* imaging due to reduced tissue scattering. Dyes adopting this structure have also demonstrated greater chemical stability in aqueous solutions and improved photostability compared with ICG[12].

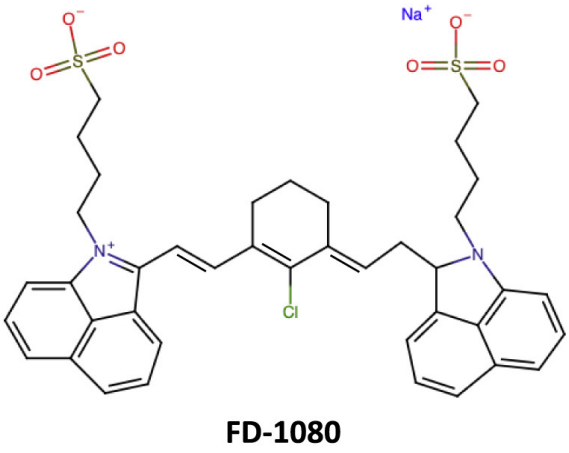

Figure 1.3: FD-1080 cyanine dye.

Attempts have been made to extend these dyes to excitation and emissions at longer wavelengths by lengthening the polymethine chain. Although this approach does increase the wavelength of emission, it also typically causes significant solvatochromic quenching in polar solvents, limiting their use in bioimaging applications[13]. Therefore, more work is needed to generate red-shifted dyes with high QYs in polar environments through methods such as enhancing the donor strength of the molecule's heterocycles, branching the polymethine chain, or engineering the charge of the π-π-system.

D-A-D

Donor-acceptor-donor (D-A-D) type small molecule fluorescent dyes offer another mechanism to tune the band gap of π-conjugated semiconductors and achieve NIR optical properties. Antaris et al. reported the first use of this structure to synthesize CH1055, a water soluble

PEGylated NIR-II fluorophore with a molecular mass of 8.9 kDa and emission at 1055 nm[14]. However, this reduced band gap often leads to increased interactions between the dye's conjugated backbone and other molecules, causing aggregation and quenching fluorescence QY. To address this problem, Yang et al. added a dialkyl fluorene as the shielding unit to synthesize IR-FEP, a pegylated shielding unit-donor-acceptor-donor-shielding unit (S-D-A-D-S) structure with BBTD as the acceptor and EDOT (3,4-ethylenedioxythiophene) as the donor (Figure 1.4a)[15]. These additions enabled tunable NIR absorbance (Figure 1.4b) and increased QY to 2% in aqueous solution, from the previous 0.4% QY of the shielding unit-free counterpart.

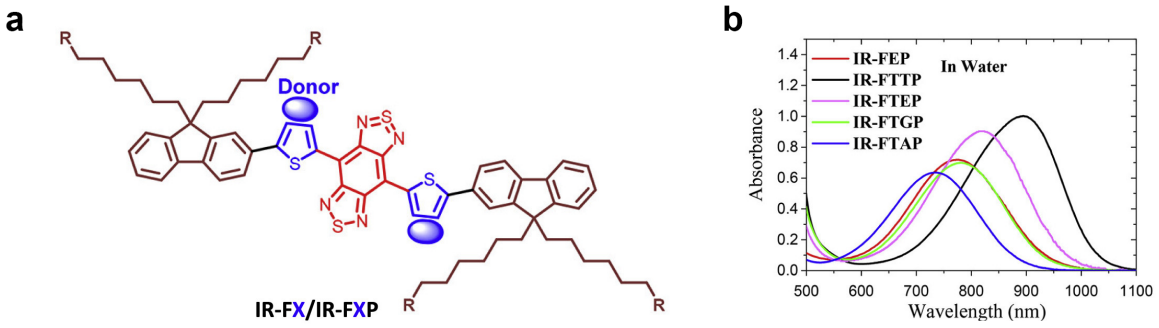

Figure 1.4: D-A-D dye. **(a)** D-A-D dye with shielding units. **(b)** Absorbance spectra of PEGylated D-A-D fluorophores in aqueous solution. Reproduced with permission[16]; copyright 2016, American Chemical Society.

Adopting this S-D-A-D-S structure, subsequent work has explored donor engineering to enhance fluorescence performance[16]. By using octylthiophene as the first donor, the bulky, hydrophobic group causes a larger distortion of the conjugated backbone and fewer interactions with surrounding water molecules. At the same time, thiophene is used as the second donor, increasing the conjugation length and red-shifting the fluorescence emission to 1048 nm with a QY of 5.3% in aqueous solution.

To broaden NIR applications, particularly for multiplexed imaging, it is necessary to increase the number of fluorescent channels available with non-overlapping emission spectra. Zhu et al. have developed a clickable organic fluorophore and a carbon nanotube fluorescent agent conjugated to molecularly specific proteins or antibodies that can be purified through density gradient ultracentrifugation separations[17]. This approach enabled multicolor biological imaging in the 800 to 1700 nm NIR window with a QY of 1.9% in aqueous solution. Future work, particularly for multiplexed imaging, must focus on constructing molecular dyes with higher QYs, narrow emission wavelengths, and large Stokes shifts.

aza-BODIPY

Aza-dipyrromethene boron difluoride (aza-BODIPY) dyes represent another class of NIR emitters with unique optical properties and sufficient water solubility for *in vivo* imaging applications. Although commercially available aza-BODIPY dyes emit in the NIR-I region (650–1000 nm), Bai et al. have reported molecular engineering techniques using aza-BODIPY as an acceptor (A) and strong electron-donating groups as donors (D) to create a strong D to A intramolecular charge transfer effect that red-shifts their emission to the NIR-II window (1000–1700 nm) (Figure 1.5a)[18]. Parallel work by Godard et al. has reported a strategy to introduce ammonium atoms onto the central boron atom of aza-BODIPY, creating a water-soluble NIR-II fluorophore that was used for in vitro and *in vivo* tumor imaging in mice (Figure 1.5b)[19]. These BODIPY-based dyes are also significantly easier to synthesize than cyanine and D-A-D based structures, presenting the possibility of further design to improve their quantum yield.

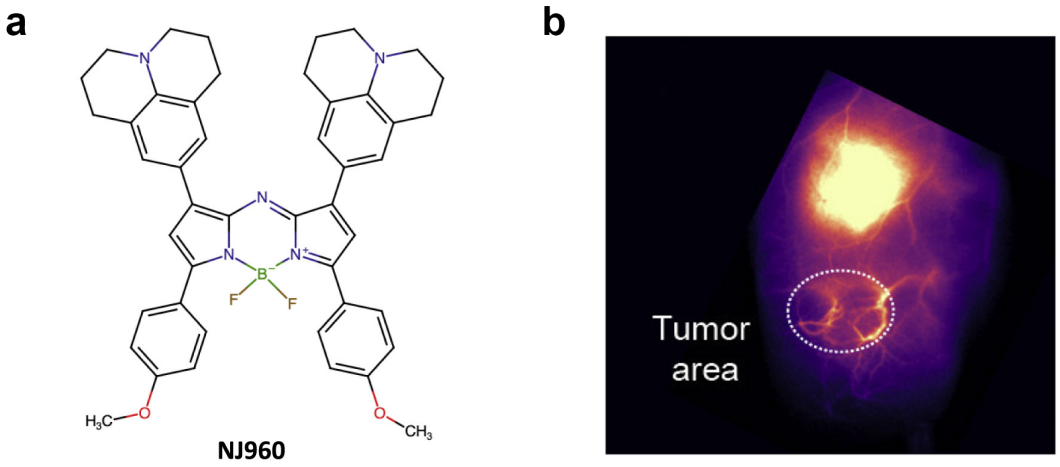

Figure 1.5: aza-BODIPY dye. **(a)** aza-BODIPY dye molecular structure. **(b)** NIR-II image of a mice tumor after intravenous injection of an aza-BODIPY based dye[19]; copyright 2020, American Chemical Society.

EXC

EXC dyes, a new family of NIR fluorescent dyes with absorption and emission in the NIR region (abs. 880 nm, em. 915 nm), are able to mitigate some of the challenges that other small molecular dyes have typically faced[20]. EXC dyes are based on a bisbenzo-C-rhodamine unit modified with a diphenyl ether moiety through spiro linkage. This bulky diphenyl ether

group sterically hinders the rotational freedom of the molecule, preventing undesirable non-radiative quenching. Lei et al. have also demonstrated post-synthetic modifications attaching different chemical handles or functional groups that allow tuning of the quantum yield above 10% in organic solvents and 1.4% in aqueous solution (Figure 1.6)[20].

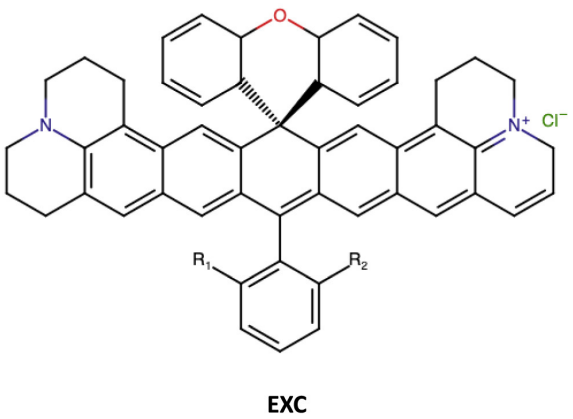

Figure 1.6: EXC dye.

1.4 Carbon nanomaterials

Given the challenges associated with fluorescent organic dyes, in recent years a growing interest in alternative luminescent materials has emerged. In particular, carbon-based nanomaterials demonstrate a resistance to photobleaching, enabling their use in a wider variety of imaging techniques over long timescales, while sometimes offering additional improvements in luminescence brightness[21]. To improve the applicability of carbon-based nanomaterials in bioimaging, techniques have been developed to coat carbon nanomaterials with polymers such as polyethylene glycol to produce materials that are both bright and biocompatible[22]. Here we highlight single-walled carbon nanotubes (SWNTs) and carbon dots as two promising candidates for highly stable and tunable NIR-emitting materials.

Single-walled carbon nanotubes

SWNTs are quasi-one dimensional structures that can be conceptualized as the rolling of a graphene sheet (Figure 1.7a). Their unique optical properties, particularly their NIR emission (˜700–1800 nm), arise from Van Hove singularities in their electronic density of states that can be tailored by the tuning of the nanotube's chiral angle (Figure 1.7b) and electronic contributions of molecules bound to their surface[23,24]. The absorption peak wavelength of

a SWNT varies with the mean tube diameter, whereas the absorption spectral bandwidth is dependent on the nanotube diameter distribution[25]. SWNTs offer unique advantages for imaging, including no blinking or photobleaching and further chemical tunability through adsorption of ligands *via* π-π stacking interactions. However, recent research still seeks to understand how biological environments impact SWNT physicochemical properties to reach the levels of biocompatibility achieved by NIR-emitting organic dyes and proteins[23,26].

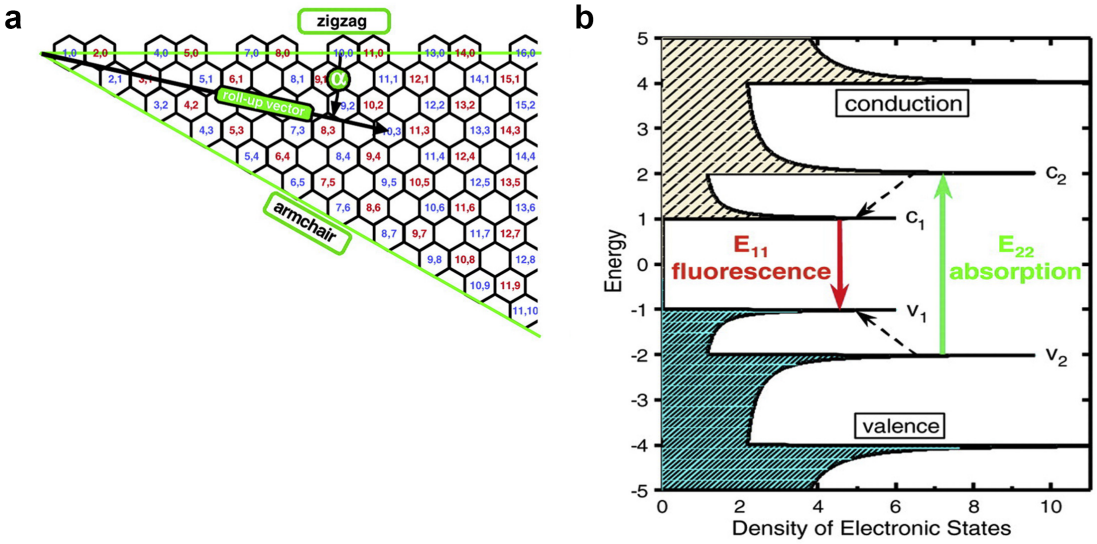

Figure 1.7: Single walled carbon nanotube structure. **(a)** Schematic showing the formation of different chirality carbon nanotubes obtained by rolling a graphene sheet from different lattice points. **(b)** Schematic electronic density of states for a single carbon nanotube, where E_{11} fluorescence can be modulated via the tuning of the nanotube's chiral angle[24]; copyright 2002, The American Association for the Advancement of Science.

Chirality-dependent emission

SWNT chirality gives rise to chirality-specific physical and optical properties, providing a distinct spectroscopic signature for each chirality (Figure 1.8)[23]. Generally, chirality-pure SWNT samples have singular excitation and emission maxima, enabling single-chirality SWNTs to be used as monochromatic fluorescent reporters for infrared imaging. (6,5) chirality-pure SWNTs are particularly desirable for bioimaging applications due to their increased brightness compared with mixed-chirality SWNTs and their relative ease of purification compared with other chiralities[27–29]. However, purification of individual SWNT chiralities from the multi-chirality mixtures resulting from their synthesis can be challenging. Recent approaches to SWNT chirality purification have identified techniques, referred

to as a corona phase exchange purification (CPEP) using polyfluorene polymers to enrich certain SWNT chiralities, which can then be redispersed in desired organic phase[30]. The authors demonstrated that these chirality-pure SWNTS could be further dispersed in water by exchanging the surface functionalizations to aqueous soluble surfactants or polymers, thus enabling their broader use in applications such as bioimaging.

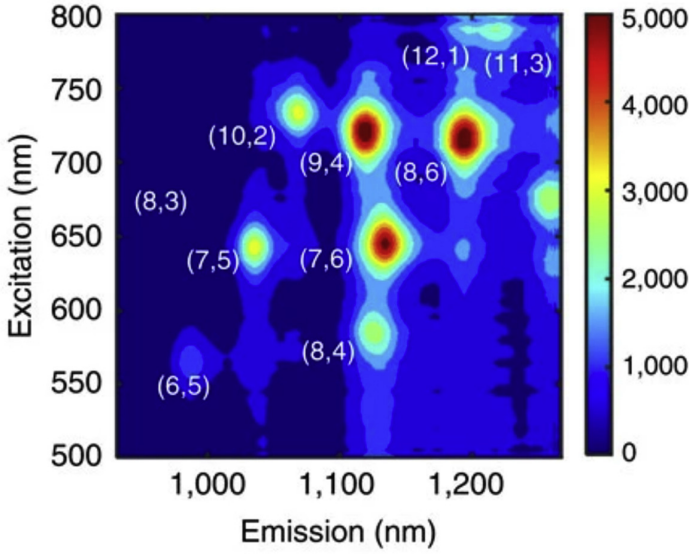

Figure 1.8: Excitation-emission profile of a mixed chirality DPPE-PEG(500)-wrapped SWNT solution[31]; copyright 2016, Springer Nature.

Given the strong dependence of SWNTs on their local dielectric environment, multiple studies have explored the effect of SWNT chirality and SWNT fluorescence on their interactions with biomolecules, particularly DNA, and subsequent changes in fluorescence. Early work by Heller et al. demonstrated the ability to transduce the conformational rearrangement of a bound DNA molecule on the SWNT surface while at the same time modulating the SWNT's dielectric environment and decreasing NIR emission by up to 15 meV[32]. Salem et al. found that different single-stranded DNA sequences, particularly $(TAT)_4$ and $(ATTT)_3$, formed DNA-SWNT hybrids with chirality-dependent fluorescence responses to various analytes[33]. Similar studies have found that for $(GT)_6$, a common DNA sequence used to suspend SWNTs for optical sensing, the stability of constructs depends on molecular interactions between the DNA sequence and specific SWNT chirality, not DNA sequence length or chirality[34]. This chirality dependence has been applied to SWNT sensors for dopamine using NIR-II excitation and fluorescence with a quantum efficiency of 0.23%. These sensors show chirality-dependent responses for dopamine with fluorescent turn-on responses between 20% and 350%[35].

Defect-oriented emission

SWNT defects, traditionally viewed as detriments to NIR optical applications, have recently gained new attention as an exciting field of research for fluorescence tunability[36]. Although most defect engineering is limited by chemistries only possible in aqueous solution, recent progress has been made toward new methods using organic solvents. One of the first reports showing chemical control of defect quantum states in SWNTs demonstrated emission from aryldiazonium defects brighter than that of the pristine SWNTs. This emission is tunable by as much as 254 meV by attachment of electron-withdrawing substituents; QY increased exponentially as a function of the shifted emission energy and reached up to 16%, one of the brightest reports of SWNTs in water[37].

More recently, SWNT defects have been harnessed to tailor excitonic behavior through molecular engineering of covalently attached surface functional groups. Kwon et al. demonstrated the use of alkyl and aryl defects to tune fluorescence through their inductive electronic effect. Although the quantum defects trap excitons at a localized potential well, the SWNT serves as an antenna to harvest light and channel excitons to the defect site, where excitons recombine and give off NIR emission dependent on the tailored functional group (Figure 1.9)[38]. These arylated SWNTs can also be tailored for use as pH sensors; the authors demonstrated that switching between protonated and deprotonated states of an attached amine modified its defect state, producing energy shifts that were sensitive to pH changes as small as 0.2 pH units over a pH range of 4.5–8.5[39]. As subsequent studies showed, excitons trapped at defect sites are not subject to diffusion-limited contact quenching, allowing for radiative relaxation and red-shifted emission. By tuning the defect density, Berger et al. reported enhanced QY up to 4%[40]. Recent research has also used quantum defects for modular anchors for both the attachment of nanobodies (such as peptides and proteins) and the synthesis of peptides directly on the SWNT surface, enabling further tuning of their photophysical properties[41].

Nonlinear optical properties

The nonlinear optical properties of SWNTs include saturable absorption, two-photon absorption, modulation depth, and optical limitations of decreased transmittance under high-intensity illumination[42]. These properties can be traced to the basis of SWNT structure, the cylindrical wrapping from a graphene sheet, transitioning from a 2D topology to a quasi-1D topological structure. This reduced dimensionality leads to a quantum confinement of the π-electron wavefunction in the radial and circumferential directions, contributing to a delocalized π-electron system confined by a quasi-1D structure (Figure 1.10)[42].

Using Z-scan and pump-probe spectroscopy across 600–2400 nm, Xu et al. demonstrated the mapping of nonlinear absorption properties across a broad spectral range. Their spectral results indicate that saturable absorption occurs across the visible and near-IR range, with a cutoff within the semiconducting S_{11} band that indicates the role of photoinduced effects in addition to physical effects such as Pauli blocking[43,44]. Other recent studies suggest that

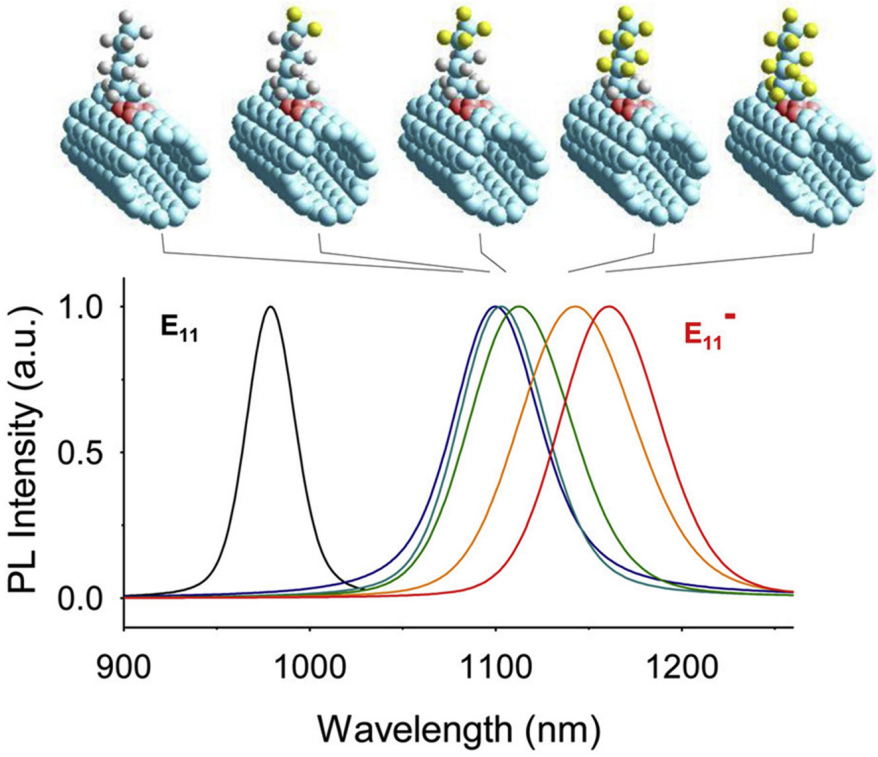

Figure 1.9: Tunable photoluminescence (PL) spectra of (6,5)-SWNTs functionalized with six-carbon alkyl chains with increasing numbers of fluorine substituents[38]; copyright 2016, American Chemical Society.

nonlinear photoemission is a result of optical-field-driven electron tunneling from the valence band; therefore, emission nonlinearity can be tuned by engineering the SWNT band structure through techniques such as controlling the SWNT chirality and doping level[45].

Carbon dots

Carbon dots are quasi-spherical fluorescent nanoparticles consisting of sp^2 carbon atoms and sp^3 carbon atoms at edge planes with dimensions less than 10 nm in diameter. Graphene quantum dots are a subset of carbon dots with higher crystallinity and fewer defects[46]. Fluorescent carbon dots usually emit in the UV and visible spectrum; however, recent advances in their fabrication have enabled fluorescent carbon dots emitting at over 1000 nm. Tang et al. demonstrated the microwave-assisted hydrothermal synthesis of nitrogen-doped graphene quantum dots with broadband photoluminescence from deep UV to NIR wavelength upon excitation with 808 nm light[47]. The unusual NIR emission from graphene quantum dots

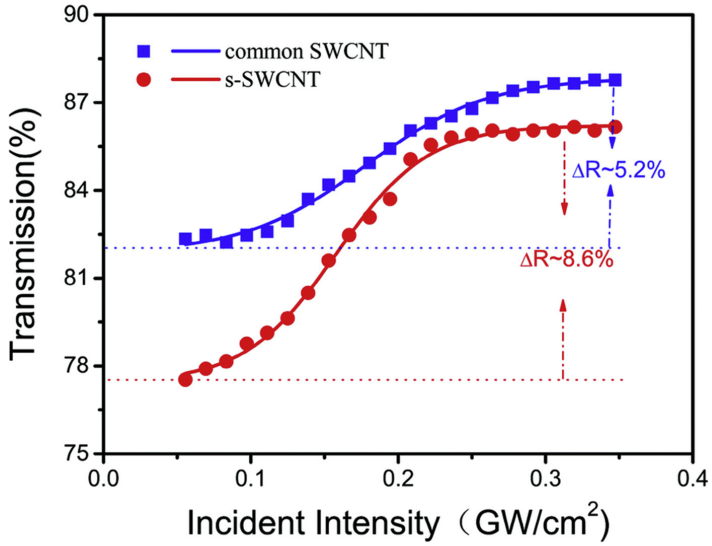

Figure 1.10: Nonlinear transmission versus the incident intensity for samples of mixed and pure-semiconducting SWNTs[42]; copyright 2019, Royal Society of Chemistry.

likely originates from the conjugated electrons in their layered structure. More recently, Li et al. reported the fabrication of NIR-emitting carbon dots from watermelon juice *via* a hydrothermal method. These carbon dots exhibited NIR emission from 900 to 1200 nm with a decent quantum yield of 0.4%[48]. Similar to previous reports, these carbon dots had a quasi-spherical structure with diameters less than 10 nm and consisted of oxygen- and nitrogen-related functional groups[47].

1.5 Inorganic nanoparticles

Compared with their organic counterparts, inorganic nanoparticles can benefit from a wide variety of useful properties, including non-toxicity, hydrophilicity, biocompatibility, and high stability. In recent years, quantum dots and lanthanide nanoparticles have emerged as two particularly exciting candidates for use as tunable and highly luminescent NIR emitters.

Semiconductor quantum dots

The optical properties of semiconductors are determined by excitons (excited hole-electron pairs) that have an intrinsic Bohr radius where the kinetic energy and Coulombic potential are ideally balanced. When the dimensions of a semiconductor are similar to or smaller than

its Bohr radius, the excessive Coulombic potential results in a quantum confinement effect. This principle forms the basis of quantum dots (QDs). In the quantum confinement regime, energy levels are quantized to discrete values and the band gap of a QD depends on its size; specifically, the band gap increases when the size decreases (Figure 1.11a). QDs usually range in size from 2 to 10 nm and consist of 100 to 100,000 atoms in a single particle. The band gap energy and emission wavelength of QDs can be easily tuned by adjusting their size, where the broad absorption profile of the QD enables wavelength-independent excitation of QDs. In comparison to other NIR fluorophores, QDs have advantages such as a broad absorption spectrum, high PL QY, large Stokes shift, and excellent band-gap tunability.

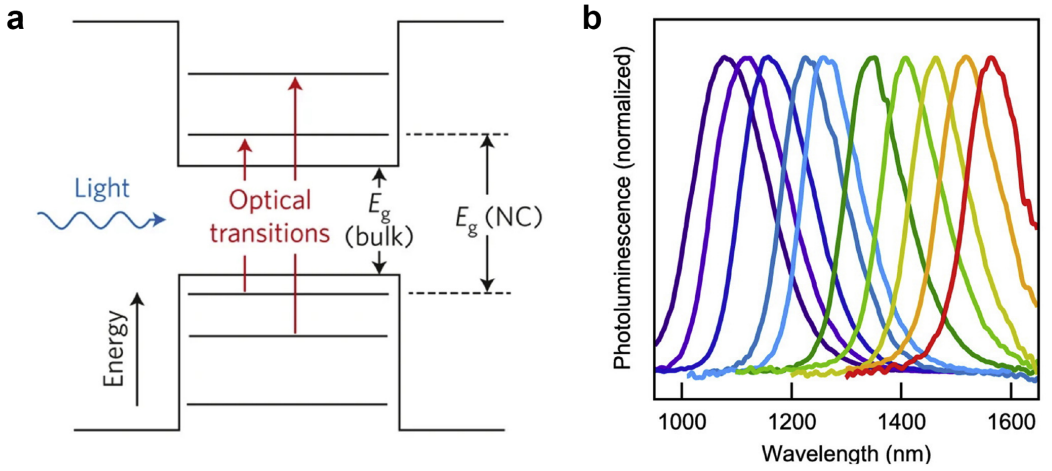

Figure 1.11: Quantum dot tunability. **(a)** Energy diagram of QDs with tunable band gap. **(b)** Tunable NIR PL wavelength of PbS QDs by size control[49]; copyright 2014, American Chemical Society.

Types of NIR-emitting QDs

In the last decade, research on NIR-emitting QDs has focused on metal chalcogenides. QDs composed of lead chalcogenides such as PbS have exhibited decent NIR absorption and emission capabilities in photovoltaic devices. The emission spectra of PbS QDs are extensively tunable in the range of 900–2000 nm by adjusting their size (Figure 1.11b)[49]. The emission wavelength of NIR-emitting QDs can be easily tuned by controlling their size, which enables outstanding multispectral characteristics among current NIR emitters. The high monodispersity and gaussian-like emission spectrum of QDs enables narrow absorption and emission peaks that have half-width at half maximum values in the ranges of 20–40 meV. Due to their extensive study, high-quality synthesis techniques exist that can improve their monodispersity (standard deviation of the QD size distribution ˜4%) and brightness (up to

100% QY)[50]. The chemical stability of PbS QDs can be improved by using an inorganic protective shell such as a CdS/ZnS multi shell structure, which further increases PL QY by passivating defect states[51]. However, medical applications of QDs are limited by concerns about the potential leakage of Pb, a heavy metal ion. Although some researchers report minimal cytotoxicity up to several months in mice, the biocompatibility of Pb-based QDs warrants further investigation[52].

Ag_2S QDs can enable NIR imaging and are known to have higher biocompatibility due to the absence of heavy metal ions in their composition, lending themselves to various applications ranging from bioimaging probes to NIR-emitting devices[43,44]. The emission wavelength of Ag_2S QDs is tunable from 500 to 1200 nm *via* size control. However, the chemical instability of Ag_2S QDs often results in their structural and optical deterioration under light and redox conditions. Although deterioration might be ameliorated by the fabrication of an inorganic protective shell, this approach has not been fully investigated for Ag_2S QDs. Recently, femto-second laser pulsing of Ag_2S dots prompted the transformation of Ag-Ag_2S heterodimers to highly fluorescent Ag_2S superdots that contain protective AgCl outer shells (Figure 1.12)[53]. This transformation results from the fast dissolution of Ag nanoparticles and subsequent reaction between Ag atoms and Cl atoms from chloroform solvent to passivate the Ag_2S dots with the AgCl shell. Using ultrafast illumination of 50 fs pulses drastically reduces surface-related non-radiative processes and leads to an increased QD PL QY of up to 10% and a longer fluorescence lifetime in this Ag_2S system.

As the most recently reported composition of NIR QDs, InAs QDs have been introduced as bright and photostable NIR QDs with a tunable emission spectrum (1000–1400 nm). Bright and photostable InAs-based QDs such as InAs/CdSe/CdS core/shell/shell QDs have been synthesized by continuous injection synthesis. The QY of InAs-based QDs have reached 30% in aqueous solution with PL lifetimes of 100 ns, enabling in vivo whole body imaging with >50 frames per second and negligible background signal (Figure 1.13)[54]. Furthermore, InAs-based QDs show high PL QY in aqueous environments relative to other QDs. However, the long-term toxicity of InAs-based QDs needs to be studied further before consideration of their use in humans.

Controlling blinking and quantum yield

Among all NIR fluorescent emitters, including organic dyes, carbon nanomaterials, and lanthanides, QDs have shown the highest QY (up to 100%). The PL lifetime of NIR QDs is usually 10 ns–1 μs, longer than organic dyes and SWNT and shorter than lanthanide-doped nanomaterials (Table 1.1)[52]. Because QDs have such a high surface-to-volume ratio, the radiative recombination of excitons in QDs (closely tied to QY), is highly dependent on their surface states. To maximize QY, it is necessary to use inorganic and organic protective layers to minimize surface trap sites such as nonstoichiometry and dangling bonds[55].

QDs exhibit a unique blinking behavior, where photoluminescence stochastically fluctuates on a timescale ranging from milliseconds to tens of seconds. The widely accepted explanation for this phenomenon is that a transient charged state is created by illumina-

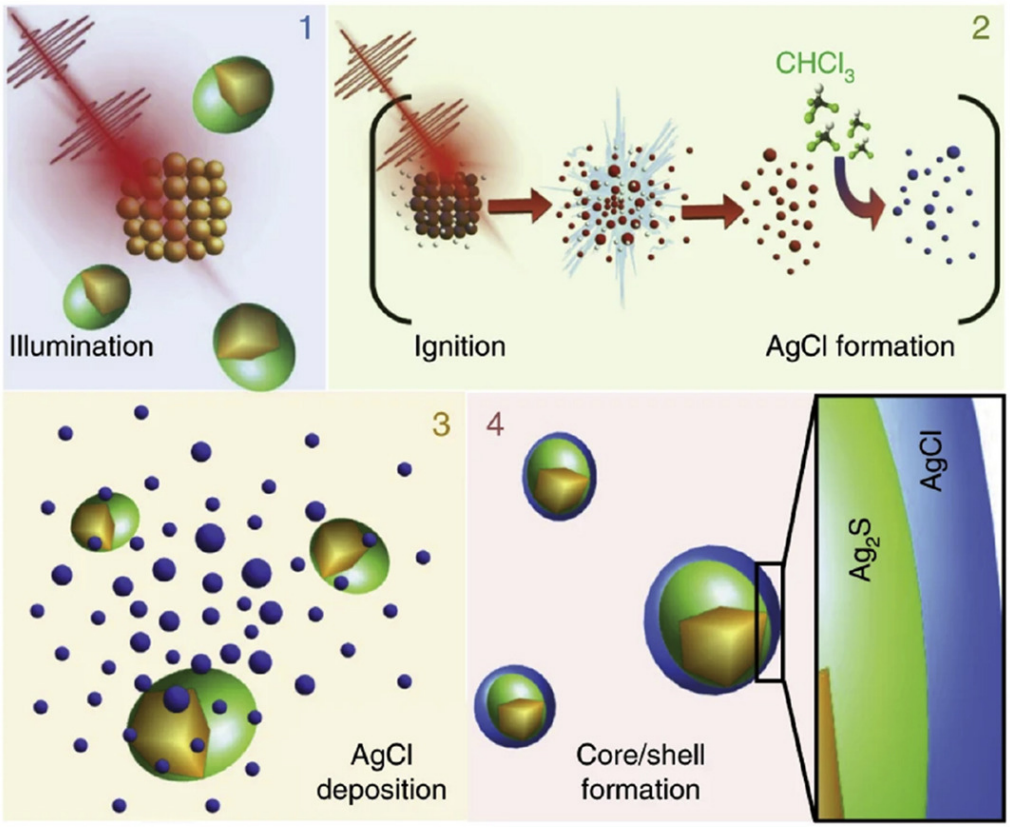

Figure 1.12: Schematic illustration of the transformation from Ag_2S nanodots to Ag_2S superdot by ultrafast laser pulse[53]; copyright 2020, Springer Nature.

tion, which then promotes non-radiative excitonic relaxation *via* Auger recombination[56]. Although blinking may be neglected in ensemble measurements, the optical measurement of a single QD probe can be detrimental if a stable fluorescence signal is desired. Yuan et al. recently reported experimental evidence that suggests the coexistence of two blinking pathways in a single QD—one due to fluctuations in adsorbate at the crystal surface (BC-blinking) and a second involving both radiative and nonradiative rate-jumps due to charging (Auger-blinking) (Figure 1.14)[57]. Previous reports suggest that non-blinking QDs can be made by controlled epitaxial inorganic shell growth on the QD core, potentially leading to higher QY and more consistent fluorescence outputs[58].

Photostability

The photostability of NIR QDs has been understudied, especially in comparison to that of visible QDs. It is generally accepted that the photostability of NIR QDs is much higher

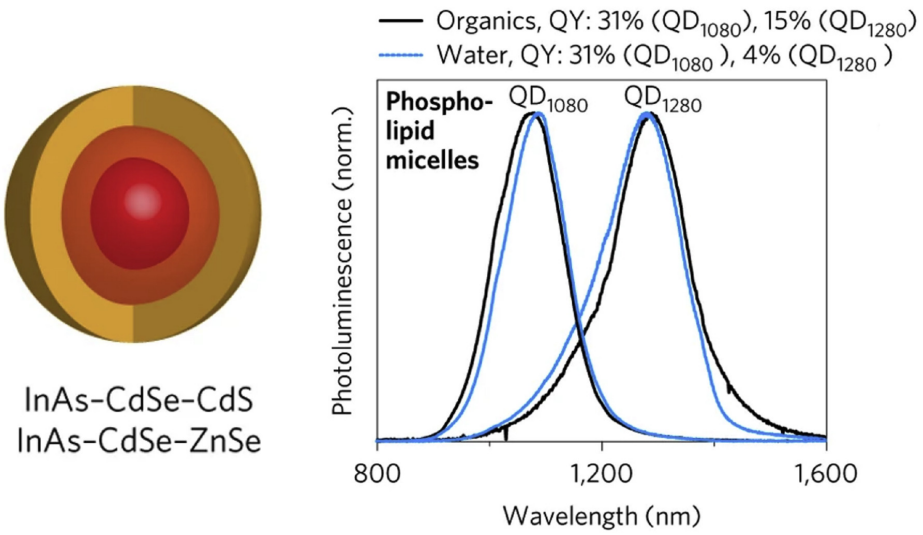

Figure 1.13: Highly bright InAs-based QD in aqueous phase[54]; copyright 2017, Springer Nature.

than that of organic NIR dyes. This increased photostability of QDs is attributed to their controlled inorganic structure and stable organic ligands, which reduces the formation of surface trap sites and prevents particle aggregation *via* ligand desorption. By using a slow and continuous injection of precursors, Franke et al. synthesized InAs QDs that exhibited less than 10% photobleaching upon >100 mW/cm^2 irradiation and up to two months of photostability[59]. More recently, Zamberlan et al. reported PbS QDs capped with dihydrolipoic acid–polyethylene glycol ligands, with stable photoluminescence for up to 9 months[60].

Lanthanide-doped nanoparticles

Lanthanide-doped nanoparticles (La NPs) usually consist of a host nanomaterial, a sensitizer, and an activator. Host nanomaterials, which provide the template for lanthanide dopants, must be transparent to allow for excitation and emission light to pass through. Various kinds of lanthanide dopant ions have been used as "sensitizers," which absorb excitation light and transfer the harvested energy to the "activator" that in turn emits photoluminescence (e.g. Yb, Er-doped $NaYF_4$).

Conventionally, La NPs have been extensively studied as upconversion PL probes, converting near-infrared irradiation into visible PL. More recently, the downconversion of visible light to NIR by La NPs has emerged as an area of interest in NIR probe development. La NPs exhibit advantageous NIR optical properties compared with other NIR probes including a low level of photobleaching, narrow emission bandwidth, non-photoblinking, and feasible time-gated lifetime imaging based on their long radiative lifetime.

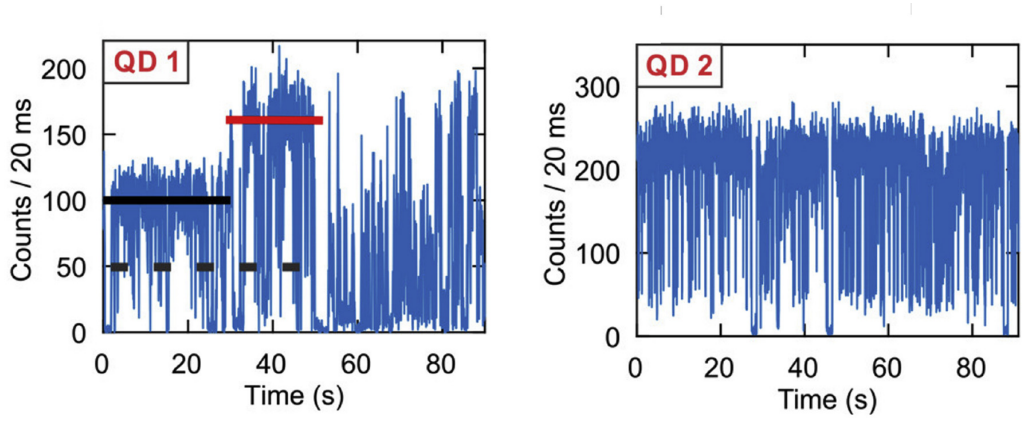

Figure 1.14: Two characteristic blinking behaviors of QDs[57]; copyright 2018, American Chemical Society.

Tuning the emission of La NPs

Numerous NIR-emitting La NPs have been reported with different host materials and sensitizer/activator ions. A number of transparent inorganic matrices in the visible and NIR window have been used as the host material for NIR-emitting La NPs including $NaYF_4$, $NaCeF_4$, $NaGdF_5$, LaF_3, and Y_2O_3. As sensitizers, Yb^{3+} and Nd^{3+} ions are frequently selected due to their high absorption cross-section (1.2 x 10^{-20} cm^2 at 980 nm and ˜10-19 cm^2 at 810 nm respectively)[61,62]. The 980 nm excitation light for Yb^{3+} is absorbed by water and causes heat damage to biological samples, a problem that is mitigated with Nd^{3+} ions that have multiple absorption peaks at 730, 808, and 865 nm[62].

Nd^{3+}, Ho^{3+}, Pr^{3+}, Tm^{3+}, and Er^{3+} have been used as activators with NIR luminescence centers at 1060 nm, 1155 nm, 1289 nm, 1475 nm, and 1525 nm peaks, respectively (Figure 1.15)[63]. For example, Er and Yb-doped $NaCeF_4$ nanocrystals were synthesized by high-temperature co-precipitation methods and exhibit intense 1530 nm NIR emission with a maximum PL QY of 32.8% upon excitation at 980 nm[64].

Although other reviews have covered recent advances in downconverting NIR-emitting La NPs, a significant remaining issue is their relatively low absorption coefficient[61,63,65]. The absorption coefficient of La NPs are still typically lower than organic dyes and other nanoparticles by several orders of magnitude; for example, the collective absorption coefficient of $NaCeF_4$ NP doped with 20% Yb and 1% Er (core diameter = 7 nm) is approximately 2000 $M^{-1}cm^{-1}$ at 980 nm[64] in comparison to ˜104 $M^{-1}cm^{-1}$ (organic dye) and ˜105 $M^{-1}cm^{-1}$ (QD). To overcome the weak light-absorbing characteristics of La NPs, exogenous organic dyes and QDs can be added to the La NP surface to harvest the excitation light in a broader wavelength range. This energy is then transferred to sensitizer ions, creating an "antenna effect"[66]. This antenna effect has been demonstrated by combining surface-immobilized IR

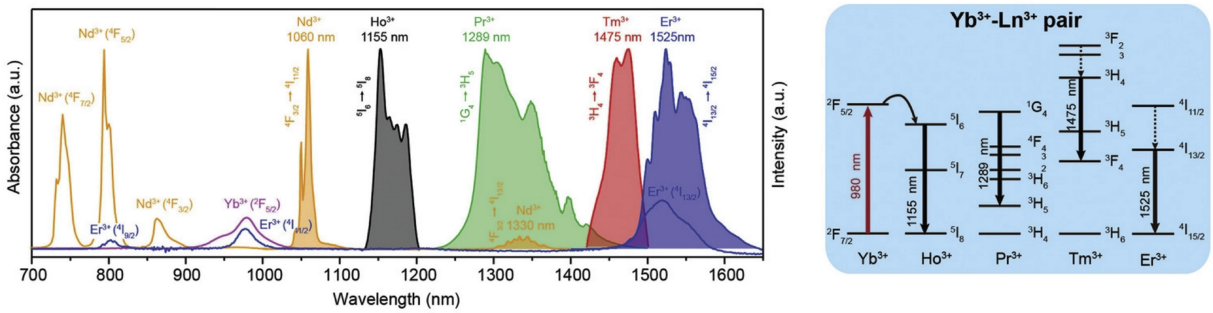

Figure 1.15: Absorption and downconverted NIR emission spectrum of various lanthanide ions and proposed energy transfer mechanism for NIR emission in Yb^{3+} and Ln^{3+} paired systems[63]; copyright 2019, Wiley-VCH GmbH.

dyes (Figure 1.16)[67] and biocompatible indocyanine green (ICG) dye[68] to the increased absorptivity of La NPs. More recently, Ag_2S[69] and Ag_2Se QDs[70] have been also employed as antennas for La NPs, leading to QD-LaNP complexes with a higher absorption coefficient and greater photostability than their counterparts with organic dye-based antennas.

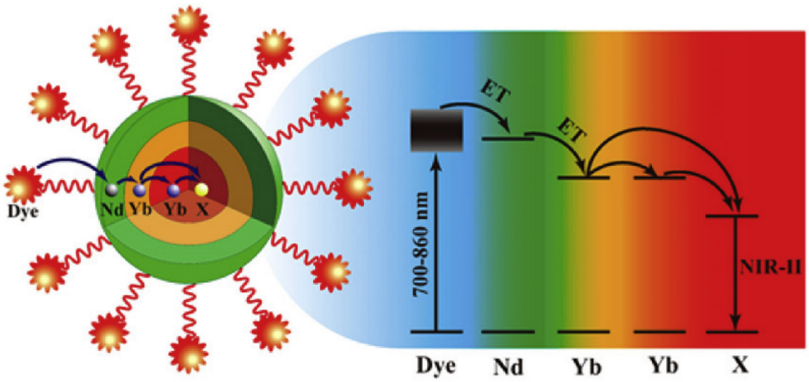

Figure 1.16: Absorption-enhanced NIR-emitting La NPs by antenna effect from surface-conjugated dyes[68]; copyright 2012, Springer Nature.

Improving quantum yield and fluorescence lifetime modulation

Due to their separated absorption (sensitizer) and luminescence (activator) centers, La NPs exhibit a large Stokes shift and tunable radiative pathway controlled by the distance and

location of lanthanide ions in nanocrystals. Downconversion La NPs have been studied less than upconverting La NPs, but in current technologies, the PL QY of downconverting La NPs has shown PL QY ranging from 1% to 30%, which is higher than that of organic dyes and SWNT and similar to that of NIR QDs (Table 1.1).

Compared with their s- and p-orbitals, the f-orbitals in lanthanide ions are strongly shielded and therefore behave as inner, rather than valence, electrons with narrow excitation and emission bands[71]. These parity-forbidden f-f transitions exhibit long lifetimes ranging from sub-milliseconds to milliseconds. These long lifetimes enable facile time-gated PL measurements, drastically improving signal-to-background ratios by removing short-lived emission and scattered excitation light[72]. In addition, Fan et al. reported that the controlled activator concentration and the thickness of the energy relay layer can tune the emission lifetime of Ho and Er emitting La NPs spanning three orders of magnitude with a single NIR emission band (Figure 1.17)[73]. Increasing the thickness of interlayers that relay energy between the sensitizer and activator in multi-shell La NPs can tune the emission lifetime from 0.04 ms to 7 ms. This enables time-domain multiplexing, which spatially resolves the multiple nanoparticles by their specific emission lifetime.

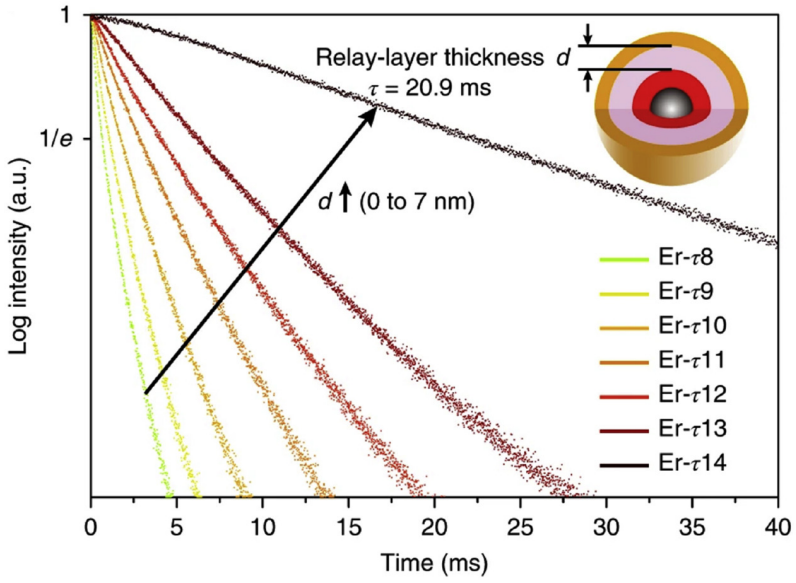

Figure 1.17: High tunable NIR radiative lifetime of La NPs by controlling the relay-layer thickness between sensitizer and activators[73]; copyright 2018, Springer Nature.

Photostability

Because their absorption and radiation pathways originate from a shielded f-f transition that is insensitive to the environment, La NPs exhibit no blinking and have exceptionally photostable PL under modest laser excitation. For example, Yb^{3+}- and Er^{3+}-doped $NaYF_4$ nanocrystals showed no fluctuation or photobleaching of their upconverted PL at individual and ensemble levels under a modest continuous laser power of 5 x 106 W/cm^2 at 980 nm[74]. The photostability of NIR-emitting downconverting La NPs has not been investigated extensively compared with upconverted La NPs[74,75], but it is expected that their photostability will be similar due to a shared nanostructure and optical pathways. The chemical stability of La NPs is generally superior to the chemical stability of inorganic QDs; for example, host material NaYF4 has reported extraordinary chemical stability[74–76].

1.6 NIR fluorescent proteins

For certain biological applications, the use of chemical or abiotic fluorescent probes is desirable; however, genetically encoded fluorescent reporters offer a number of advantages including cell specificity and tissue-targeted expression *via* viral vector delivery. Therefore, it is not surprising that in recent years there has been a focus on the development of NIR fluorescent proteins to, as with other NIR probes, take advantage of the tissue transparency window and extend multiplexing capabilities (Figure 1.18).

Although some naturally occurring protein systems make use of chromophores with absorption maxima well into the NIR range, they are typically not easy to adapt for use as fluorescent reporters. For example, the P870 and P960 bacterial reaction centers have maxima at 870 and 960 nm, respectively[78]. Although typically non-fluorescent, they can be made so by inactivation of their photochemical pathways; however, they are far red-shifted due to strong coupling of two chromophores. In addition, as multi-component membrane-bound proteins, they are not easily engineered into workable reporters. Importantly, they also contain components that are not synthesized by animal cells, which are the typical end targets for these proteins. In fact, although Fischer and Lagarias successfully engineered a cyanobacterial phytochrome for intense fluorescence at 672 nm in 2004, the necessity to provide additional machinery to produce the chromophore in animal cells has prevented widespread use as a template for further engineering[79]. As such, most current NIR proteins are based on bacterial phytochromes that make use of biliverdin as the chromophore, a pigment naturally available to cells as a product of heme breakdown. Shu et al. demonstrated the first successful expression of such a system in 2009[80]. Since then, dozens of proteins have been engineered to improve upon and extend the capabilities of this first demonstration.

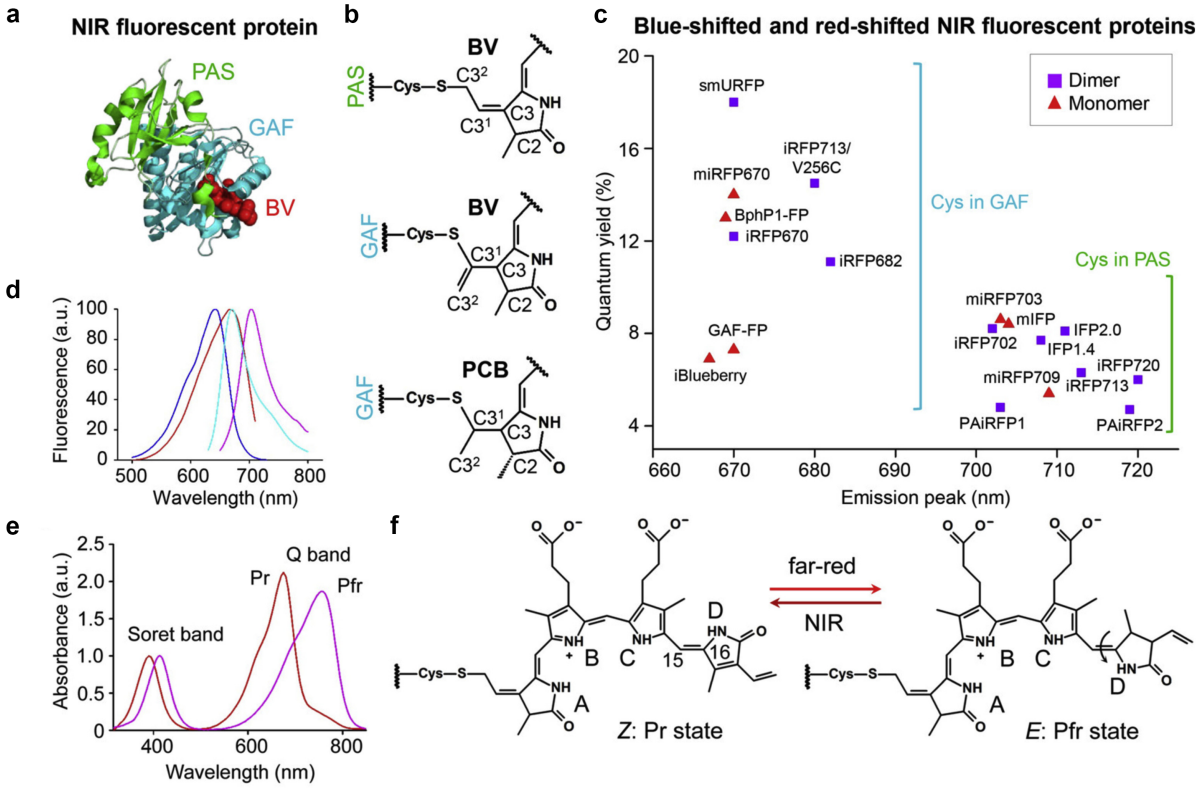

Figure 1.18: NIR-fluorescent proteins. **(a)** Structure of a two-domain NIR protein with PAS (Per–ARNT–Sim) and GAF (cGMP phosphodiesterase–adenylate cyclase–FhlA) domains shown, along with BV (biliverdin). The third domain of the protein is truncated. **(b)** Chemical structures of BV or PCB (phycocyanobilin) bound to Cys residues in the PAS or GAF domains. **(c)** Binding of BV to Cys residues in the GAF domain causes blue shifting of fluorescence. Squares represent dimeric proteins, whereas triangles represent monomers. **(d)** Typical excitation and emission spectra for proteins with a Cys residue in the PAS domain (ex. red, em. magenta) or GAF domain (ex. blue, em. cyan). **(e)** Absorption spectra of phytochromes in red or far-red states. **(f)** Reversible isomerization reaction of BV that drives the transition between the two states[77]; copyright 2017, American Chemical Society.

Limitations and advancements in NIR protein engineering

Red-shifting absorption and emission

As NIR proteins need to be expressed in cells, their primary engineering limitations are the constraints of the native capabilities of the cell and the requirement to use a genetically

tractable model organism. For this reason, as stated earlier, although there are examples of naturally occurring chromophores far into the near-infrared, their versatility is highly restricted. The engineering challenge is then to attempt work within the constraints provided by the target system of interest. Bacterial phytochromes have primarily been used as a template as they provide the most straightforward model from which to work. It is therefore of some interest to discuss the structure and function of these proteins.

As the phytochromes that exist across algae, plants, and cyanobacteria, bacterial phytochromes are generally thought of as red light receptors, able to interconvert between a red and a far-red absorbing state[81]. This process is controlled by an isomerization reaction around the central chromophore[77]. Notably, the maximum absorbance of the far-red state is Stokes shifted by ˜70 nm, out to about 770 nm; however, the fluorescent population of phytochromes is usually not able to undergo the photochemical reaction to bring about the transition. In the generation of a more stable population of fluorescent phytochromes, the protein domains are truncated to make the transition unfavorable and stabilize the red-state, with mutations also designed to change the chromophore environment[82].

Due to the use of a naturally occurring chromophore, and the necessity for a large number of structural modifications to the protein it binds with, the number of possible further mutations to modify chromophore absorption becomes limited. One possible future approach to address this would be to seek stabilization of the far-red phytochrome state instead, using structure-driven rational mutagenesis, although any such work has yet to be demonstrated. At the cost of increased complexity, another approach would be to integrate exogenous dyes or chromophores with proteins of interest. For example, Zeng et al. demonstrated the complex of H2a-4T dye with fetal bovine serum proteins and Cetuximab to perform image-guided photothermal therapy of cancer in mice, in the NIR-II window[83].

Monomeric versus dimeric

At the most general level the population of near-infrared proteins can be categorized into two groups: monomeric or dimeric. The first demonstration by Shu et al. falls into the latter category, heading a category of proteins now referred to as infrared fluorescent proteins (IFPs). In this case, the dimerism was generally seen as a disadvantage, and their final product, IFP1.4, showed more propensity to monomeric behavior. Subsequent efforts worked to improve brightness and specificity of biliverdin for the protein. IFP2.0 was shown to be roughly 13x brighter and has been imaged in *Drosophila* larvae and mouse brain tissue, with monomeric propensity[84]. IFPs have excitation maxima in the 680–690 nm range, with emission maxima at around 708 or 711 nm.

The second group of dimeric proteins are known as infraRed fluorescent proteins (iRFPs). These were developed using a different bacterial phytochrome as a template, from *Rhodospirillum centenum*, and variants were engineered with emission wavelengths between 670 nm and 720 nm (the most red-shifted of the dimeric proteins), with 1–2x brightness compared with IFPs[85]. A small number of photoactivatable proteins have also been produced for selec-

tive imaging or potentially super-resolution microscopy techniques, derived from a different bacterial phytochrome[86].

In contrast, for many applications, (exclusively) monomeric proteins are preferred, particularly if fusion partners are involved for tracking studies. These more recent developments have been mostly derived from the previous dimeric versions with generally similar optical properties. Matlashov et al. recently demonstrated monomerization of the iRFPs, yielding the set of miRFPs, and some enhanced counterparts, emiRFPs[87]. They furthermore demonstrated the ability to do two-color STED imaging with these proteins in cells and mice (Figure 1.19). Their furthest red-shifted variant miRFP703 had an emission maximum at 703 nm. In the previous work from the Verkhusha group though, Shcherbakova et al. demonstrated miRFP709 with a maximum of 709 nm. Hodgson and colleagues were able to produce the furthest red-shifted monomeric iRFP, miRFP720, with a 720 nm emission maximum[88]. In addition, they demonstrated its compatibility as an FRET pair with miRFP670. IFP2.0 has also been engineered into a fully monomeric form, mIFP2.0[89]. Recently, Ollinyk et al. demonstrated a new model template for monomeric proteins[90]. Using a single domain of a cyanobacteriochrome, they were able to produce the smallest monomeric fluorescent protein, named miRFP670nano, which is unrelated to the miRFPs described above. At 17 kDa, it is over 1.5x smaller than GFP-like fluorescent proteins, and is therefore a useful fusion partner, and can be used as a FRET donor for further red-shifted proteins.

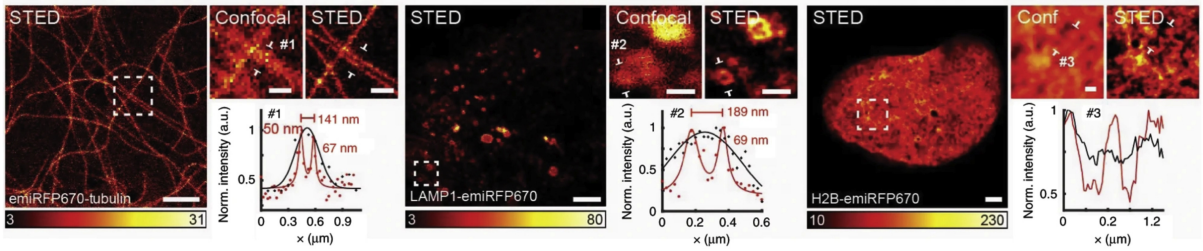

Figure 1.19: NIR-protein expression in HeLa cells. Confocal and STED images with a line profile along the indicated section of HeLa cells expressing an emiRFP670-tubulin fusion (left), U2OS cells expressing a LAMP1-emiRFP670 fusion (center), and U2OS cells expressing an H2B-emiRFP670 fusion (right). Scale bars are 2μm for the full images and 500nm for the inserts showing the zoomed-in regions of interest[87]; copyright 2020, Springer Nature.

Applications

In the past five years, the emergence of NIR proteins has seen their application to a variety of biological fields, from cancer to neuroscience. They have also been integrated into more advanced imaging methodologies, such as FRET[88,90], BRET[91], and super-resolution techniques

Table 1.2: Brightness versus emission wavelength of NIR proteins.

	Excitation wavelength (nm)	**Emission wavelength (nm)**	**Quantum yield (%)**	**Extinction (M^{-1} cm^{-1})**	**Brightness vs. iRFP (%)**
Dimeric proteins					
IFP1.4	684	708	7	92,000	8
IFP2.0	688	709	6.88	72,900	80
iRFP670	643	670	12.2	114000	225
iRFP682	663	682	11.1	90,000	162
iRFP702	673	702	8.2	93,000	124
iRFP	690	713	6.3	98,000	100
iRFP720	702	720	6	96,000	93
Monomeric proteins					
miRFP670	642	670	14	87,400	198
miRFP670-2	643	670	13.6	103,000	227
miRFP680	661	680	14.5	94,000	221
miRFP682	663	682	11.2	91,000	165
miRFP702	673	703	8.1	88,000	115
miRFP703	674	703	8.6	90,900	127
miRFP709	683	709	5.4	78,400	77
miRFP713	690	713	7	99,000	112
miRFP720	702	720	6.1	98,000	97
mIFP2.0	683	705	6.9	65,900	111
miRFP670nano	645	670	10.8	95,000	167
emiRFP670	642	670	14	87,400	198
emiRFP703	674	703	8.6	90,900	127
Wi-Phy	701	719	4.7	92,991	7

such as STED[87,92]. The development of photoactivatable NIR proteins is promising for future demonstrations of techniques such as PALM, STORM, and RESOLFT as well. NIR proteins have been of particular utility in applications requiring multiplexing with existing architectures in the visible range, such as multi-channel imaging or optogenetics[93].

Background reduction and highly multiplexed imaging

The broad absorption and emission bands of fluorescent proteins have traditionally limited the number of simultaneous channels that can be acquired without fully spectrally resolved detection and deconvolution. NIR proteins have been shown to allow for multi-channel imaging, both among themselves, and with fluorescent proteins in the visible range. Donnelly et al. used miRFP703 in 4-channel imaging, as well as an additional FRET assay to study the role of Rac3 in breast cancer invasion and metastasis[94]. In developing their NIR fluorescent protein, smURFP based on an allophycocyanin, Rodriguez et al. developed a cell cycle indicator using the further red-shifted IFP2.0 as well[95]. Shcherbakova et al. similarly demonstrated this capability using miRFPs[96]. In the same study, they demonstrated the capability of producing three channel SIM super-resolution images across the visible and NIR and the ability to split these proteins to produce a reporter for protein-protein interactions. Telford et al. have also demonstrated the ability to do simultaneous red/NIR-excitation-based cell sorting using the iRFP family[97]. Janssen et al. used multi-channel imaging with mRFP, GFP, and miRFP to study how myosin-V is involved in immobilization of cargo transport along the axon[98].

Neuroimaging and optogenetics

Many neuroscientists have turned to NIR proteins, particularly as the quest continues for high-resolution imaging deeper and deeper into the brain. These proteins' far-shifted absorption spectra also make them well suited for use in combination with the blue wavelengths typically used for optogenetic stimulation. Piatkevich et al. extensively characterized the viability of using iRFPs under two-photon excitation in neurons (Figure 1.20)[99]. Richie et al. also demonstrated the feasibility of using iRFP713 as a reporter protein across sub-cellular locations in neurons, as well as its viability for use as a transgenic Cre-reporter for functional studies[100]. Weinhard et al. used iRFP in conjunction with light-sheet microscopy and correlative light electron microscopy to study the microglial-mediated remodeling of synapses[101]. Qian et al. also engineered a novel NIR genetically encoded Ca^{2+} indicator based on mIFP, demonstrating its usability in cultured cells and brain tissue[102].

A number of advances have also been made in the use of NIR fluorescent proteins, and NIR wavelengths generally, in optogenetics. In their report of miRFP720, Shcherbakova et al. demonstrated the compatibility of their NIR FRET-based biosensor with the blue-green LOV-TRAP optogenetic system[88]. Roman et al. used iRFP713 to track nuclear motion and sequestration upon muscle contraction with optogenetic stimulation[103]. Other research has focused instead on how to produce NIR controllable optogenetic tools, which would

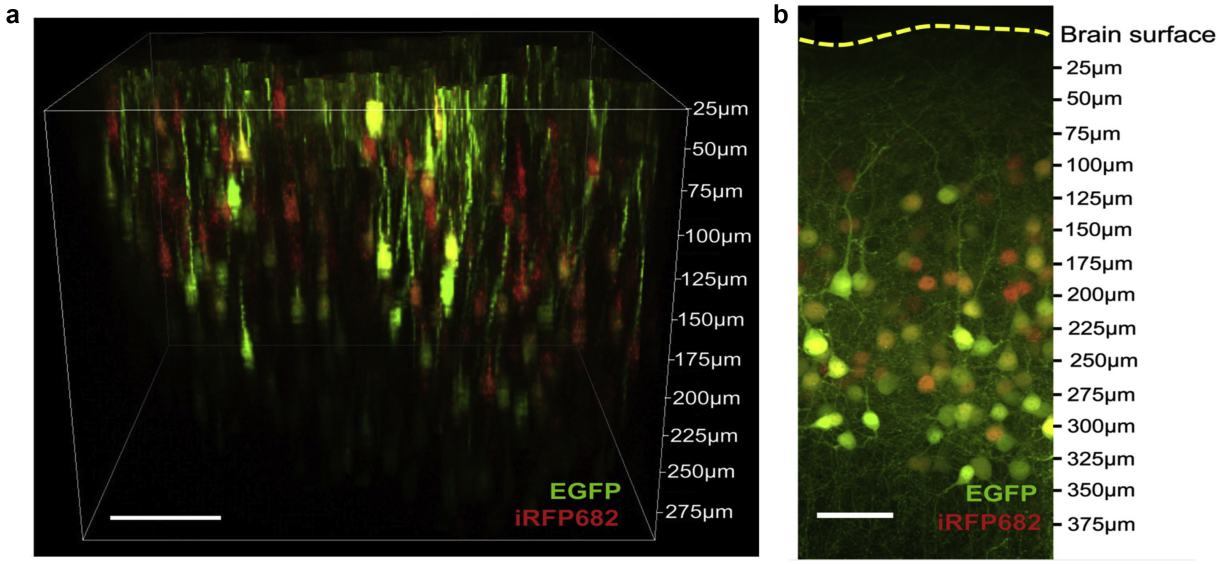

Figure 1.20: Imaging of NIR protein expression in mouse cortex. **(a)** *In vivo* two-photon imaging of iRFP682 in-mouse cortex acquired with 6.5 mW 880 nm excitation. Volumetric view of EGFP and iRFP682-expressing neurons in layers 1 and 2/3 of a mouse cortex. Scale bar 100 μm. **(b)** Confocal images acquired from a fixed slice of the region in (a) acquired with 488 nm and 637 nm excitation. Scale bar 50 μm[99]; copyright 2017, Biophysical Society.

be compatible with existing blue-green technologies. Kaberniuk et al. engineered an NIR optogenetic system based on a bacterial phytochrome BphP1 and its binding partner PpsR2, which showed control of cell morphology and gene expression under 740 nm and 780 nm excitation[104]. Redchuk et al. demonstrated that a similar system based on a BphP1-QPAS1 pair could induce gene transcription similarly to a blue-light system, LightOn[105]. This work also showed that it could be used simultaneously with another blue-light system, LOV.

1.7 NIR light sources and detection

As NIR optical probes have developed, there has been a concurrent search for new materials for light sources that can take advantage of the NIR spectral window. Since their first demonstration in the early 1980s, Ti:Sapphire lasers have been widely adopted as the NIR solid state laser standard, particularly for pulsed laser applications, due to their relatively broad tunability in the NIR. However, new laser technologies can now push the wavelength tuning range out to 2000 nm and beyond, produce supercontinuum sources, and provide nanostructured solutions for photonic circuitry and biomedical applications. Advances in

fiber technologies have focused on increased bandwidth and amplification for communication purposes, as well as on new materials better suited to addressing specific biological or clinical problems. Additional work has focused on the development of broadband incoherent sources, particularly for compact, low-cost spectroscopy applications.

Fiber lasers

Demand for increased optical communication bandwidth and transmission rates, and for compact laser systems for biological and clinical applications, has continued to drive the development of new fiber laser and amplifier materials. For the division multiplexing techniques, especially the popular wavelength division multiplexing (WDM), that are used for optical communication, large bandwidth luminescent fiber materials are needed to provide sufficient optical power over all transmission bands. Recent work has focused on extending the capabilities of the popular Er^{3+}-Doped Fiber Amplifiers (EDFA) through the introduction of additional rare earth ions. Chu et al. improved on Er3+-doped bismuth borosilicate glasses by the additional codoping of Ce^{3+} and Yb^{3+}, producing a broadband luminescent material with a full-width-half-max (FWHM) of ˜80 nm, and a reduction in undesirable up-conversion emission and excited state absorption[106]. Dan and colleagues demonstrated a Nd^{3+}-Bi^{+}-Er^{3+} co-doped silica glass with ultra-broadband NIR luminescence of 600 nm FWHM from 1000 to 1600 nm, covering all transmission bands[107]. Subsequently, they investigated the use of Y^{3+} for the enhancement of luminescence from Bi^{+}-Er^{3+} co-doped fibers[108]. Other investigations have focused on the integration or adoption of entirely new materials. Cheng and colleagues demonstrated a simplified manufacture of a glass-based PbSe quantum dot fiber amplifier (QDFA), with double the FWHM and roughly half the level of noise of conventional EDFAs currently available[109].

The integration of optically active nanostructures as pulsed lasers has also been pursued for a variety of applications. Ming et al. used PbS/CdS core/shell quantum dots as saturable absorbers to produce a candidate for tunable passively mode-locked Er^{3+}-doped fiber lasers[110]. Cheng et al. similarly used the novel transition-metal dichalcogenide $PdTe_2$, to produce a passively Q-switched Yb^{3+}-doped fiber laser operating at 1066 nm[111]. Using carbon nanotubes as the saturable absorber, Meng et al. demonstrated a mode-locked thulium fiber laser with a 200 nm tuning range covering 1860–2060 nm[112]. In addition to optical communications, thulium fiber lasers have been increasingly adopted for surgery applications, in particular for urology, due to the strong absorption of water at their operational wavelengths[113].

Nanowire lasers and detectors

Nanostructured light sources open many exciting avenues for the development of on-chip systems and nanophotonic circuitry for a variety of applications. In particular, nanowire lasers appear to be especially promising for their ability to provide guided coherent light in extremely compact geometries—often just microns along the long axis and hundreds of

nm along the short. Two remaining challenges, however, are the manufacturing of nanowire lasers at longer NIR wavelengths and lasing at temperatures close to room temperature. A number of material compositions and manufacturing techniques have been proposed to overcome these issues. Ren et al. presented a GaAsSb nanowire with high Q factor lasing and a relatively high characteristic temperature of 129 K, with an emission wavelength tunable from 890 to 990 nm based on the relative Sb composition of the lattice[114]. Chen et al. manufactured a GaAs/GaNAs/GaAs multishell nanowire with emission at 1000 nm and an estimated characteristic temperature of 160 K[115]. Efforts to produce NIR organic lasers are typically hampered by intrinsic non-radiative processes, dictated by the energy gap law. Recently, Wu et al. took advantage of the excited-state intramolecular proton transfer process between the enol and keto forms of the compound (E)-3-(4-(dimethylamino)phenyl)-1-(1-hydroxynaphthalen-2-yl)prop-2-en-1-one (DMHC) to overcome this barrier and demonstrate a single-crystal organic nanowire laser[116].

The NIR optical properties of nanowire structures have also been investigated more generally for optoelectronic and detection applications and for use in absorption-based imaging and medical technologies. Li et al. first demonstrated broadband photoluminescence from silicon nanowires across the visible and NIR (500–920 nm) under 980 nm CW illumination, with potential applications from biosensors to an optical source in itself[117]. Zheng et al. demonstrated the possibility to use p-type SnS and SnSe nanowires as NIR photodetectors with sub-ms response[118]. More recently, Sb_2Se_3 nanowires have been used to produce similarly rapid photodetectors for the visible through NIR. These crystalline nanowires exhibit strong anisotropy, yielding a highly polarization sensitive detector[119]. The strong absorption of some nanowire substrates in the near IR has also made them useful targets for photothermal therapies. For example, Au-coated Si nanowires have been demonstrated as suitable for photothermal treatment of cancer cells[120].

LEDs

In contrast to most lasers, light-emitting diodes (LEDs) tend to be more portable, cost-effective, and safer to use for a variety of applications ranging from NIR spectroscopy to light therapies. Similar to organic solid state lasers, traditional NIR LED technologies have often focused on semiconductors due to the high non-radiative decay of organic compounds in the NIR. In recent years, significant work has been done to expand the set of materials available for LEDs, while also producing extremely broadband sources for spectroscopy and imaging across the NIR window.

Recent work has demonstrated the possibility of manufacturing organic LEDs operating in the NIR. Hu et al. designed exciplex-based OLED materials with NIR emission at either 704 or 730 nm based on combinations of a novel synthesized fluorescent compound and commercially available materials[121]. Zhang et al. improved on existing Ir(III) complexes, which have been used previously to produce mixed red/NIR emission, by demonstrating Ir(III) based OLED with complete emission in the NIR, centered at 850 nm[122]. Similarly, Wei et al. improved on existing Pt(II) organometallic complexes producing NIR emission between

866 and 960 nm, with a record photoluminescence quantum yield of 5%–12%, through exciton delocalization over numerous molecules[123].

Substantial improvements in phosphor-converted LEDs for broadband NIR emission have also been realized in recent years. Numerous Cr3+-based phosphors have been designed, usually used in conjugation with a blue LED for excitation, often with NIR photoluminescence yields of ¿65%, broadband emission over 700–1100 nm, and high thermal stability. Output powers in the 10s of mW make these LEDs suitable for a variety of near infrared spectroscopy applications[124–127]. Basore et al. have also demonstrated Cr^{3+}:garnet LED with 98.6% internal quantum efficiency and high power emission of over 750 mW over the 700–1000 nm range[128]. Most recently, Eu^{2+}-doped phosphors have also been used to produce broadband LEDs covering the visible and NIR[129,130].

1.8 Future directions and perspectives

Over the past several years, the development of new NIR-emitting materials has rapidly expanded due to a growing understanding of the structural and material characteristics that underpin their luminescent properties. In particular, NIR materials have enabled better control over stability, quantum yield, and tunability of material performance in complex environments for applications in biology, as optical light sources, and in detectors.

New molecular engineering techniques have expanded the traditional emission window for NIR-emitting organic dyes, particularly for small molecule dyes. As new molecular structures become easier to synthesize, dyes with higher QY, narrow emission wavelengths, and large Stokes shifts will be easier to achieve. In parallel, efforts toward carbon-based NIR emitters such as SWNTs and carbon dots have revealed exciting nonlinear optical properties that can be tuned through better control of material properties such as chirality and electronic doping. Similarly, inorganic nanomaterials including semiconducting quantum dots and lanthanide-based nanoparticles exhibit significantly higher QY while maintaining some degree of tunability through changes in material composition. However, there remain a number of areas that warrant further exploration, including the study of downconverting nanoparticles and improved absorption coefficients.

Here, we have limited our focus to the use of nanomaterials in aggregate. However, nanomaterials also offer exciting possibilities in tracking single molecules and super-resolution imaging, with work still remaining to balance the need for smaller sizes with brightness and stability. In particular, SWNTs have been able to mitigate some of the challenges faced by molecular dyes and fluorescent proteins to enable single molecule tracking[131,132]. Many of the properties highlighted in this chapter, including the narrow-band emission and size-tunable emission exhibited by quantum dots and upconverting nanoparticles, are ideal for super-resolution microscopy. We direct readers to other recent publications that provide a more comprehensive discussion of the use of nanoparticles in these applications[133].

As NIR luminescent materials are increasingly desired for biological imaging applications, new engineering tools can be leveraged to engineer NIR fluorescent proteins at smaller length

scales and with an expanded emission window. This development is critical for applications such as multi-channel imaging and optogenetics and cell-specific targeting of NIR emitters. Likewise, new engineered materials have been recently developed for expansion of lasing, detection, and LED capabilities into the NIR spectrum. The interplay of these different material systems could allow researchers to overcome many of the existing barriers in the development of tools for NIR imaging. We hope this work will provide a fundamental understanding of the underlying chemical and physical properties that govern NIR emission across this diverse range of materials, inspiring future efforts by researchers who seek to develop and use NIR-emitting materials.

Chapter 2

Nanotechnology to advance CRISPR–Cas genetic engineering of plants

2.1 Chapter abstract

CRISPR-Cas genetic engineering of plants holds tremendous potential for providing food security, battling biotic and abiotic crop stresses caused by climate change, and for environmental remediation and sustainability. Since the discovery of CRISPR-Cas technology, its usefulness has been demonstrated widely, including for genome editing in plants. Despite the revolutionary nature of genome-editing tools and the notable progress that these tools have enabled in plant genetic engineering, there remain many challenges for CRISPR applications in plant biotechnology. Nanomaterials could address some of the most critical challenges of CRISPR genome editing in plants through improvements in cargo delivery, species independence, germline transformation and gene editing efficiency. This chapter identifies major barriers preventing CRISPR-mediated plant genetic engineering from reaching its full potential, and discusses ways that nanoparticle technologies can lower or eliminate these barriers. We also describe advances that are needed in nanotechnology to facilitate and accelerate plant genome editing. Timely advancement of the application of CRISPR technologies in plant engineering is crucial for our ability to feed and sustain the growing human population under a changing global climate.

Chapter 2 is reproduced from work previously published as Demirer, G.S.; Silva, T.N.; Jackson, C.T.; Thomas, J.B.; Ehrhardt. D.W.; Rhee, S.Y.; Mortimer, J.C.; Landry, M.P. Nanotechnology to advance CRISPR–Cas genetic engineering of plants. Nature Nanotechnology 2021, 16, 243-250. https://doi.org/10.1038/s41565-021-00854-y.

2.2 Introduction

Plants are essential for food security and the production of therapeutics, bioenergy and biomaterials. To meet global demand sustainably, improving plants beyond their natural reserves and abilities is a promising strategy. Plant improvements began millennia ago with crop breeding to domesticate wild plants and increase their yield and nutrient density. The Green Revolution of the 1950s generated high-yielding varieties of semi-dwarf wheat and rice, and exemplified how plant breeding can boost yields to support a rapidly growing population[134]. Nevertheless, breeding requires extensive time and labour, is genetically non-targeted, can reduce plant fitness due to the potential co-introduction of undesirable traits and cannot introduce traits that do not exist in the crossed species.

Compared with conventional plant-breeding approaches, genetic-engineering methods, which rely on tools such as particle bombardment and *Agrobacterium tumefaciens* transformation, have broadened the range of traits that can be introduced and improved in plants[135] (see Box 1 for definitions of the main terms used in this chapter). However, these genetic-engineering tools insert genes into a random location in the plant genome and may cause undesirable outcomes. Recently developed nuclease-based genome-editing methods, such as TALEN (transcription activator-like effector nucleases) and CRISPR (clustered regulatory interspaced short palindromic repeats)-Cas, are precise, rapid, genetically targeted and can introduce novel traits into specific locations in the genome[136].

CRISPR-Cas genome-editing technology was awarded the Nobel Prize in Chemistry in 2020. CRISPR-Cas genome editing has and continues to be extensively studied in animal systems, including the first clinical trials with patient T cells[137]. CRISPR-Cas cargoes are commonly delivered to animal cells using ex vivo methods such as electroporation or in vivo vehicles such as viruses. In recent years, nanoparticles have emerged as an alternative vehicle suitable for delivering CRISPR editing components to mammalian cells. For example, cationic lipid-based nanoparticles can be used to encapsulate CRISPR components for cell delivery, albeit with some concerns regarding toxicity and non-specific cell uptake[138]. Additional advances have also demonstrated the use of gold nanoparticles that can be assembled with CRISPR-Cas complexes for delivery in mice[139].

In the field of plant biology and agriculture, CRISPR-Cas technology holds much potential for transforming plant functional genomics research, improving crop resilience to abiotic and biotic stresses, and rapidly introducing new desirable traits into crops. However, the widespread application of CRISPR technologies in plants faces several barriers. Obstacles include CRISPR cargo delivery challenges, limitations of plant tissue and cell culture, and lack of methods that work across plant species. In addition, our limited understanding of plant genetic and metabolic networks hinders the development of plant varieties with desired traits. Introducing CRISPR-engineered plants to the market may face further obstacles in many countries because of regulations and societal acceptance.

Over the past decade, the intersection of plant biotechnology and nanomaterials has been fruitful. Early use of nanomaterials in plants has focused on the synthesis of plant-based metallic nanoparticles, the delivery of agrochemicals, and nanoparticle uptake and toxicity

studies. More recently, nanomaterials have been used to deliver genes and proteins into plant cells for genetic-engineering applications[140–143]. Nanomaterials can reach previously inaccessible plant tissues, cellular and subcellular locations. In addition, nanomaterials can enable the targeted delivery and release of cargoes, and can protect cargoes from degradation. Finally, nanoparticles can often perform these tasks in a species-independent manner. While there is much potential for nanomaterials to address many central bottlenecks of CRISPR-based genome editing, several nanotechnology-specific advances are needed to realize the potential of these tools in plant biology. In this chapter, we discuss how current nanomaterial systems have addressed some challenges of CRISPR in plants, and what nanotechnology-specific advances are needed to circumvent the remaining barriers to plant CRISPR genome editing.

2.3 CRISPR genome editing in plants

In this section, we will first discuss some of the major accomplishments of CRISPR genome editing in plants, followed by the current limitations of plant CRISPR genetic engineering.

Accomplishments in plant genome editing with CRISPR plasmid and protein delivery

Genome editing in plants using the CRISPR-Cas system (Figure 2.1) has widely been reported[144]. Plasmids encoding the CRISPR-Cas reagents have been delivered into plant cells by various methods for either stable or transient transformation. CRISPR-Cas expression using transient methods is preferable, as transient methods do not rely on chromosomal integration of the CRISPR-Cas reagents but rather in their temporary expression using plant machinery. Transient expression of the CRISPR-Cas complex has been shown to result in fewer off-target mutations in bread wheat[145], no heritable DNA integration and hence a reduction of the regulatory burden. However, transient expression methods through plasmid delivery have had limited applicability so far, as most plant species are not susceptible to these DNA-delivery methods.

DNA-free editing, in which the CRISPR-Cas complex is introduced directly into plant cells, is an alternative genome-editing strategy (Figure 2.1b). Preassembled ribonucleoproteins (RNPs) have been successfully delivered *via* protoplast transfection[146] or particle bombardment[145]. However, these editing efficiencies are still low ($\leq$10%) outside of a few well-studied species[147]. Recently, an RNA virus was used to deliver CRISPR-Cas reagents, leading to heritable mutations of multiple genes simultaneously and editing efficiencies of 90-100% in infected somatic tissue[148]. A drawback is the limited host range associated with any virus-based tool. Comprehensive reviews of CRISPR-Cas applications in agriculture and plant biotechnology have been summarized elsewhere[149].

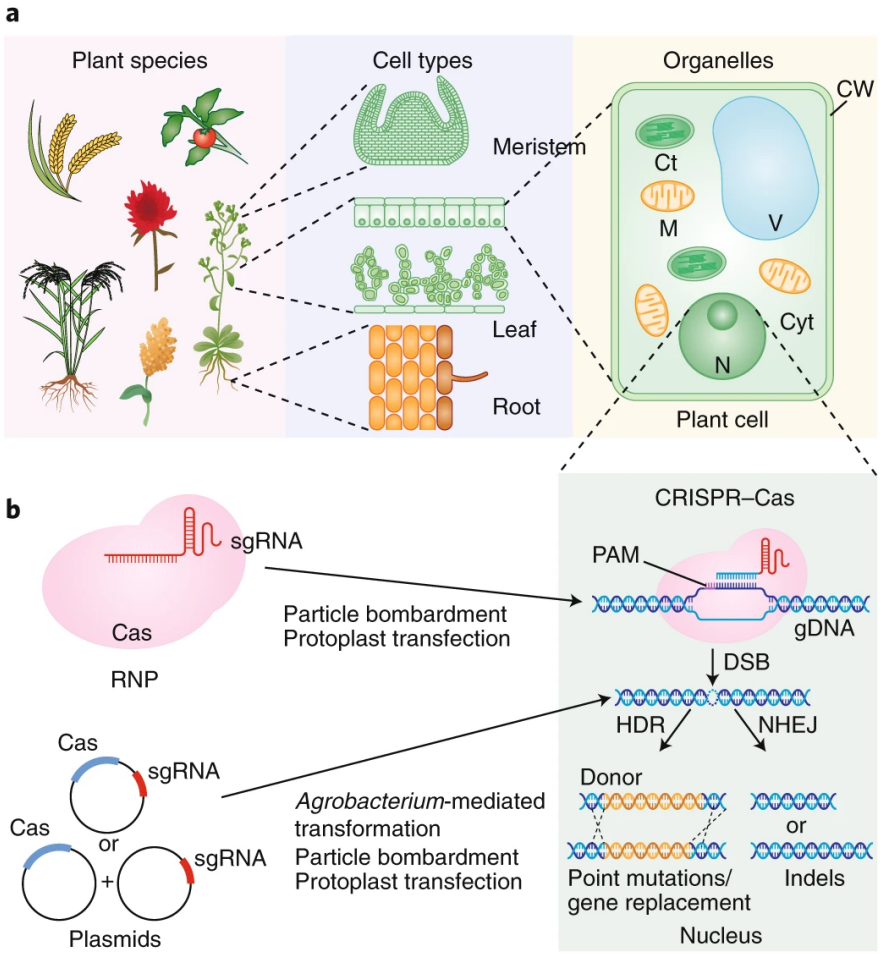

Figure 2.1: CRISPR–Cas reagent delivery to diverse plant species, cells and organelles. **(a)** Examples of plant species, cell types and organelles that can be targeted by the CRISPR-Cas system. **(b)** The CRISPR-Cas genome-editing system is derived from bacterial adaptive immunity. It consists of the Cas endonuclease, which site-specifically cleaves double-stranded DNA, and an sgRNA that hybridizes to approximately 20 nucleotides of the target sequence via Watson-Crick base pairing. A PAM upstream of the sgRNA binding site in the genome is also required. In the nucleus, the Cas protein and the sgRNA form an RNP complex and Cas undergoes conformational changes that enable DNA binding and cleavage. Once a double-stranded break (DSB) is generated, one of two plant DNA repair mechanisms is triggered. HDR, in which a DNA donor template with homology to the target sequence is provided, leads to point mutations or gene replacement. NHEJ, which is error-prone and generates small insertions or deletions (indels), is much more commonly demonstrated than HDR. RNPs can be delivered into the plant cell by particle bombardment or protoplast transfection. Alternatively, plasmids containing genes that encode Cas and the sgRNA are delivered into the cell through *Agrobacterium*-mediated transformation, particle bombardment or protoplast transfection. Ct, chloroplast; Cyt, cytoplasm; CW, cell wall; gDNA, genomic DNA; M, mitochondria; N, nucleus; V, vacuole.

Current limitations of CRISPR genetic engineering in plants

For full realization of the promise of CRISPR genome editing, we need simple, accurate and efficient methods to deliver CRISPR reagents to diverse plant species. A major barrier to all forms of plant genetic engineering is the need to induce somatic embryogenesis in species where germline transformation is not an option. Somatic embryogenesis is a time-consuming and technically challenging process, particularly in monocot species. Furthermore, even within a species, different genotypes respond differently to tissue culture. To expedite transformation, morphogenic regulators have been introduced into plants[150] to induce embryo formation from somatic cells[151] and, recently, to induce de novo meristem formation to circumvent tissue culture[152]. The latter has only been demonstrated in eudicots, but holds great promise if applied to monocots, particularly to species and genotypes recalcitrant to transformation.

A second critical barrier to plant CRISPR genetic engineering is a physical barrier to the delivery of CRISPR reagents-the plant cell wall, a rigid and thick extracellular matrix composed primarily of polysaccharides and absent in most other biological systems in which CRISPR has seen many successes. The use of protoplasts, plant cells in which the cell wall is removed by enzymatic digestion, can overcome this barrier, facilitating the delivery of CRISPR reagents. However, regeneration of full plants from protoplasts is technically challenging and has not been demonstrated in most species[153]. For intact plant cells, particle bombardment allows reagents to breach the cell wall, although it increases the chance of irreversible cell damage and suffers from a low editing efficiency.

Another challenge that prevents successful gene insertion through homology-directed repair (HDR) is the need for simultaneous delivery of donor templates as well as the CRISPR-Cas complex. Studies showing successful HDR in plants are very limited. A low HDR editing efficiency in plants is due in part to difficulty in delivering sufficient concentrations of the donor template into the nucleus at the cut site and the short stability of the donor template inside the plant cell[154]. Further advancements require the ability to deliver preassembled RNPs and donor templates in a manner that has not yet been reported in plants. CRISPR base editors are an alternative approach, which avoids the need for donor templates. Base editors consist of a catalytically disabled Cas endonuclease with a cytosine or adenine deaminase domain, allowing more precise edits[155]. However, these base editors only allow the conversion of cytosine-to-thymine or adenine-to-guanine bases, limiting the method to specific target mutations. Recently, a promising prime editing technology that introduces all 12 base-to-base conversions has been applied to rice and wheat[156], overcoming the limitations of CRISPR base editors. Prime editing is composed of an engineered prime editing guide RNA (pegRNA) and a prime editor. The latter has a Cas9 nickase fused to a reverse transcriptase enzyme that performs the editing following pairing with the pegRNA. Further studies involving a broader range of species and target genes are still required to unravel the technique's full potential.

The requirement of Cas9 for a G-nucleotide-rich protospacer adjacent motif (PAM) site close to the cut site is another factor limiting high-efficiency genome editing in plants. For

example, there may be a lack of G-rich regions close to the target site of the gene of interest, such as untranslated and promoter regions of plant genomic DNA that are generally AT-rich. An alternative is the use of different nucleases, such as Cas12a (formerly Cpf1), which recognizes T-rich PAMs and requires a shorter single guide RNA (sgRNA)[157]. Cas12a is a promising strategy for nanotechnology-mediated genome editing as it is approximately 40 kDa smaller than Cas9, resulting in a smaller cargo that could be beneficial for nanoparticle-based delivery.

Successful CRISPR-Cas genome editing further relies on selection of the correct sgRNA to optimize Cas specificity to the plant genomic target and cleavage efficiency, and to avoid off-target editing[158,159]. Existing bioinformatics tools have poor correlation with in planta sgRNA editing efficiency[160]. Methods for the transient screening of sgRNA efficiency have been demonstrated in tobacco and wheat[161,162] but need development for other species.

Even with the capability to deliver CRISPR reagents to crops and make specific heritable mutations with no off-target effects, a remaining problem is that the functions of most plant genes are unknown[163]. A first step for both understanding gene function and performing targeted mutagenesis is having a well-annotated genome. Most major crop species have had their genomes sequenced, but these genomes vary in quality and many orphan crop genomes have yet to be sequenced[164]. In addition to genomic knowledge, information about gene function at the transcriptomic, proteomic and metabolomic levels is just as important for crop engineering[165]. As a further complication, there are complex biological interactions between these -omics levels. This may result in another type of off-target effect, wherein mutating the target gene indirectly affects the regulatory and metabolic connections to other genes[166]. With increases in data availability, quality assessment and access, plus high-throughput experimental validation in plants, we will more easily make predictions on gene function that can be used for crop CRISPR engineering[163].

2.4 Nanotechnology to address CRISPR challenges in plants

Initial studies of plant biomolecule delivery and genome editing with nanomaterials used larger (over 100 nm) particles necessitating their biolistic delivery to plants[140,167] (Figure (Figure 2.2). Subsequent developments have demonstrated that certain smaller nanoparticles can be delivered into plant cells without biolistic delivery, and that nanoparticles can deliver DNA and RNA cargoes to many plant species and target tissues[141–143,168–171]. See Table 2.1 for a roadmap summary for how nanotechnology could address key outstanding CRISPR challenges in plants.

Delivery

Delivery is a critical challenge in plants, as common abiotic transfection techniques (heat shock, electroporation, lipid- and polymer-mediated delivery) that are used for microbes and

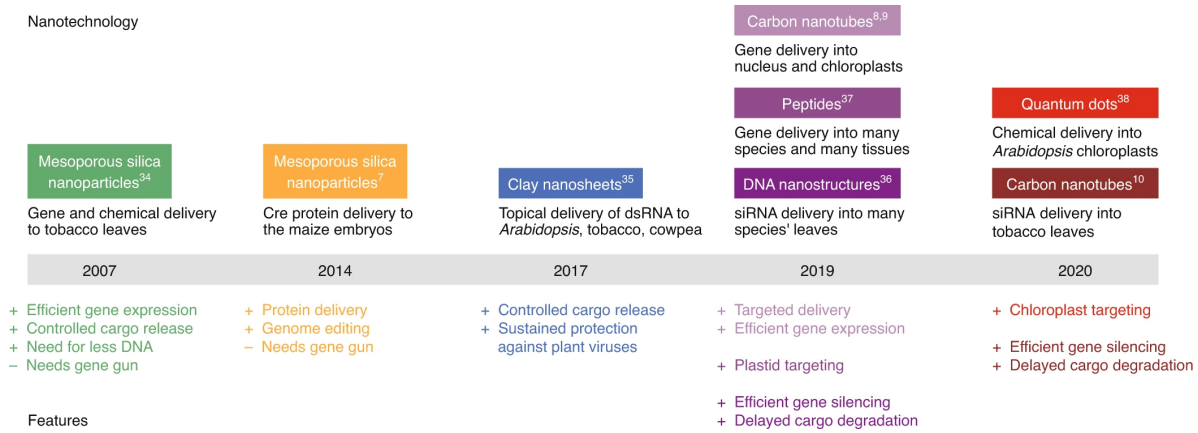

Figure 2.2: Schematic showing nanomaterials developed for plant biotechnology, delivery and genetic engineering. Nanotechnology (upper) used in plants and its features (lower). The first use of nanomaterials for plant delivery was by Torney and colleagues, where mesoporous silica nanoparticles biolistically delivered a gene to tobacco leaves. The same group used mesoporous silica nanoparticles for plant genome editing in 2014, by delivering Cre protein into maize embryos. In 2017, studies with RNA demonstrated the ability of nanomaterials to protect RNA cargoes from degradation. Parallel to RNA delivery, DNA delivery without biolistics was shown using carbon nanotubes and peptides. These studies showed that nanoparticles can be used to express genes in different subcellular locations, such as the nucleus and chloroplast, and that the nanotechnologies are compatible with a diverse set of plant species.

animals are typically ineffective in intact plants. Nanotechnology's biggest contribution to plant genetic engineering is in enabling efficient delivery into diverse plant species and tissues (Figure 2.1a). In addition to targeted delivery, controlled cargo release and cargo protection from degradation, certain nanoparticles allow imaging of cargo delivery and release processes in planta given their intrinsic or engineered fluorescent properties[172].

While delivering DNA and proteins into plant cells using nanomaterials has been successful, nanomaterial-mediated CRISPR-Cas genome editing in plants has not yet been reported due to the unique physicochemical properties of CRISPR reagents and the high delivery efficiencies needed to enable CRISPR genome editing in plants. DNA plasmids encoding for the CRISPR-Cas complex are substantially larger than reporter plasmids that are commonly used in nanoparticle proof-of-principle studies. Owing to the difference in plasmid size and net charge, nanomaterial researchers need to identify optimal chemistries for loading CRISPR DNA plasmids onto nanoparticles. In the case of Cas9 protein and RNP delivery, challenges stem from the large size of Cas9, its high local charge density and its low stability in ionic solutions. One possible solution is to covalently attach Cas9 RNPs onto the nanoparticle surface *via* a conjugation chemistry that can be cleaved in the vicinity of the

target. Several promising approaches involve enzymatically cleavable linkers and the use of tissue-penetrable near-infrared light to trigger release of the RNPs from the nanoparticle surface. Additionally, nanomaterial-mediated delivery is still less efficient than biotic delivery approaches; thus, increasing the delivery efficiency of CRISPR reagents is needed to enable genome editing for practical applications.

Tissue culture

Nanomaterial-based technologies that are developed for plant germline transformation could circumvent the need to regenerate plants from tissue culture, a major plant biotechnology limitation, and produce edited offspring directly. Towards circumventing regeneration, transformation of the pollen (the male gametophyte) is a promising method as edited plants can be generated directly through pollination with edited pollen. So far, there has been limited success in transforming pollen through either physical or biological methods due to the tough outer layer of pollen combined with its fragile viability following transformation. The unique mechanical properties of nanoparticles, such as the high tensile strength of carbon nanotubes, could be leveraged for CRISPR editing of pollen, though optimization is necessary to maximize the intake of nanoparticles by pollen without sacrificing its viability. Researchers can attempt the delivery of CRISPR DNA or RNPs through ˜5-μm diameter pollen surface apertures, where the outer pollen wall (exine) is thinner. A detailed investigation of pollen surface properties is needed to engineer nanoparticles for penetration of the pollen coat.

An alternative approach to pollen transformation is to edit the germline cells in intact flowers, where both the male and female gametophytes (ovules) reside. Administration of CRISPR reagents to flowers *via* nanoparticles has the potential to edit cells in all of the following locations: pollen, ovules and the embryo. Another promising tissue target for nanomaterials is the shoot apical meristem, from which whole edited plants can be generated with a reduced tissue culture and regeneration burden. However, most of these plant organs are buried deep inside plants; therefore, how to penetrate through multiple plant tissue layers remains to be solved.

Species dependence

One of the biggest bottlenecks for the widespread application of plant CRISPR genetic engineering is the inability of transformation tools to be effective for a wide range of plant species. There are several reasons for this plant species dependence: (1) the inability to deliver cargoes to all species, (2) challenges of in vivo sgRNA validation and (3) the PAM site requirement of nucleases with unsuitable genomic composition in certain species. Nanoparticles have facilitated many aspects of delivery into a diverse range of plant species, including Arabidopsis, tobacco, maize, wheat, arugula, spinach, cotton and watercress[140–142,171]. These promising studies suggest that the entry of nanoparticles into plant cells is likely a mechanical phenomenon, and thus is not heavily affected by plant genetics or signalling pathways.

In addition to delivery benefits, nanotechnology might offer a way to identify high-efficiency sgRNAs by rapidly screening sgRNAs for efficacy in planta. Since nanomaterial-mediated RNA delivery platforms are based on chemisorption of the polynucleotide cargo to the nanoparticle, and are indifferent to the polynucleotide cargo type[143,168,169], these nanoparticles could deliver sgRNA into Cas transgenic plants for high-throughput and rapid testing of sgRNA efficacy in vivo. Nanomaterial surface and conjugation chemistries will need to be optimized to enable tight binding of sgRNA for delivery into plant cells without irreversibly disturbing the three-dimensional structure of the sgRNA molecules, which is necessary for their function. Similar to in vivo sgRNA efficacy testing with nanomaterials, it is also possible to devise high-throughput tools to survey alternative nucleases with differing PAM sites to address specific PAM site limitations of current nucleases, or possibly to deliver mRNA molecules for DNA-free expression of CRISPR tools.

Low HDR efficiency

Nanotechnology could increase the HDR efficiency in plants through multiple approaches. Nanomaterials that enable efficient delivery of double- or single-stranded donor (template) DNA to the plant cell nucleus is one of these promising ways. Also, approaches that bring the donor DNA and Cas RNP into the proximity of the double-stranded break site in the plant genome can increase the HDR efficiency. Borrowing from a recent animal study[173], negatively charged nanoparticles can be used to increase the HDR efficiency in plants. Here, nanoparticles stabilize the Cas-sgRNA complex and carry a modified donor DNA interacting with Cas RNPs to shuttle the template to the nucleus. This approach has been shown to enhance the HDR efficiency approximately twofold to fourfold in human T cells, and could provide substantial enhancement in plants. The nanoparticle size should be designed appropriately to allow the stable carrying of RNP and donor DNA, while still being suitable for plant cell entry, which is a challenging balance.

To improve HDR editing efficiencies in plants, nanomaterials can also be exploited to achieve time-staggered delivery (and expression) of Cas, sgRNA and donor DNA. Many nanomaterials have already been used in animal systems for the sequential delivery of genetic material and drugs[174]. Translating these technologies into plants can circumvent some of the limitations of HDR. As RNA is not stable long-term inside plant cells, sgRNA could be delivered when Cas reaches its maximum cellular levels of expression. To achieve this, nanoparticles can aid either through the sequential delivery or controlled release of cargoes and/or by delaying the degradation of donor DNA and sgRNAs in plant cells. Promisingly, nanoparticle-mediated delivery platforms demonstrated for siRNA delivery may be indifferent to the polynucleotide type[143,168,169] and could thus be re-purposed for the direct delivery of donor DNA.

Table 2.1: Roadmap for nanotechnology to address CRISPR challenges in plants.

Challenges	Insights on nanoparticle solutions
Delivery	
Large size, high local charge density and low stability of Cas9 protein.	Covalent attachment Cas9 RNPs onto nanoparticle surfaces via cleavable chemical linkers to release the RNP in the target's vicinity: enzymatically cleavable linkers and the use of tissue-penetrable near-infrared light to trigger release of RNPs from the nanoparticle surface.
Donor DNA delivery.	Nanoparticle delivery is indifferent to the polynucleotide type and could be used for direct delivery of donor DNA into plant cells.
Tissue culture and regeneration	
Inability to transform plant germline cells.	Use of high tensile strength nanomaterials to transform pollen through large pollen surface apertures.
	Combined use of nanomaterials and other physical approaches such as microinjection for the transformation of flowers and shoot apical meristem.
Species dependence	
Inability to deliver cargoes to all species.	Entry of nanoparticles into plant cells is likely a mechanical phenomenon and may not be affected by plant genetics or signalling pathways.
Challenges of in planta sgRNA validation.	Nanoparticles could deliver sgRNA into Cas transgenic plants for high-throughput and rapid testing of sgRNA efficacy in planta.
Unsuitable genomic composition in certain species for the PAM site.	Devise high-throughput nanoparticle tools to survey alternative nucleases with differing PAM sites to address PAM site limitations of current nucleases.
Low HDR efficiency	
Limited simultaneous reach of Cas and sgRNA to the plant nucleus.	Use of negatively charged nanoparticles to stabilize the Cas–sgRNA complex and carry a modified donor DNA interacting with Cas RNPs to shuttle the template to the nucleus.
Challenges of in planta sgRNA validation.	Nanoparticles could deliver sgRNA into Cas transgenic plants for high-throughput and rapid testing of sgRNA efficacy in planta.

Generalizability of nanotechnology platforms for use in diverse plant systems

Differences in nanoparticle uptake and transport across plant tissues might affect the generalizability of nanotechnologies for plant genetic engineering with CRISPR. Leaves and roots are the most common nanomaterial uptake pathways in plants. In leaves, a waxy, hydrophobic cuticle with small pores (<5 nm) reduces the time nanomaterials spend on the leaf surface and inhibits their entry[172]. Instead, nanoparticles are more likely to enter leaves through the stomata, larger pores measuring tens of microns that regulate water and gas exchange. While stomata can comprise up to 5% of a leaf's surface, the location and number of stomata vary between plant species and their size can fluctuate depending on surrounding environmental factors[175]. The variability in leaf anatomy and morphology is an important consideration for nanotechnology generalizability between different plant tissues and species.

Regarding nanoparticle uptake by roots, there are conflicting reports of nanoparticle entry and translocation[176–178]. Most recently, Milewska-Hendel and colleagues demonstrated that gold nanoparticles did not translocate into or within roots by either apoplastic or symplastic pathways in barley[179]. These shortcomings are potentially due to additional barriers within root tissue, such as the root cortex and the Casparian strips of root endodermal cells. While research into the mechanisms for nanoparticle movement within tissues suggests that properties such as nanoparticle size, charge, stiffness and aspect ratio may play an important role[169,179], these properties may also influence the ability of nanomaterials to deliver large proteins, such as Cas9, through the cell wall's measured size-exclusion limit of ˜5-20 nm[180]. Bypassing this barrier and double-membranous organelles such as mitochondria, nuclei and chloroplasts is critical for intracellular localization within organelles. Further work is also needed to explore other variable factors that could affect nanoparticle transport between plant cells, such as pH and osmotic conditions, which will likely influence both the transport and the stability of nanomaterial-cargo complexes within a plant cell.

2.5 Regulatory considerations

In this section, we will discuss the regulation of genetically engineered crops and societal challenges that they face. We will also analyze the safety and regulatory aspects of nanotechnologies.

Regulation of genetically engineered crops and societal challenges

The regulation of genome-edited crops is a complicated issue. While regulations are important for public safety, genetically engineered crops may be over-regulated given that they pose no higher risks to human health and the environment than conventionally bred crops[181]. At present, safety testing for a single genetically engineered crop in the United States lasts over a decade and costs several million US dollars before being introduced to the market,

stifling innovation[182]. Furthermore, regulatory practices vary widely worldwide. The new 'SECURE' rule (that is, Sustainable, Ecological, Consistent, Uniform, Responsible, Efficient) introduced in 2020 by the US Department of Agriculture updates and streamlines regulatory processes to sustainably speed innovation in genetically engineered crop development[183]. This guidance places genetically engineered crops under regulatory oversight only if they contain foreign DNA from agricultural pathogens. In the case of CRISPR-Cas mutagenized plants, while vector DNA from pathogenic *Agrobacterium* is typically used to introduce the Cas protein, after the target gene has been mutated, the bacterial vector can be removed from the plant host genome with crossing. Thus, these CRISPR-Cas mutagenized crops are regulated on a 'product-basis' and do not fall under oversight by US regulatory agencies[184] but remain dependent on the lengthy process of plant breeding. A few CRISPR-edited crops have recently been introduced into this regulatory pipeline including corn, soybeans, mushrooms and camelina[184,185]. Canada, Argentina, Brazil, Japan and Australia have similar regulatory frameworks[186]. In the European Union, however, CRISPR-edited crops are regulated on a 'process-basis' and thus as conventional genetically engineered crops, based on the notion that the procedure to generate CRISPR crops does not occur in nature[187]. Notably, this rationale is inconsistent with other rules. For example, gamma irradiation is commonly used to generate new germplasms that are not regulated, and gamma irradiation does not occur naturally[188].

Safety and regulatory aspects of nanotechnologies

As nanotechnologies for plant systems evolve, there must be parallel efforts to better understand their safety implications and create effective regulatory policies. Early studies of nanotechnologies such as carbon nanotubes emphasized their non-biodegradable nature and likened their appearance to needle-like, carcinogenic asbestos fibres[189]. Other studies have instead correlated the toxic effects of nanoparticles with the presence of heavy-metal impurities introduced during their synthesis[190]. While many of these initial concerns have been ameliorated by subsequent research, toxicity and other safety concerns are still being addressed within the nanomaterial community.

While regulation broadly defines risk based solely on nanomaterial size, systematic studies of nanomaterial toxicology have shown that not all nanomaterials are equally toxic, with disparities being based largely on nanomaterial physical and chemical properties instead of size[191]. For example, the European Commission defines nanomaterials by a size range of 1-100 nm, without explicit consideration of size distribution, nanoparticle surface chemistry, synthetic route and purity or other material properties. Nanomaterials represent a broad class of substances of different sizes, shapes and compositions, determined not by a single value but by a distribution of values. This diversity of physicochemical properties makes classification of nanomaterials difficult. The lack of consensus about how to define and categorize nanomaterials has created a fragmented regulatory market that places a burden on researchers attempting to move research from the laboratory to the field. Many of the nanotechnologies commonly used for genetic engineering are regulated in the United States

under the Toxic Substances Control Act, which places the burden of proof on producers and importers of chemicals to demonstrate safety[192]. However, to our knowledge, there has been no government oversight of nanomaterial use in laboratories, greenhouses or in the field to date.

As such, for nanomaterial applications in CRISPR genetic engineering, we need to better understand the lifecycle of nanomaterials after cargo delivery to ensure that edited plants, their litter, progeny and consumers are free of nanomaterials. This path will allow for the development of new nanotechnologies with minimal safety concerns and offers exciting opportunities for the remarkable reduction of regulatory barriers.

2.6 Conclusion

CRISPR-Cas plant genome editing has shown success in several plant species following traditional transformation and regeneration procedures. However, there are still many challenges regarding the range of plant species that can be genetically engineered through this approach, the time and labour input required for plant regeneration, and the types of CRISPR edits that can be routinely and efficiently achieved in plants. We have discussed how nanomaterials could make an impact on addressing each of these challenges. Nonetheless, many outstanding questions surrounding the use of nanomaterials for plant genome editing persist (Table 2.2). First, an upper limit for the nanoparticle-loaded cargo size and amount has not yet been established for CRISPR DNA and protein cargoes, and this is likely to be dependent on the nanoparticle type and surface chemistry. Second, despite the successful delivery of certain nanoparticles into the plant chloroplasts, it remains unknown whether or not these nanoparticles can carry CRISPR reagents to plant plastids and mitochondria for modification of their genomes. Third, more studies are needed to establish the compatibility of nanoparticles with plant tissue culture and regeneration protocols, in the cases where germline transformation is not plausible. Last, would the regulation of plants engineered *via* nanoparticles be different from traditionally engineered plants? To answer this question, the persistence of nanoparticles in the offspring of edited plants should be determined.

As seen in Table 2.2, there are various outstanding questions, which call for attention from a diverse set of researchers, industry and policymakers for progress in nanomaterial-mediated plant genetic engineering. Further development of nanoparticle chemistries and a better understanding of plant-nanomaterial interactions, delivery routes, and health and environmental risks are all key steps in the path towards widespread applicability. To facilitate this transition, the plant nanotechnology community could draw on lessons from the field of nanomedicine's experience translating benchtop research into clinical applications. In both medicine and plant agriculture, researchers and regulators must consider complex biological environments, human exposure, limited reproducibility and the challenges of scale-up and cost. Building on these lessons, we encourage the agriculture sector to develop a unified pathway to foster academia-industry collaborations that include stakeholders such as fertilizer and pesticide producers, speciality chemical companies and large- and small-scale farmers.

Table 2.2: Outstanding questions of nanomaterial-mediated CRISPR editing in plants.

Broad Categories	Specific Outstanding Questions
Technological unknowns	What is the upper limit of DNA and protein size and amount that can be efficiently delivered by nanomaterials?
	Can nanoparticles target CRISPR reagents to chloroplasts and mitochondria, especially in grass species?
	Can nanomaterials enable pollen transformation through an optimum balance between the pollen's tough exine and its susceptibility to damage following transformation?
	How does the frequency of off-target editing compare between canonical and nanomaterial-mediated CRISPR delivery?
	Are nanomaterials compatible with current plant tissue culture and regeneration protocols?
Safety and regulation	Would the regulation of edited plants using nanoparticles be different from traditionally edited plants?
	Do nanoparticles persist in downstream generations of edited plant offspring?
	What are the environmental lifecycles and safety implications of nanomaterials on microbes and animals?
Broad use	When will these nanotechnologies be widely available and routinely used in plant biotechnology?
	Does the future of nanotechnology in plants include commercially available nanoparticles or will people need to make their own?
	What is the overall cost of obtaining nanoparticle-mediated CRISPR-edited plants? How does this compare with conventional methods?
Novel applications in the future	Will nanomaterial-mediated CRISPR be effective in creating customized genetic mosaics for experimentation?
	Can somatic CRISPR manipulations be done in the field?
	Can gene replacement and allele swapping be done in plants?
	Can we induce transformation on an as-needed basis?

Chapter 3

Polymer-conjugated carbon nanotubes for biomolecule loading

3.1 Chapter abstract

Nanomaterials have emerged as an invaluable tool for the delivery of biomolecules such as DNA and RNA, with various applications in genetic engineering and post-transcriptional genetic manipulation. Alongside this development, there has been an increasing use of polymer-based techniques, such as polyethylenimine (PEI), to electrostatically load polynucleotide cargoes onto nanomaterial carriers. However, there remains a need to assess nanomaterial properties, conjugation conditions, and biocompatibility of these nanomaterial–polymer constructs, particularly for use in plant systems. In this chapter, we develop mechanisms to optimize DNA loading on single-walled carbon nanotubes (SWNTs) with a library of polymer-SWNT constructs and assess DNA loading ability, polydispersity, and both chemical and colloidal stability. Counterintuitively, we demonstrate that polymer hydrolysis from nanomaterial surfaces can occur depending on polymer properties and attachment chemistries, and we describe mitigation strategies against construct degradation. Given the growing interest in delivery applications in plant systems, we also assess the stress response of plants to polymer-based nanomaterials and provide recommendations for future design of nanomaterial-based polynucleotide delivery strategies.

3.2 Introduction

Genetic engineering is a critical component of biomedical research, healthcare, biopharmaceuticals, and agriculture. Central to these applications is the ability to deliver biomolecular

Chapter 3 is reproduced from work previously published as Jackson, C.T.; Wang, J.W.; González-Grandío, E.; Goh, N.S.; Mun, J.; Krishnan, S.; Geyer, F.L.; Keller, H.; Ebert, S.; Molawi, K.; Kaiser, N.; Landry, M.P. Polymer-Conjugated Carbon Nanotubes for Biomolecule Loading. ACS Nano 2022, 16, 2, 1802-1812. https://doi.org/10.1021/acsnano.1c06343.

cargoes such as DNA, RNA, or proteins to the inside of cells. This delivery challenge affects the efficiency of resulting genetic transformations and the ease and throughput of advancing bioengineering applications. In particular, the low biomolecular cargo delivery efficiencies in plant systems motivate the development of tools for more effective intracellular delivery of biomolecular cargoes such as polynucleic acids. Nanomaterial–polymer conjugates have the potential to overcome many shortcomings of conventional delivery systems, including low efficiency, species dependence, limited cargo types, and tissue damage[180].

Nanoparticles have been widely used in both mammalian and plant systems for the delivery of biomolecular cargoes. For example, conjugated polymer nanoparticles were shown to effectively penetrate tobacco BY-2 protoplasts within 2 h of delivery for small interfering RNA (siRNA) delivery and gene knockdown[193]. Similarly, polymer compositions for DNA delivery have been demonstrated in moss and tobacco protoplasts, where delivery efficiency is dependent on the chemical structure and molecular weight of the polymer carriers[194]. The formation of ionic complexes that combine a polycation with a cell-penetrating peptide has also enabled the delivery of DNA to intact leaf cells[195]. In both plant and mammalian systems, PEI remains one of the most commonly used cationic polymers for DNA delivery. The delivery capabilities of these PEI-based systems have been broadly attributed to their ability to escape endosomes *via* a "proton sponge" mechanism. When placed in an acidic endosomal environment, the polymer's amine groups become increasingly protonated, leading to a buffering effect. As protons (and typically chloride ions, which maintain charge neutrality) enter the vesicle, they cause osmotic swelling and rupture, freeing the nanoparticle and/or its cargo[196]. However, as is the case with many cationic polymers, aggregation of PEI-DNA, which occurs largely due to hydrophobic interactions, limits their utility for gene delivery[197]. Furthermore, the high charge densities present in cationic polymers such as PEI can induce cytotoxicity, as demonstrated previously in nonplant systems[180,198]. Mitigating techniques, including cationic polymer cross-linking, chemical modification of the cationic polymer, and modulation of DNA structure, can more effectively condense DNA to increase transfection efficiency and limit toxicity[199–202].

Toward these ends, the conjugation of cationic polymers such as PEI to nanoparticles has been demonstrated to improve transfection efficiency, relative to free PEI polymers, in mammalian cells[203,204]. Importantly, particle size and zeta potential absolute magnitude are key for internalization of nanoparticles within an organelle[205]. Early reports demonstrated the use of Au-PEI nanoparticles to bind RNA *via* electrostatic interaction and deliver the cargo in mammalian cells with cytocompatibility and improved gene silencing compared to polymer alone[204]. More recent reports have combined low-dimensional nanomaterials, such as SWNTs, with cationic polymer systems for delivery in diverse plant tissues and mammalian cells[141,206].

Despite the success of polycationic polymers and their nanomaterial conjugates for polynucleotide delivery, there remains a lack of consensus on the optimal design of polymer-nanoparticle complexes that maximize nanoparticle stability, delivery efficiency, and biocompatibility[207]. Herein, we explore the use of polymer-conjugated SWNT nanoparticles and the material properties that govern their use in biomolecule delivery. We next optimize

polymer-conjugated SWNT nanoparticle biocompatibility for use in plant systems, which remain less well studied than their mammalian counterparts and face additional barriers to cellular entry such as the cell wall. To these ends, we synthesized polymer-SWNTs using a library of cationic polymers conjugated with two chemical techniques to assess their relative functional density, dispersibility, and long-term stability. We further investigated the impact of preparation techniques and cationic polymer design in the stability and DNA loading ability of the resulting polymer-SWNT systems. Finally, we assessed plant stress responses to these nanoparticle–polymer conjugates in vivo to provide insight into rational polymer–nanoparticle design to optimize DNA loading, construct stability, and minimize toxicity.

3.3 Results and Discussion

Name	**Abbreviation**	**Molecular weight, M_w [g/mol]**[1]	**Polydispersity index**[2]
Branched polyethylenimine (800)	BPEI-800	800	0.212 ± 0.043
Linear polyethylenimine (5000)	LPEI-5000	5000	0.563 ± 0.116
Branched polyethylenimine (750k)	BPEI-750k	750,000	0.352 ± 0.044
Branched polyethylenimine (25k)	BPEI-25k	25,000	0.379 ± 0.048
Branched polylysine	-	3,500	0.778 ± 0.125
Linear polyethylenimine (800)	LPEI-800	800	0.633 ± 0.139
Low hydrophobic modified branched polyethylenimine	low-phi-BPEI	25,000 - 30,000	0.131 ± 0.017
Medium hydrophobic modified branched polyethylenimine	med-phi-BPEI	1,500 - 2,000	0.448 ± 0.154

Generating Polymer-SWNT Constructs

We selected a library of cationic polymers (Table 3.3) commonly used for polynucleotide delivery applications, with ranging physicochemical properties including molecular weight, amine density, and structure: linear vs branched. We also developed two attachment chemistries to covalently link polymers to the SWNT surface: EDC-NHS and triazine chemistries. For EDC-NHS based polymer attachment, commercially available carboxylic

acid functionalized SWNTs (COOH-SWNTs) were modified *via* EDC-NHS chemistry to form a covalent amide bond to the amine groups of the cationic polymers in our library (Figure 3.1a)[208]. The attachment of polymer was confirmed by zeta potential measurements, with a notable change from the initial -50.1 mV for COOH-SWNTs to +67.7 mV after conjugation of a cationic polymer such as 25,000 MW branched PEI (BPEI-25k) (Figure 3.1b), with all zeta potential values listed in Table 3.1.

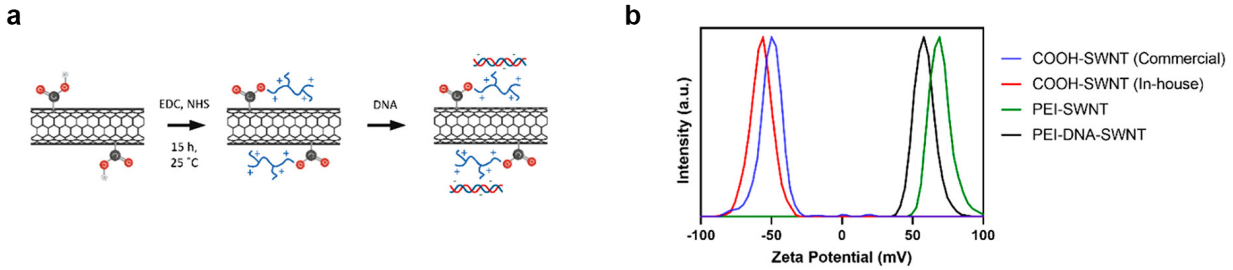

Figure 3.1: Synthesis and characterization of polymer-SWNTs using EDC-NHS chemistry. (a) Scheme of polymer-SWNT synthesis using EDC-NHS chemistry and subsequent DNA loading. **(b)** Zeta potential measurements of initial COOH-SWNT constructs, after conjugation with BPEI-25k *via* EDC-NHS chemistry and after addition of DNA.

In the second method, triazine-functionalized SWNTs (Trz-SWNTs) were synthesized from pristine SWNTs *via* a rearomatization reaction to generate triazine groups on the SWNT surface[209]. These Trz-SWNTs were further functionalized *via* a nucleophilic substitution of the chlorine on the triazine with a polymer amine group to create Trz-SWNTs with a covalently attached BPEI-25k polymer (Figure 3.2a). Given the prolific use of this BPEI-25k polymer for polynucleotide delivery applications over others in our library, we only synthesized the BPEI-25k polymer-SWNT complex with this triazine-based chemistry for comparison against EDC-HNS based polymer attachment. The attachment of the BPEI-25k polymer was confirmed by zeta potential measurements, with an increase in zeta potential from -6.30 mV to +36.0 mV after conjugation of BPEI-25k (Figure 3.2b).

Improved Functionalization Density and Removal of Amorphous Carbon

The efficiency of polymer-SWNT conjugation depends on the purity of the starting COOH-SWNT material and the density of COOH functional groups on the COOH-SWNT. Thus, we first implemented thermogravimetric analysis (TGA) of COOH-SWNTs, as received from the supplier, to assess the purity of the COOH-SWNT starting material. Previous literature indicates that both pristine SWNT and COOH-SWNT are thermally stable below 600

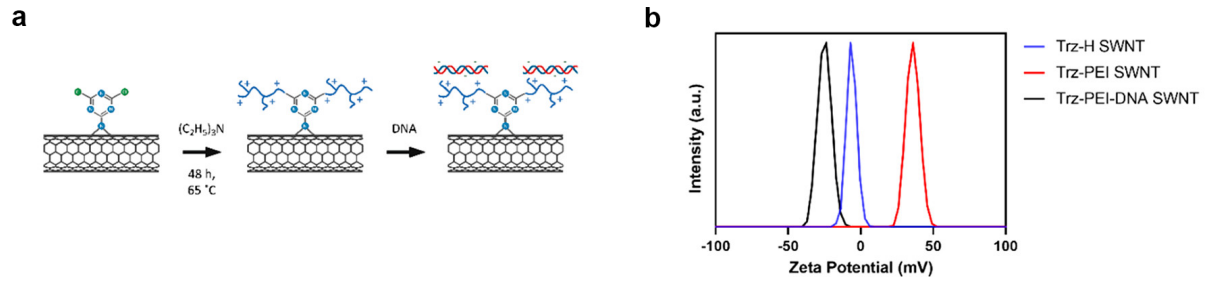

Figure 3.2: Synthesis and characterization of polymer-SWNTs using triazine chemistry. **(a)** Scheme of polymer-SWNT synthesis using triazine chemistry and subsequent DNA loading; **(b)** Zeta potential measurements of triazine-functionalized SWNTs, after conjugation with BPEI-25k *via* nucleophilic substitution and after addition of DNA.

°C[210,211]. Upon heating samples to this temperature and accounting for the removal of impurities such as excess solvent below 150 °C, we observe a 81.6% loss in mass in the commercially-procured COOH-SWNT. On the basis of previous literature, we attributed this mass loss to the combustion of amorphous carbon in the sample (Figure 3.3a), suggesting the as-procured COOH-SWNT material is composed predominantly of amorphous carbon material not viable for delivery applications[210,212].

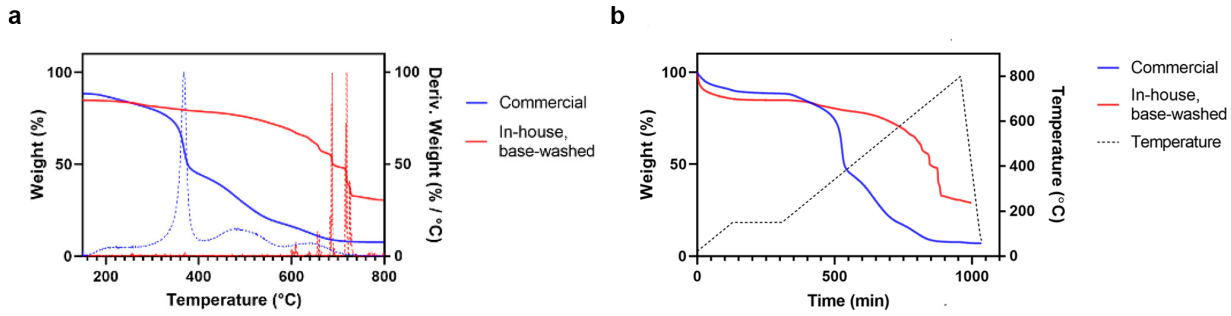

Figure 3.3: Quantification of amorphous carbon via thermogravimetric analysis. **(a)** TGA measurements of COOH-SWNTs either purchased commercially or carboxylated in-house *via* reflux in nitric acid and washed with 1.0 M NaOH. **(b)** TGA heating profile. Temperature was increased from room temperature to 150 °C, held for 3 hours, then gradually raised to 800 °C before being rapidly cooled.

To mitigate manufacturer variability, we performed an in-house carboxylation reaction by refluxing pristine SWNTs in concentrated nitric acid[213]. These SWNTs were subsequently

washed *via* vacuum filtration and characterized. The negative zeta potential of our in-house carboxylated SWNTs was -56.9 mV, which is consistent with that of commercially available COOH-SWNTs (-50.1 mV) (Figure 3.1b) and provides one confirmation of a successful reaction. X-ray photoelectron spectroscopy (XPS) characterization of this product (Figure 3.5c) further confirmed a high degree of in-house produced COOH-SWNT carboxylation, notably higher than that of the commercially procured COOH-SWNT (Figure 3.4). COOH-SWNTs synthesized *via* this technique demonstrated notably little (19.3%) mass loss *via* TGA analysis, representing a more than 4-fold increase in purity compared to commercially purchased COOH-SWNTs (Figure 3.3a).

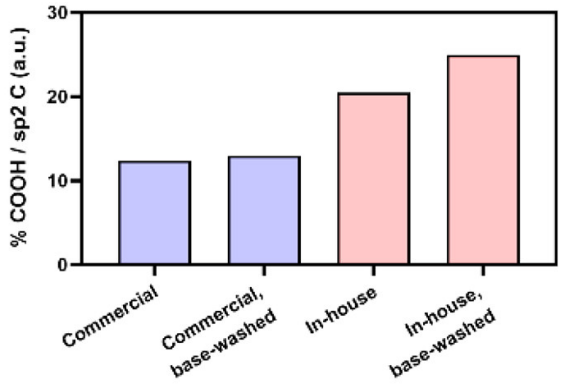

Figure 3.4: Quantification of SWNT carboxylation via XPS. Bar plot displaying carboxyl group peak area, normalized in relation to sp^2 C peak area in C 1s XPS spectra.

To test whether carboxylation resides predominantly on the SWNT surface compared to on amorphous carbon, we washed commercially purchased carboxylated SWNTs with a 1.0 M NaOH solution to remove amorphous carbon[214]. A colored filtrate was recovered, which has been previously attributed to the presence of oxidation debris[215]. XPS characterization before and after washing suggests that both commercially purchased (Figure 3.5a) and in-house synthesized COOH-SWNTs (Figure 3.5c) contain a high percentage of ester groups (Table 3.2). The subsequent decrease in these ester groups after a base wash treatment suggests that these functional groups are primarily located on amorphous carbon rather than on the SWNT surface. This result is consistent with previous published literature, which suggests that upon reaction with concentrated acid, oxidation debris from amorphous carbon coats the SWNT walls, preventing covalent functionalization of the SWNT surface[215,216]. As a practical result, it is likely that a majority of carboxyl-functionalized carbon material, which is subsequently conjugated to cationic polymers, is largely removed during wash steps. Any amorphous carbon that is not removed still adsorbs DNA but lacks the material properties, including tensile strength and high aspect ratio, that have been shown to enable DNA delivery[141–143]. Importantly, COOH-SWNTs synthesized *via* an in-house carboxyla-

tion reaction followed by base wash demonstrated the highest degree of carboxylation of all treatments tested (Figure 3.4, Figure 3.5d) and are thus the best suited starting material for downstream delivery applications.

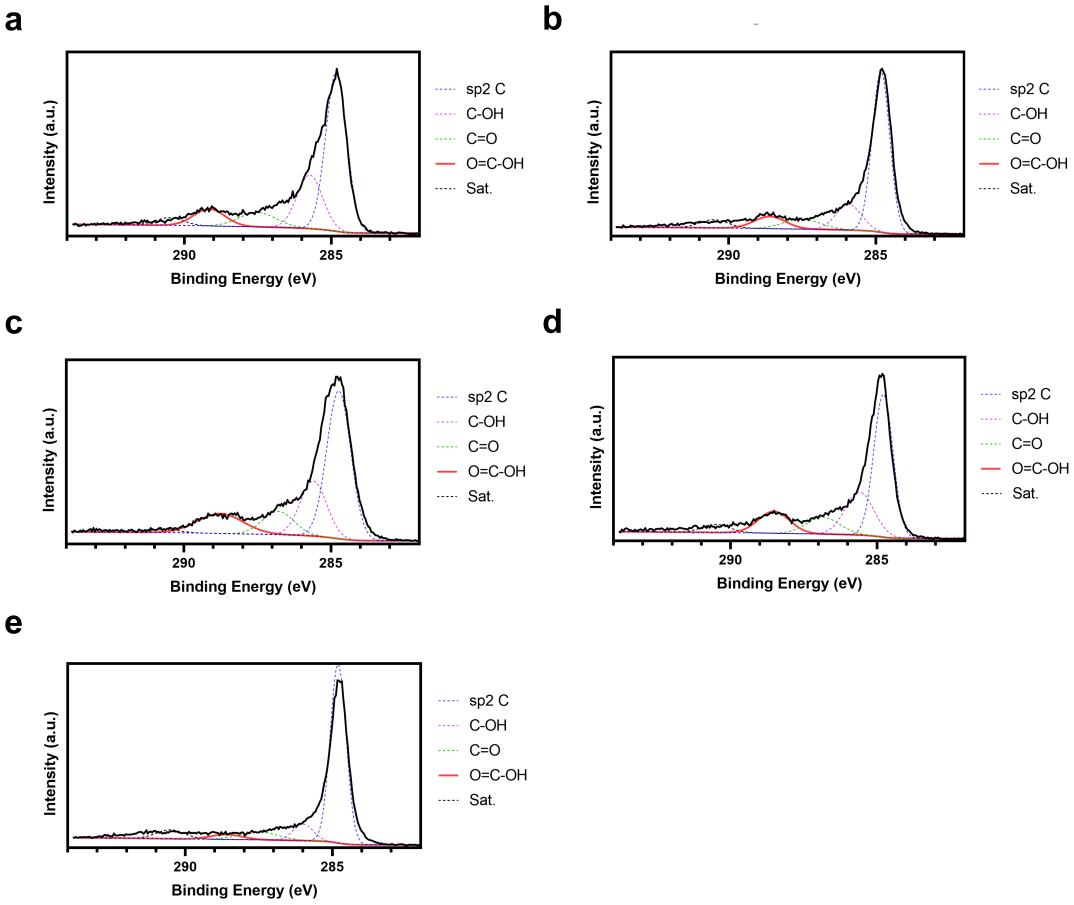

Figure 3.5: XPS spectra of carboxylated-SWNT preprations. **(a)** XPS C1s spectra of commercially purchased COOH-SWNT. **(b)** XPS C1s spectra of commercially purchased COOH-SWNT after wash treatment with 1.0 M NaOH. **(c)** XPS C1s spectra of in-house carboxylated COOH-SWNT. **(d)** XPS C1s spectra of in-house carboxylated COOH-SWNT after washing with 1.0 M NaOH. **(e)** XPS C1s spectra of pristine SWNT.

Removal of Unreacted Residual Polymer

In this study, we tested the conjugation of eight cationic, amine-containing polymers to SWNTs: three branched PEI (BPEI; 800, 25K, and 750K Da), two linear PEI (LPEI; 800

and 5000 Da), two hydrophobically modified branched PEI (low-phi-BPEI, low degree of modification, 25–30K Da; and med-phi-BPEI, medium degree of modification, 1500–2000 Da), and a branched polylysine (3500 Da) (Table 3.3) using the aforementioned EDC-NHS chemistry. It has been previously demonstrated that free polymer will bind DNA in solution, preventing its adsorption to nanoparticles of interest[197,200–202]. Furthermore, polymer-DNA constructs have shown limited success for delivery of DNA in whole plant systems due to barriers such as cell membranes or the plant cell wall[195]. Therefore, the removal of unreacted polymer is critical for the viability of polymer-SWNT nanomaterials for DNA delivery. To this end, following the reaction of 1 mg of functionalized COOH-SWNTs with cationic polymers using EDC-NHS chemistry, we tested the efficacy of various washing methods in their ability to remove the large excess of unreacted free polymer and recover pure polymer-SWNT product. First, polymer-SWNT constructs were spin washed *via* centrifugation at high speed through a 100 kDa spin filter until only 1 mL of solution remained. 4 mL of water was added to the remaining solution, and this water wash was repeated a total of six times. The filtrate containing free polymer was collected after each wash step. Alternatively, polymer-SWNT constructs were washed *via* vacuum filtration through a fritted filter with a 0.45 μm PTFE membrane. An equivalent volume of water to that used during the spin wash process (˜4 mL) was used during each wash step, and the filtrate containing free polymer was collected after each step for a total of six times.

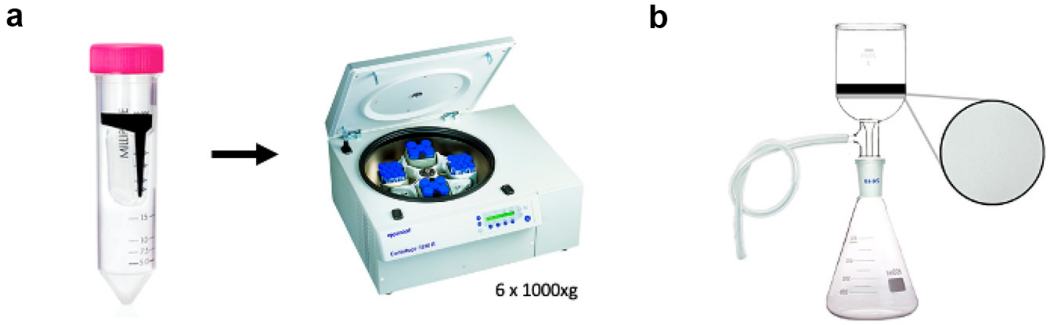

Figure 3.6: Free polymer removal from polymer-SWNT complexes. **(a)** Schematic of polymer-SWNT washing via spin filtration. **(b)** Schematic of polymer-SWNT washing via vacuum frit filtration.

To test the purity of the polymer-SWNT samples as a function of the wash step, filtrates from each wash were added to solutions of plasmid DNA and run on an agarose gel. If any free polymer was to be present in the filtrate, it would bind to the plasmid DNA and result in retention of DNA from running into the gel. Indeed, we observe no bands after the first wash, indicating the presence of free polymer that binds the plasmid and prevents its migration into the gel during electrophoresis (Figure 3.7a). By the sixth wash, we no

longer observe polymer in the filtrate solution, regardless of polymer type, as indicated by the migration of plasmid through the gel equidistant to that of the control free plasmid (Figure 3.7b). Testing of the filtrate after each wash step for our BPEI-25k polymer-SWNT construct demonstrates that the filtrate is largely free of polymer by the fourth wash step (Figure 3.7c).

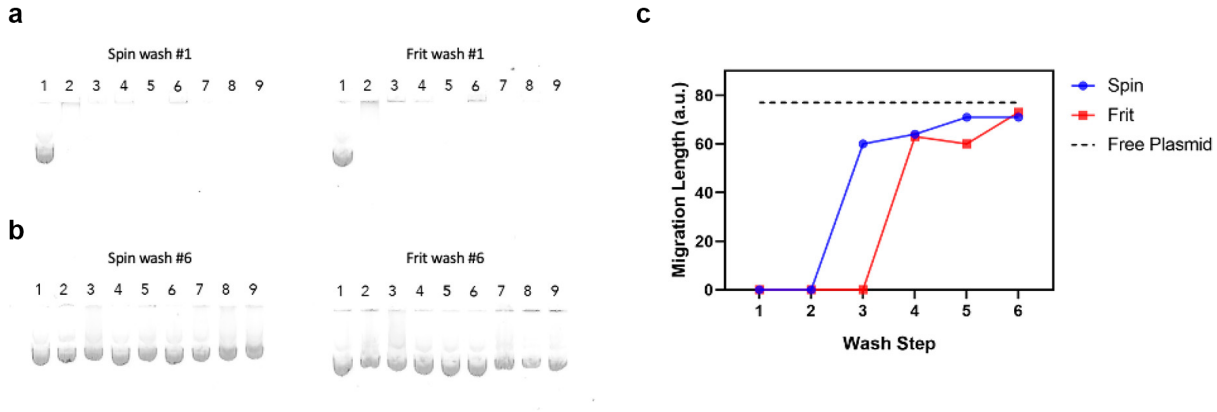

Figure 3.7: Agarose gel assay of polymer removal. **(a)** Filtrate from the first polymer-SWNT wash step loaded with DNA and run on an agarose gel for all polymers. **(b)** Filtrate from the sixth polymer-SWNT wash step loaded with DNA and run on an agarose gel for all polymers. From left to right: (1) free plasmid, (2) LPEI-5000, (3) LPEI-800, (4) BPEI-800, (5) low-phi-BPEI, (6) branched polylysine, (7) med-phi-BPEI, (8) BPEI-750k, (9) BPEI-25k. **(c)** Measurements taken after each wash step for BPEI-25k polymer-SWNTs show a steady increase in the plasmid migration distance, corresponding to a decrease in free polymer, after each wash step.

We further tested the effects of the pH of the wash solution to optimize removal of free polymer (Figure 3.9). In spite of its widespread use, the protonation state of PEI is not well understood; previous studies have suggested that approximately 55% of amine groups are protonated under physiological conditions (pH ~7.4)[218]. Wash treatments at pH levels both above and below this pH 7.4 threshold could cause differentially protonated amine groups, impacting the solubility and thus ability of PEI polymers to be removed during the wash process. Generally, we observe that higher pH washes corresponded to a lower zeta potential of the final purified polymer-SWNT sample. We hypothesize that this is due to the poor removal of free polymer, which has a zeta potential that ranges from neutral to weakly positive (Figure 3.10). This hypothesis is further confirmed by the larger size observed by DLS for constructs with the lowest zeta potential, which can also likely be attributed to a large amount of residual polymer in solution and aggregation of the final product (Figure 3.9).

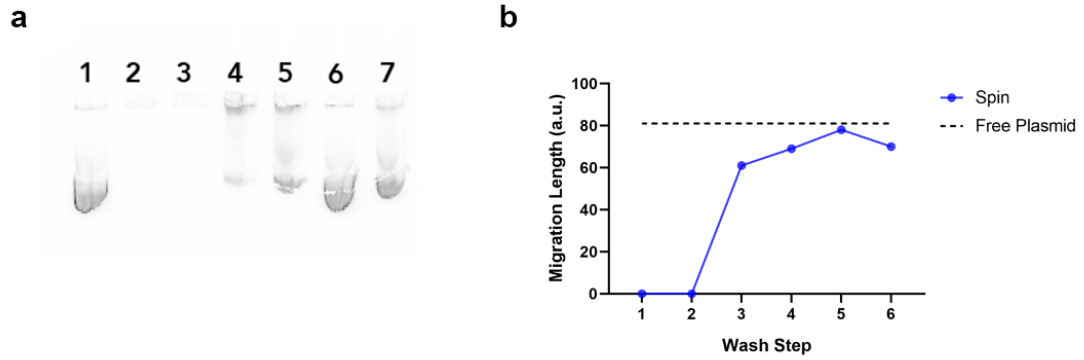

Figure 3.8: Washing of BPEI-25k polymer. Free BPEI-25k polymer suspended in water at 8 mg/L was washed six times with water through a 100 kDa spin filter at 1000 xg. The filtrate was collected after each wash step, loaded with DNA, and run on an agarose gel. By the fourth wash step, the filtrate loaded with DNA ran equidistant to free plasmid, suggesting that no free polymer remains in solution.

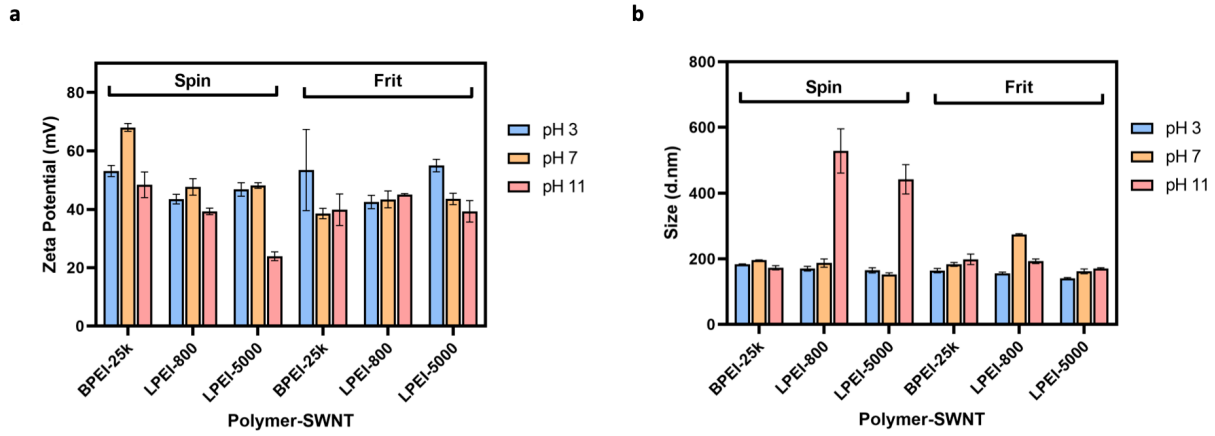

Figure 3.9: Zeta potential of polymer-SWNTs washed at varying pH. We attribute a lower zeta potential value to the poor removal of free polymer. **(a)** Zeta potential of washed polymer-SWNTs. **(b)** DLS size measurements for washed polymer-SWNTs. Error bars represent standard deviation of the mean (N = 3).

Probing Long-Term Stability of Polymer-SWNTs

Once we confirmed the covalent conjugation of polymers to the SWNT surface and their successful purification from residual unreacted polymer, we examined the long-term stability

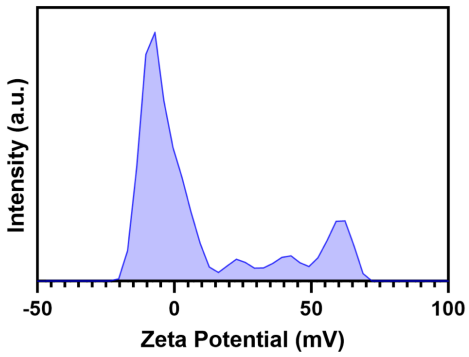

Figure 3.10: Zeta potential of BPEI-25k polymer in water. Free polymer suspended in solution exhibits a neutral or weakly positive charge, likely due to intermolecular interactions. When free polymer is suspended with positively charged polymer-SWNT nanoparticles, this can increase the ionic strength of the suspension and lower the measured zeta potential of the whole solution.

of polymer-SWNT conjugates in water. Given the challenges of nanoparticle use in diverse biological environments, including biofouling *via* protein adsorption, loss of colloidal stability, and toxicity, the stability of the nanomaterial polymer bond is critical for a diverse array of applications[26]. For delivery applications, the strength of covalent polymer attachment to nanoparticle surfaces is commonly assumed to be robust against breakage over conditions relevant to polynucleotide delivery; however, our stability assays below suggest otherwise.

To test the long-term stability of the polymer-SWNT conjugate, we synthesized polymer-SWNT constructs as described above, including six water wash steps, to confirm our final product contained purified polymer-SWNTs. Subsequently, we allowed our polymer-SWNT constructs to age in water at ambient conditions for 30 days postsynthesis. As previously demonstrated, we are able to successfully remove all unreacted free polymer after synthesis; therefore, all subsequent measurements can be attributed to polymer that has dissociated from the nanomaterial surface over time. Zeta potential measurements of polymer-SWNT samples conducted at the start and end of this 30 day time period show a substantial decrease in zeta potential, with the emergence of peaks corresponding to less positively charged particles as a function of time (Figure 3.11). We attribute the appearance of these secondary peaks to both free polymer that is no longer conjugated to our SWNT surface as well as polymer-SWNT conjugates with a decreased amount of attached polymer.

We do not observe any peaks at a negative zeta potential that would correspond to SWNTs without any bound polymer (Figure 3.1b), indicating that there is still a substantial amount of polymer attached to our constructs regardless of polymer type. We further confirmed this polymer-SWNT bond instability by XPS analysis, where we see a notable decrease in the N 1s peak in an aged polymer-SWNT sample compared to a freshly synthe-

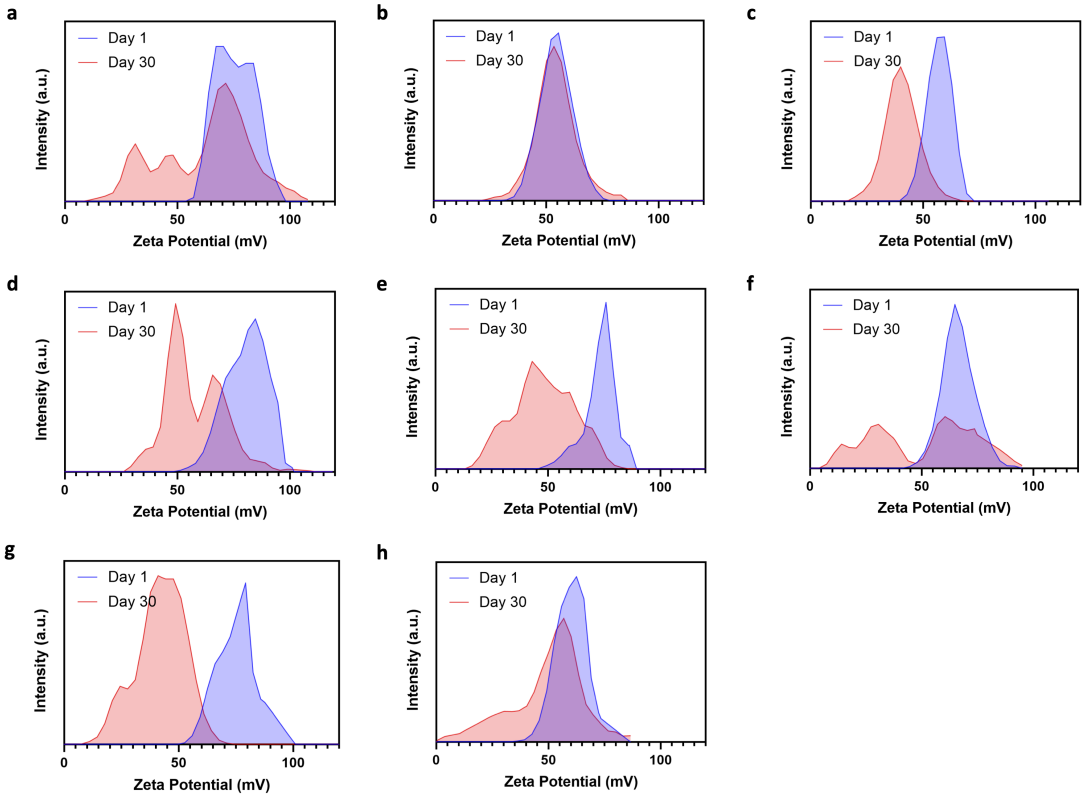

Figure 3.11: Zeta potential measurements of polymer-SWNT immediately after synthesis and after 30 days. **(a)** BPEI-25k, **(b)** BPEI-800, **(c)** LPEI-5000, **(d)** BPEI-750k, **(e)** branched polylysine, **(f)** LPEI-800, **(g)** low-phi-BPEI, **(h)** med-phi-BPEI.

sized batch (Figure 3.12), providing further evidence of the loss of polymer from the SWNT surface *via* hydrolysis of the polymer-SWNT covalent bond over time.

Lastly, to further confirm polymer-SWNT degradation over time, a freshly synthesized sample of polymer-SWNT was flash-frozen in liquid nitrogen and stored at -80 °C for 30 days. After being thawed, the zeta potential of this sample showed minimal polymer desorption (Figure 3.13).

Each polymer showed different rates of hydrolysis from the SWNT surface (Figure 3.11). To quantify the relative loss in polymer for each polymer-SWNT sample, we calculated the percentage overlap between zeta potential peaks measured at days 1 and 30 for each polymer-SWNT construct (Figure 3.14), where a higher overlap value represents greater polymer-SWNT stability. We find that both very small and very large PEI polymers disassociate from the SWNT surface rapidly relative to their medium-sized counterparts. In addition, polymers with lower amine density, including LPEI-5000, LPEI-800, and branched polylysine, likewise

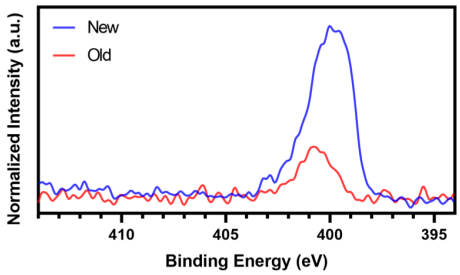

Figure 3.12: N 1s XPS spectra of a fresh and aged BPEI-25k polymer-SWNT sample, normalized to the respective C 1s peak.

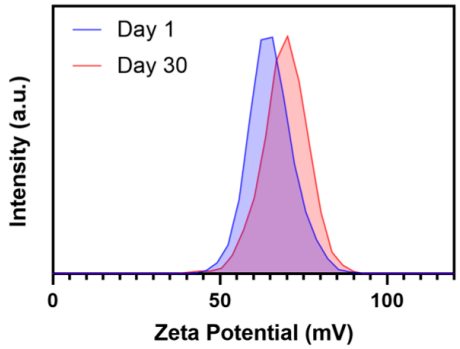

Figure 3.13: Zeta potential of BPEI-25k polymer-SWNT immediately after synthesis and after storage at -80 °C for 30 days.

showed poor stability relative to polymers with high amine density, which may be attributed to the relatively lower availability of amines for covalent conjugation to the SWNT surface. We also observe more polymer loss from the SWNT surface for low- versus medium-phi-BPEI polymers, suggesting that increasing polymer hydrophobicity may aid in long-term polymer–nanoparticle stability. These results indicate that we can attribute polymer-SWNT stability to several factors, including polymer amine density (higher is better), sterics (less steric hindrance is better), and polarity (more hydrophobicity is better). Together, our experiments suggest that a compromise between polymer size and structure may be ideal, as exemplified by the BPEI-800 polymer which showed especially high stability on the SWNT surface over time. Taken together, based on our experiments and previous literature, we attribute the loss of polymer from the SWNT surface to hydrolysis of the amide bond over time[219].

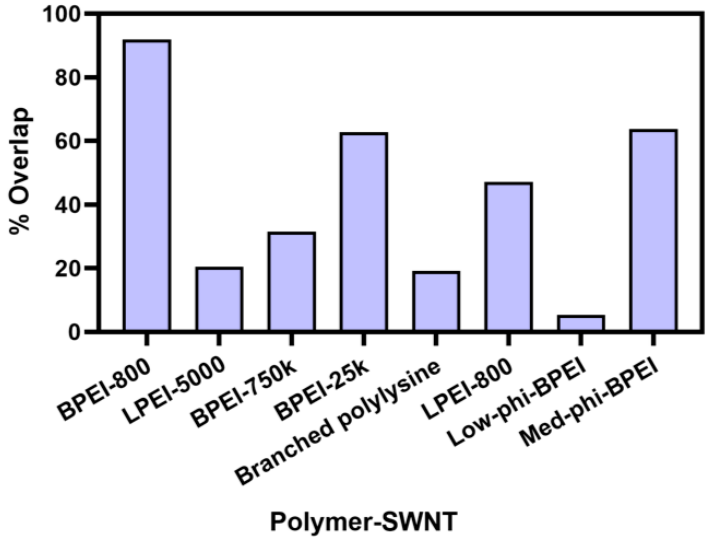

Figure 3.14: Desorption of polymer from polymer-SWNT nanoparticles over time. Quantification of the area under the curve overlap in zeta potential spectra peaks between days 1 and 30 for each polymer-SWNT construct.

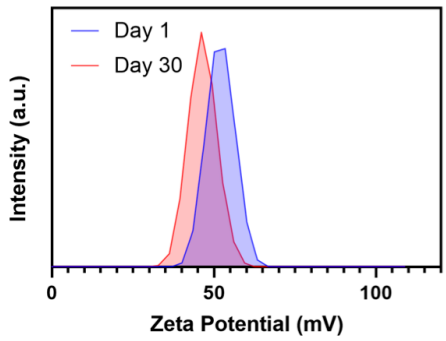

Figure 3.15: Desorption of polymer from BPEI-25k-Trz-SWNT nanoparticles over time.

To probe the effect of alternative bonding chemistry on polymer stability, we performed the same time course study of polymers attached to SWNT with a different attachment chemistry. Specifically, instead of the commonly used EDC-NHS chemistry, we attached the BPEI-25k polymer to SWNT *via* triazine chemistry. This chemistry proceeds *via* a covalent

functionalization reaction that rearomatizes SWNT defect sites to restore the original, pristine SWNT lattice and yields functional groups on approximately 1.64% of carbons on the SWNT surface[209]. After 30 days at ambient conditions, we observe minimal change in the zeta potential (Figure 3.15), despite the fact that the EDC-NHS chemistry performed above proceeds with COOH-SWNT starting material containing the same or more functional group density on the SWNT lattice than triazine chemistry. These results suggest that triazine-based attachment chemistries could be more viable for applications where long-term stability of the polymer–nanoparticle construct is necessary.

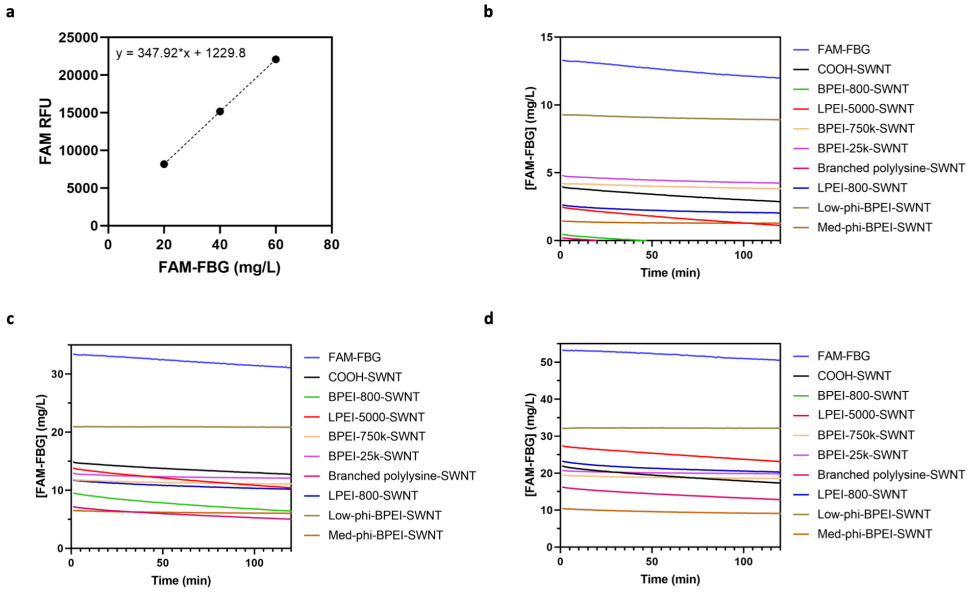

Figure 3.16: Quantification of real-time FAM-fibrinogen adsorption to polymer-SWNTs. **(a)** FAM-FBG fluorescence calibration curve. **(b)** Adsorption of 20 μg/mL FAM-FBG determined by quenching of conjugated FAM fluorophore to 5 μg/mL polymer-SWNTs. **(c)** Adsorption of 40 μg/mL FAM-FBG determined by quenching of conjugated FAM fluorophore to 5 μg/mL polymer-SWNTs. **(d)** Adsorption of 60 μg/mL FAM-FBG determined by quenching of conjugated FAM fluorophore to 5 μg/mL polymer-SWNTs. The decrease in the FAM-FBG concentration over time across all concentrations can be attributed to self-quenching.

Lastly, biofouling considerations are often overlooked for polynucleotide delivery applications. Specifically, spontaneous protein adsorption to nanoparticle surfaces can alter the physicochemical properties of the polymer–nanoparticle complex, generating adverse outcomes for successful DNA or RNA loading and delivery. To understand the impact of different covalently linked polymers on protein adsorption to the SWNT surface, we performed

an assay to test the adsorption of fibrinogen, a protein known to be highly involved in the formation of SWNT nanoparticle coronas[220]. We have previously demonstrated that the fluorescence of FAM-labeled fibrinogen (FAM-FBG) is quenched when this species adsorbs to a SWNT surface[221]. Therefore, we can use this solution-phase and real-time ligand binding assay to quantify the amount of protein that adsorbs onto a nanoparticle surface. When compared to COOH-SWNT across a range of FAM-FBG concentrations, we consistently observe that only one of our polymer-SWNT constructs, the low-phi-BPEI, best mitigates against protein adsorption (Figures 3.16, 3.17). We hypothesize that this antibiofouling effect is due to a combination of both the polymer's hydrophobic modifications and large size, which together may prevent the protein from binding to the SWNT surface[26].

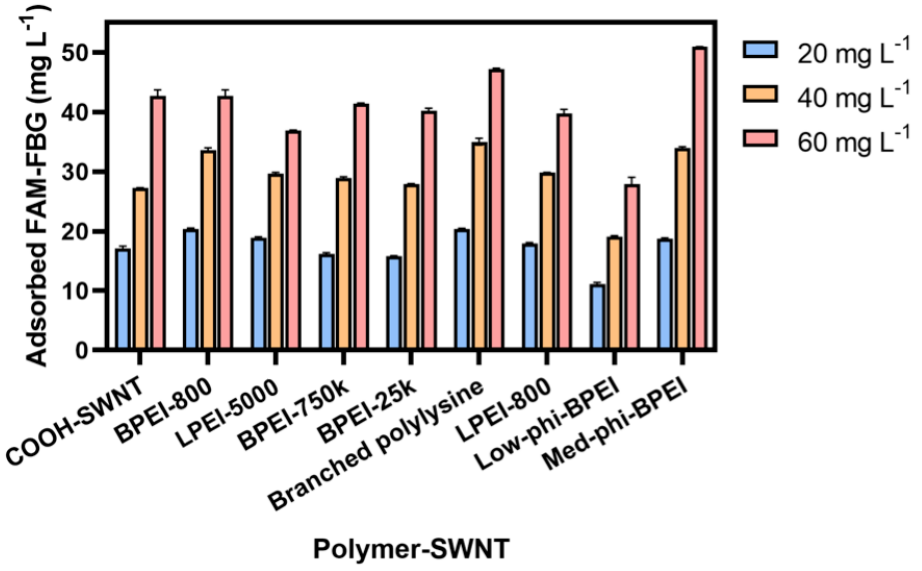

Figure 3.17: Quantification of adsorbed FAM-FBG on 5 μg mL^{-1} polymer-SWNT. Initial concentrations of FAM-FBG added to solution were 20, 40, and 60 μg mL^{-1} respectively. Error bars represent standard deviation of the mean (N = 3).

DNA Loading on Polymer-SWNT Constructs

We next investigated the ability of our polymer-SWNT nanomaterials to electrostatically bind and load plasmid DNA. Measurements taken before and after addition of DNA show a decrease in zeta potential after the addition of DNA, as expected due to the negative charge of DNA (Figure 3.18a). For the highest molecular weight linear polymer-SWNT construct (LPEI-5000-SWNT), we observe a negative final zeta potential for the DNA-polymer-SWNT

mixture. This decrease in zeta potential, which was also observed to a lesser extent for BPEI-800-SWNT and branched polylysine-SWNT following DNA addition, is also accompanied by an increase in size as measured by DLS, which is attributed to aggregation of these nanoparticles (Figure 3.18b).

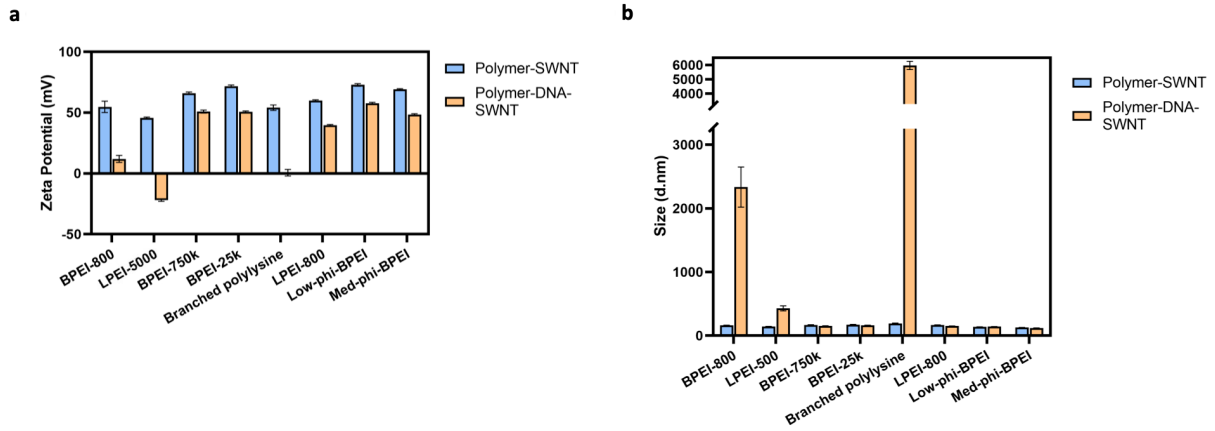

Figure 3.18: DNA loading capacity of polymer-SWNTs via zeta potential and DLS measurements. **(a)** Zeta potential measurements, in water, of polymer-SWNT constructs before and after addition of DNA. **(b)** DLS measurements, in water, of polymer-SWNT constructs before and after addition of DNA. Error bars represent standard deviation of the mean (N = 3).

The zeta potential values reported in Figure 3.18a are calculated from measurements of particle mobility under an applied electric field, representing averages of polymer-SWNT, polymer-SWNT-DNA, and free DNA that may be present in the sample. We attribute the significant decrease in zeta potential for samples that are less able to hold DNA to the abundance of free DNA in solution. The free DNA will have a significantly higher mobility than DNA bound to polymer-SWNTs, which then translates to a lower zeta potential value than their bound counterparts.

We hypothesize that the lower molecular weight of the BPEI-800 polymer results in less polymer mass available per conjugation site on the SWNT surface and, as a result, a decreased ability to bind DNA as effectively as larger polymers and a lower colloidal stability[202]. Similarly, a combination of steric hindrance and the lower density of amine groups in polylysine and LPEI-5000, especially as compared to BPEI, likely inhibits their ability to bind to the SWNT surface through EDC-NHS chemistry.

To better understand the relative loading ability of these various polymer-SWNT conjugates, we loaded DNA on polymer-SWNTs at a 1:1 mass ratio and next loaded DNA-polymer-SWNT samples in an agarose gel (Figure 3.19a). Due to the size and net charge

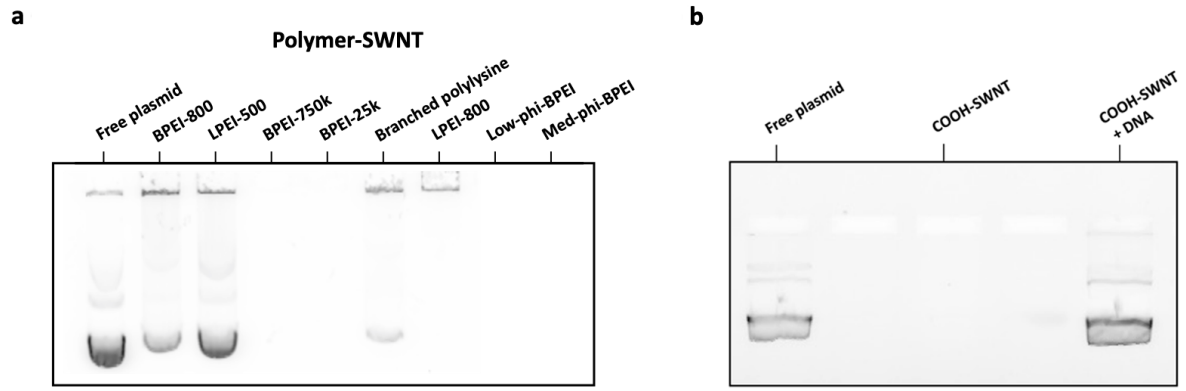

Figure 3.19: Agarose gel assay of DNA loading on polymer-SWNTs. (a) Agarose gel of polymer-SWNTs (10 μg mL^{-1}) loaded with DNA (10 μg mL^{-1}). **(b)** Agarose gel of COOH-SWNTs (10 μg mL^{-1}) loaded with DNA (10 μg mL$^{-1)}$.

of DNA successfully loaded on polymer-SWNTs, we anticipated that successfully bound DNA would exhibit retention in the loading well and would not run into the agarose gel during electrophoresis. For several polymer-SWNT constructs (BPEI-750k, BPEI-25k, low-phi-BPEI, and med-phi-BPEI), we do not observe any DNA running into the gel, suggesting these polymer-SWNT effectively load DNA at a 1:1 mass ratio. In contrast, we observed that the DNA loaded on polymer-SWNTs that previously showed a low or negative zeta potential, and colloidal instability, after DNA loading (BPEI-800, LPEI-5000, and branched polylysine) ran into the gel during electrophoresis, indicating the presence of free plasmid. These results confirm a large range of variability in the effectiveness of different polymer-SWNT constructs for loading polynucleotides such as plasmid DNA. As a control, when we perform the same assay using COOH-SWNT, we confirm that the DNA does not adsorb to COOH-SWNT (Figure 3.19b).

Plant Stress Response upon Infiltration with Polymer-SWNTs

As previously discussed, cationic polymers such as PEI are known to be toxic in mammalian cells, which severely limits their use in gene delivery[197,200,222]. However, polymer toxicity in plants is less well understood, particularly when used in conjunction with nanoparticle systems. Prior work has shown that leaf-infiltrated SWNTs per leaf area decrease by approximately 50% over 21 days, likely due to cell division and leaf expansion[141]; therefore the persistence of SWNT in plant leaves motivates testing of their biocompatibility in leaves. To test the biocompatibility of polymer-SWNTs in plants, we abaxially infiltrated 50 mg L^{-1} of polymer-SWNT nanoparticles into leaves of 5-week old mature *Nicotiana benthamiana (Nb)*

plants, a common model laboratory plant species (Figure 3.20)[223].

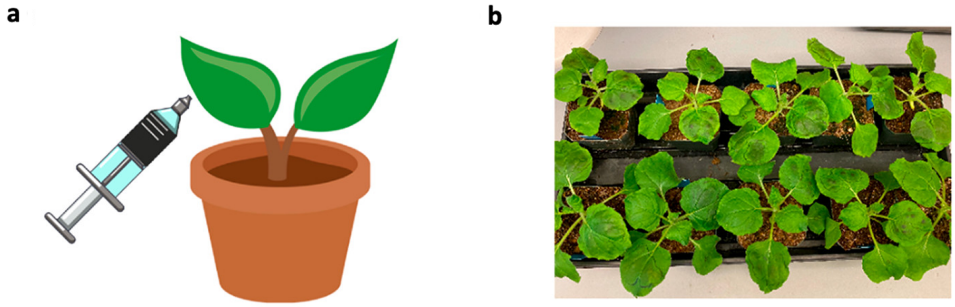

Figure 3.20: Infiltration of plant leaves with polymer-SWNTs. **(a)** Graphic illustration of leaf infiltration with polymer-SWNTs. **(b)** Plant leaves immediately after infiltration.

To assess toxicity, we infiltrated Nb leaves with polymer-SWNT nanoparticles and compared differential expression of stress genes in these leaves, relative to leaves infiltrated with COOH-SWNTs. By performing this comparison, we sought to isolate the toxic effect of each polymer-SWNT conjugate relative to the COOH-SWNT starting material. Two days after infiltration, we harvested leaf tissue and performed qPCR analysis of *pathogenesis-related gene 1 (PR1A)* upregulation, a known stress gene in *Nb* plants[224]. Quantification of *PR1A* expression shows that areas infiltrated with SWNT-branched PEI polymers exhibit large upregulation of *PR1A* 2 days after infiltration (Figure 3.21a). This stress response was observed most strongly in leaf tissues infiltrated with higher molecular weight polymer-SWNT conjugates. In contrast, low molecular weight and linear polymer-SWNT conjugates exhibited a relatively low stress response. Interestingly, a low degree of hydrophobic modification for branched PEI polymer-SWNT conjugates significantly reduced upregulation of *PR1A*, which also reduced nonspecific protein adsorption (Figure 3.17). We hypothesize that a combination of hydrophobic modifications and steric effects from large molecular weight PEI polymer limits the adsorption of proteins in plant media, which in turn mitigates toxicity of the nanoparticle–polymer conjugates. Similar trends have been shown in previous literature, whereby low enhancements in hydrophobicity increase transfection efficiency of PEI polymers[202].

These findings were further confirmed by testing the response of *arabinogalactan protein 41 (NbAGP41)*, for which the orthologous gene in *Arabidopsis thaliana (AT5G24105)* was previously shown to be downregulated during plant stress response[225]. We found that the low-phi-BPEI and branched polylysine both did not lead to downregulation of this gene, suggesting their biocompatibility in *Nb* plants (Figure 3.21b). We performed the same tests in *Arabidopsis thaliana* plants, where we observed no notable difference in stress response

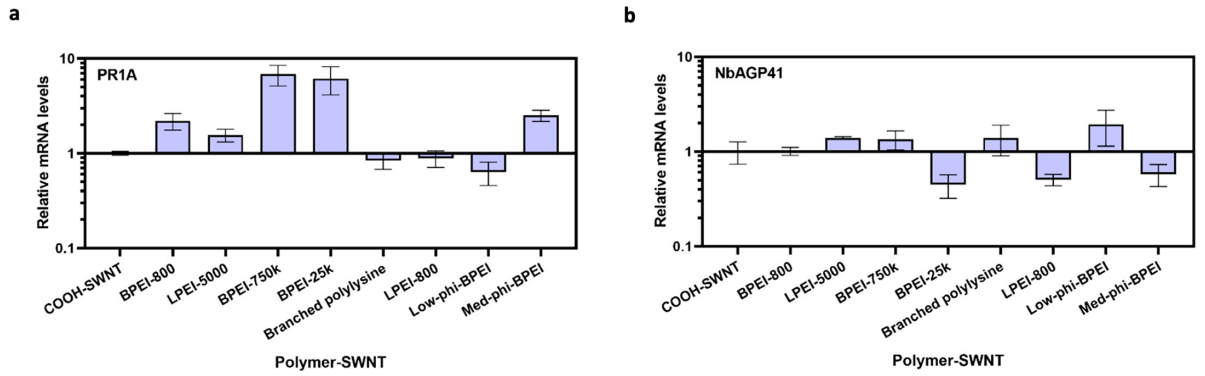

Figure 3.21: qPCR analysis of plant stress response to polymer-SWNTs. **(a)** qPCR analysis quantifying mRNA fold-change for *PR1A* gene two days after infiltration. **(b)** qPCR analysis quantifying mRNA fold change for *NbAGP41* gene two days after infiltration. Error bars represent standard deviation of the mean (N = 4).

trends between leaves infiltrated with BPEI-25k-SWNT and DNA-BPEI-25k-SWNT constructs (Figure 3.22).

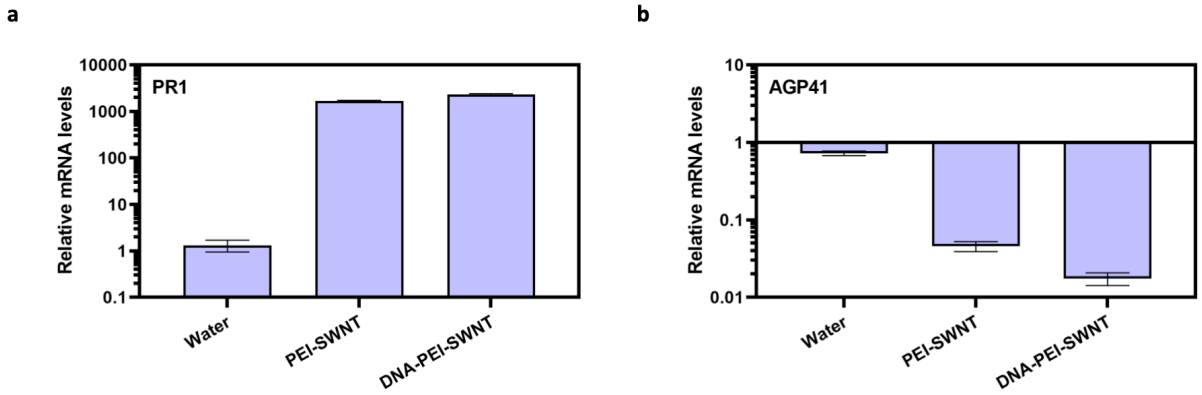

Figure 3.22: qPCR analysis of plant stress response. **(a)** qPCR analysis quantifying mRNA fold-change for *PR1* gene 2 days after infiltration. **(b)** qPCR analysis quantifying mRNA fold change for *AGP41* gene 2 days after infiltration. We observe no notable difference in trends of mRNA fold change of *AGP41* between *Arabidopsis thaliana* leaves infiltrated with BPEI-25k-SWNT and DNA-BPEI-25k-SWNT. Error bars represent standard error of the mean (N = 3).

Interestingly, we observe that the low-phi-BPEI-SWNT, which previously demonstrated the lowest levels of protein adsorption, also showed the highest level of biocompatibility as assessed *via* qPCR. This correlation suggests that protein adsorption to nanoparticles may play an important role in plant stress response, creating an opportunity for the tailoring of polymer properties to enhance or mitigate these effects.

3.4 Conclusion

Despite the widespread use of polymer–nanoparticle conjugates for the delivery of biomolecular cargo, there lacks consensus on what nanocarrier properties maximize their loading ability, polydispersibility, stability, and biocompatibility. To address these issues, we generated and characterized a library of polymer-SWNT nanoparticles for DNA loading. We found that commercially available carboxylated SWNTs contain a high degree of amorphous carbon, which is detrimental to downstream chemical modification and successful recovery of polymer-SWNT complexes. Therefore, we identified synthetic techniques, including SWNT carboxylation *via* acid reflux and subsequent washing with a basic solution, to aid in removal of amorphous carbon and improve functionalization density on the SWNT surface. Subsequently, we identify that the presence of free polymer, whether residual after covalent conjugation or as a product of hydrolysis from the nanoparticle surface over time, can also inhibit the electrostatic adsorption of polynucleotides to the nanoparticle. We demonstrate successful removal of free polymer and techniques to minimize hydrolysis through polymer selection and storage conditions. By testing different cationic polymers, we demonstrate their differing abilities to load DNA, largely as a function of the polymer size and structure. These material properties also play a role in biomolecule adsorption and plant toxicity, suggesting the need for improved polymer design that can address both of these challenges.

This study further highlights the wide tunability of polymer-SWNT chemistry that can allow for improved biomolecule loading and stability. Our results show successful covalent attachment of a variety of cationic polymers and provide insight into rational polymer design for improved conjugation and electrostatic adsorption of DNA. These findings offer further insight into chemistries and material design that can build upon the inherent advantages of nanomaterials such as SWNTs for cargo delivery in biological systems.

3.5 Methods

Materials

All chemicals unless otherwise noted were purchased from Sigma-Aldrich. Branched PEI polymers were purchased from Sigma-Aldrich; all other polymers were provided by BASF. Carboxylated SWNTs were purchased from Sigma-Aldrich. Raw high pressure carbon monoxide (HiPCO) synthesized SWNTs were purchased from NanoIntegris.

Synthesis of COOH-SWNTs

Synthesis of COOH-SWNTs was adapted from previous literature[213]. SWNT (20 mg) was combined in a round-bottom flask with 2.6 M HNO3 (40 mL). This was connected to a reflux condenser and stirred with a magnetic stirring bar at 120 °C for 12 h. After being cooled to room temperature, the product was isolated *via* vacuum filtration and washed sequentially with water, methanol, DMF, NaOH, and water. The solid was lyophilized for storage.

Synthesis of EDC-NHS Polymer SWNTs

Synthesis of EDC-NHS polymer SWNTs was adapted from previously published work[141,208]. COOH-SWNTs were added to water in a 1 mg:1 mL ratio and dispersed *via* bath (10 min) and probe-tip (30 min, ˜30–40 W) sonication. The resulting solution was centrifuged at 18,000g for 1 h. Afterward, the supernatant was collected, and the concentration was measured *via* absorbance at 632 nm with an extinction coefficient of 0.036.

COOH-SWNT (1 mg) was dispersed in 100 mM MES buffer and adjusted to a pH of 4.5–6. N-(3-Dimethylaminopropyl)-N'-ethylcarbodiimide hydrochloride (EDC) (5 mg) and N-hydroxysulfosuccinimide sodium salt (NHS) (5 mg) were dissolved in 100 mM MES solution (2.5 mL) and added dropwise to the SWNT mixture while stirring. The solution was bath sonicated for 15 min and then placed on an orbital shaker at 100 rpm for 45–60 min. The product was then washed three times with 0.1x PBS *via* spin filtration at 300g for ˜8 min through a 100K MWCO filter. Each polymer (20 mg) was dissolved in 0.1x PBS and adjusted to a pH between 7.4 and 7.6. The SWNT solution was added dropwise to the polymer solution while stirring. The pH was adjusted to a range of 7–8, and the solution was placed on an orbital shaker at 180 rpm overnight.

The resulting product was re-dispersed *via* probe-tip sonication (if significantly aggregated) and washed six times with water *via* spin filtration at 1000g through a 100K MWCO filter (1–20 min each, depending on the polymer). The product was resuspended *via* bath and probe-tip sonication, centrifuged, and the supernatant was collected. The SWNT concentration was measured *via* absorbance at 632 nm with an extinction coefficient of 0.036.

Synthesis of Triazine Polymer SWNTs

Synthesis of triazine polymer SWNTs with high labeling density (Trz-H) was adapted from previously published work[209]. Trz-H SWNTs (10 mg) were dispersed in dimethylformamide (DMF) (5 mL) and bath sonicated for 15 min. Next, polymer (13.3 mg) and a 1.5 M excess of triethylamine were added, and the mixture was stirred at 65 °C for 2 days. The product was washed *via* centrifugation and re-dispersion in DMF and water (4 mL, two times each). The product was then resuspended in water and washed with water *via* spin filtration through a 100K MWCO filter six times at 1000g. The product was resuspended in water and lyophilized for storage.

DNA Loading

Plasmid DNA was added to SWNTs at a 1:1 ratio and allowed to incubate at room temperature for 30 min. For plant infiltrations, solutions were diluted with MES delivery buffer to a final volume of 100 μL, with 500 ng each of DNA and SWNT, respectively[208].

DLS and Zeta Potential Measurements

DLS and zeta potential measurements were taken on a Zetasizer Nano ZS (Malvern Instruments). SWNT solutions (with and without DNA) were diluted in water to a concentration of 5 mg L^{-1}. Three replicates of at least 20 measurements were obtained for each sample after 2 min equilibration.

X-ray Photoelectron Spectroscopy (XPS)

Samples were drop cast onto the surface of a clean silicon wafer. XPS spectra were collected with a PHI 5600/ESCA system equipped with a monochromatic Al Kα radiation source (hν = 1486.6 eV). High-resolution XPS spectra were deconvoluted with MultiPak software (Physical Electronics) by centering the C–C peak to 284.8 eV, constraining peak centers to $\pm$0.2 eV peak positions reported in previous literature, constraining full width at half maxima of $\leq$1.5 eV, and applying Gaussian–Lorentzian curve fits with the Shirley background.

Thermogravimetric Analysis (TGA)

TGA measurements were conducted on a TGA 29950 thermogravimetric analyzer (TA Instruments). Samples were transferred to an alumina holder and placed in an inert nitrogen atmosphere. The temperature was increased from room temperature to 150 °C, held for 3 h, then gradually raised to 800 °C before being rapidly cooled. Measurements were taken every 2 s over the course of 17.5 h. Mass percentage loss was calculated as the difference between measurements at 308 min (150 °C) and 758 min (600 °C).

Fluorescence Tracking of Protein Adsorption

FAM fluorophore was conjugated to fibrinogen (FBG) using N-hydroxysuccinimide (NHS) ester chemistry according to previously published work[221]. SWNT and FAM-FBG were mixed in a 1:1 volume ratio, 50 μL total in a 96-well PCR plate (Bio-Rad), and placed in a CFX96 real-time PCR system (Bio-Rad). Final concentrations were 5 μg mL^{-1} SWCNT and 20, 40, or 60 μg mL^{-1} FAM-FBG. Scans were collected at the FAM fluorescence channel at 30 s intervals at 22.5 °C. A FAM-FBG fluorescence standard curve was used to convert fluorescence readings to unbound FAM-FBG concentrations.

Gel Analysis

For experiments to remove free polymer (Figure 3.7), filtrate (1 μL) was added to DNA (100 ng in 5 μL). Samples were loaded with 6x non-SDS containing loading dye and run in 0.8% agarose at 80 V for 45 min.

For experiments to test the DNA loading ability of our materials (Figure 3.19), polymer-SWNT (100 ng) was added to DNA (100 ng) and diluted to a total volume of 10 μL. Samples were loaded with 6x non-SDS containing loading dye and run in 0.8% agarose at 80 V for 45 min.

Plant Toxicity Measurements

Healthy (5 week old) *N. benthamiana* plants were selected for experiments. For each polymer, four replicates were performed on a single plant. 50 mg L^{-1} polymer-SWNT (100 μL) was injected into plant leaves *via* needle-less syringe infiltration (Figure 3.20a,b)[208]. After 2 days, the leaf tissue was collected. RNA was extracted *via* a TRIzol reagent and subsequently used for cDNA synthesis and qPCR measurements[217].

Table 3.1: Zeta potential of polymer-SWNTs.

Polymer	**Polymer-SWNT mobility [μm cm/(V s)]**	**Polymer-SWNT apparent zeta potential [mV]**
COOH-SWNT (no polymer)	-3.928 $\pm$ 0.039	-50.1 $\pm$ 0.529
Branched polyethylenimine (800)	4.289 $\pm$ 0.363	+54.7 $\pm$ 1.27
Linear polyethylenimine (5000)	3.571 $\pm$ 0.057	+45.6 $\pm$ 0.723
Branched polyethylenimine (750k)	5.169 $\pm$ 0.082	+65.9 $\pm$ 1.01
Branched polyethylenimine (25k)	5.614 $\pm$ 0.083	+71.6 $\pm$ 1.06
Branched polylysine	4.238 $\pm$ 0.178	+54.0 $\pm$ 2.27
Linear polyethylenimine (800)	4.696 $\pm$ 0.046	+59.9 $\pm$ 0.586
Low hydrophobic modified branched polyethylenimine	5.702 $\pm$ 0.082	+72.8 $\pm$ 1.07
Medium hydrophobic modified branched polyethylenimine	5.428 $\pm$ 0.035	+69.2 $\pm$ 0.451

Table 3.2: Peak deconvolution of XPS spectra of COOH-SWNT.

Peak	**Pristine**	**Commercial**	**Commercial, base-washed**	**In-house**	**In-house, base-washed**
sp^2 C	71.37	57.01	64.09	51.21	50.34
C-OH	10.80	23.16	14.52	23.99	22.60
C=O	7.61	9.17	8.07	11.91	10.33
O=C-OH	3.92	7.06	8.3	10.48	12.57
Sat.	6.30	3.61	5.02	2.40	4.16

Unit = % Area.

Table 3.3: Size of nanomaterial constructs, characterized by dynamic light scattering (DLS).

Functionalized nanomaterial	**Size (d.nm)**[3]
COOH-SWNT (Commercial)	147.9 ± 1.484
COOH-SWNT (in-house)	237.0 ± 4.868
PEI-SWNT	160.8 ± 3.037
PEI-SWNT-DNA	130.3 ± 1.670
Trz-H SWNT	300.3 ± 5.848
Trz-PEI SWNT	394.0 ± 3.051
Trz-PEI-SWNT-DNA	779.8 ± 25.934

Table 3.4: Elemental analysis of nanomaterial constructs and polymer components.

Material	**% C**	**% H**	**% N**
BPEI-25k	2.02	5.52	1
BPEI-25k-SWNT	2.23	5.81	1

After accounting for sample impurities, we observe that the majority of the signal we obtain can be attributed to BPEI-25k. Assuming a molecular formula of C_2H_5N and a molecular weight of 25,000 Mw, we can calculate a ratio of 166 SWNT carbon atoms per BPEI molecule. This corresponds to a polymer:SWNT mass ratio of 12.5:1. Using an estimated SWNT surface area of 1315 m^2 g^{-1}, this translates to a surface density of 9.5 mg m^{-2}.[217]

Chapter 4

Streptavidin-mediated conjugation of DNA to carbon nanotubes

4.1 Chapter abstract

There are many outstanding challenges that limit the efficacy of nanomaterials to deliver biomolecular cargo to biological systems. In particular, there are limited chemistries available for the attachment of this cargo to nanomaterials that also preserve key characteristics such as aqueous solubility and biocompatibility. Furthermore, the lack of specificity for the loading of biomolecular cargo, such as plasmids, inherent in many existing delivery systems can also impact overall system efficiency. Here, we explore the development of streptavidin-biotin based chemistry for the covalent conjugation of plasmid DNA to single-walled carbon nanotubes (SWNTs). These results demonstrate the successful conjugation and quantification of streptavidin to the SWNT surface, as well as loading of biotinylated DNA cargo, and offer insights into pathways for their use in delivery in biological systems.

4.2 Introduction

The delivery of plasmid DNA (pDNA) and other biomolecular cargo such as proteins by nanomaterials remains an area of significant research effort. Particularly, there is a need to identify new surface chemistries and synthetic pathways to probe and expand the upper limits of DNA and protein cargoes.

To date, many techniques developed for the delivery of DNA cargo *via* nanomaterials have centered on the use of noncovalent, electrostatic adsorption between a positively charged nanoparticle and negatively charged pDNA[141,143,226]. In the case where cationic polymers are used, this results in a non-specific conjugation between the nanoparticle and DNA cargo that can limit the effective release of cargo from the polymer complex[227]. Further, additional research has demonstrated that the formation of partially condensed DNA on the CNT surface is a prerequisite for transfection and expression[228]. The use of cationic polymers can

also present additional challenges for delivery, including toxicity to biological systems[217] and long-term stability in aqueous and biological environments[226].

To this end, site-specific techniques for the precise loading of plasmids onto carrier nanoparticles have emerged as an attractive area for scientific research in this space. In particular, the binding between streptavidin, a 66.0 kDa tetrameric protein purified from the bacterium *Streptomyces avidinii*, and biotin, a small molecule, is one of the strongest non-covalent interactions known in nature, with a dissociation constant (K_d) on the order of 10^{-14} mol/L. Because of the strength and stability of this interaction, resistant to organic solvents, denaturants, detergents, enzymes, and extreme temperatures and pH, streptavidin-biotin chemistry is used extensively in a variety of biochemical applications.

Previous research by Beals et al. has demonstrated the site-specific biotinylation of plasmid DNA and subsequent conjugation to gold nanoparticles *via* thiol chemistry for delivery[229,230]. These gold nanoparticles were further covalently conjugated to a derivatized hyaluronic acid stabilizing polymer and a CD44 targeting aptamer. Upon immersing MDA-MB-231 cells in media containing these nanocomplexes for 24 hours, they observed targeted cellular uptake and increased protein expression. Further work has demonstrated the use of similar systems to deliver doxorubicin, an anticancer drug, to target cells overexpressing CD44 receptors8.

In this work, we explore the development of streptavidin-biotin chemistry for the covalent conjugation of pDNA to single-walled carbon nanotubes (SWNT). This proof-of-principle suggests that these techniques could be a viable alternative to other existing nanoparticle-biomolecule delivery systems and offers exciting opportunities for future research

4.3 Results and Discussion

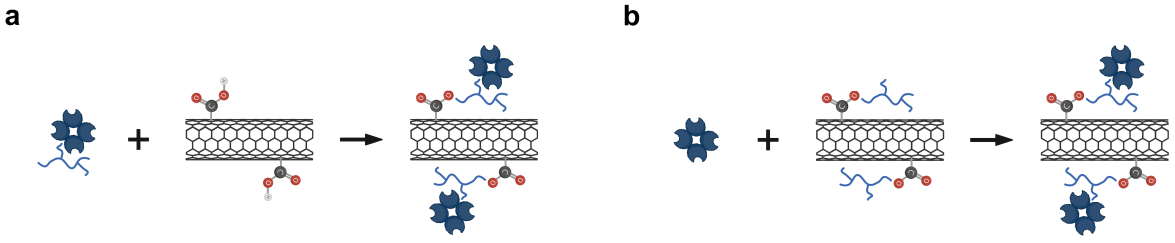

Figure 4.1: Synthesis of streptavidin-SWNT. (a) Streptavidin is functionalized with PEG and then conjugated to COOH-SWNT (Pathway 1). **(b)** COOH-SWNT is functionalized with PEG and then conjugated to streptavidin (Pathway 2).

We developed two pathways for the covalent conjugation of streptavidin to SWNT. First, we functionalized a 52 kDa streptavidin tetramer with a 5 kDa diamine-PEG group *via* EDC-NHS coupling. The functionalized protein was purified and then conjugated to carboxylated SWNT (COOH-SWNT) *via* EDC-NHS coupling (Pathway 1, hereafter abbreviated as SWNT+PEG-strep) (Figure 4.1a). In the second pathway, we used EDC-NHS chemistry to covalently functionalize COOH-SWNT with diamine-PEG, followed by subsequent purification and covalent conjugation to streptavidin *via* EDC-NHS chemistry (Pathway 2, hereafter abbreviated as PEG-SWNT+strep) (Figure 4.1b). The synthesis for each of these pathways is described in further detail below in the Methods section. Streptavidin was conjugated to COOH-SWNT in ratios ranging from 0.5:1 to 100:1 SWNT:streptavidin.

To confirm the removal of free streptavidin after washing, samples were run on a PAGE gel, where we would expect streptavidin not conjugated to the SWNT surface to run (Figure 4.2a). Across a wide range of SWNT:streptavidin ratios, we do not observe any free streptavidin present after washing. We then quantified the amount of protein retained on the SWNT surface using a Qubit fluorescence assay (Figure 4.2b). Because we have rigorously confirmed the removal of free streptavidin, this provides us with a high degree of confidence that the protein detected here is in fact securely attached to the SWNT surface.

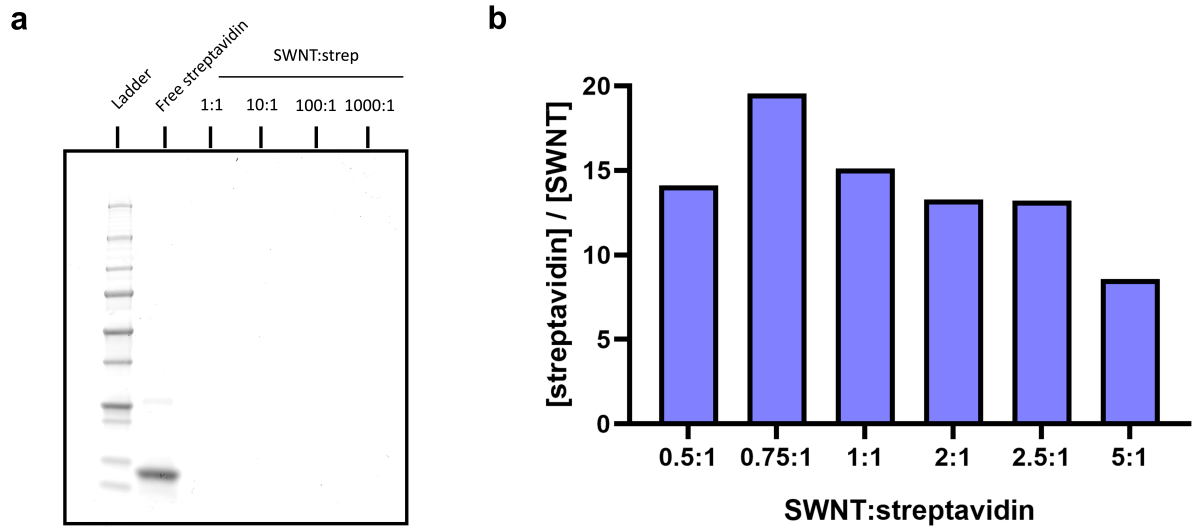

Figure 4.2: Confirmation of streptavidin on SWNT surface. **(a)** PAGE gel demonstrating lack of free streptavidin in streptavidin-SWNT solutions across all ratios of SWNT:streptavidin. **(b)** Qubit assay quantification of streptavidin present on the SWNT surface. Both datasets refer to constructs synthesized using the SWNT+PEG-strep method.

Notably, we only detect the presence of streptavidin using a Qubit assay for constructs

synthesized using low ratios of SWNT:streptavidin. Correspondingly, even at these low ratios, after normalizing the amount of streptavidin measured to the concentration of SWNT, we observe an overall slight decrease in the amount of streptavidin present as we move towards higher SWNT:streptavidin ratios.

Having confirmed the conjugation of streptavidin to the SWNT surface, we next tested their ability to bind to biotinylated DNA plasmid using agarose gel electrophoresis. To better understand the upper limit of biotinylated DNA binding by streptavidin, both in its native and PEG-functionalized form, we tested its retention with increasing ratios of DNA:streptavidin (Figure 4.3a). We observe the presence of a band corresponding to free plasmid emerging at ratios higher than 1:1 DNA:streptavidin, suggesting its retention at lower ratios. In contrast, we observe a distinct band when loading non-biotinylated DNA. From this, we can confirm that the retention of plasmid is in fact due to specific streptavidin-biotin interactions.

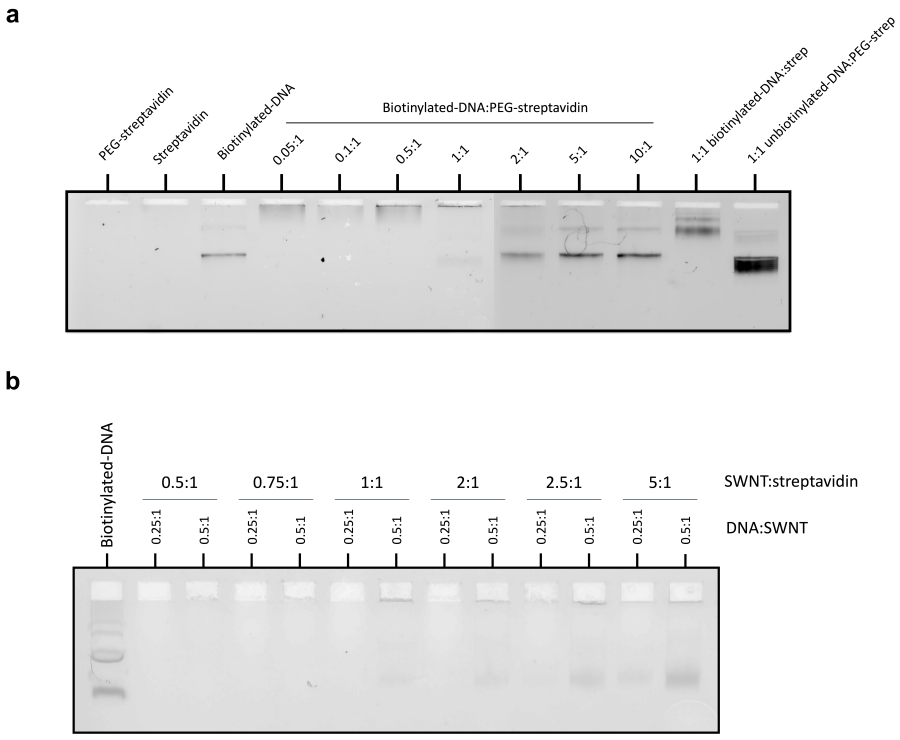

Figure 4.3: DNA loading on streptavidin-functionalized SWNTs. (a) Agarose gel demonstrating the ability of PEG-streptavidin to retain biotinylated-DNA. **(b)** Agarose gel demonstrating the loading of biotinylated-DNA on streptavidin-functionalized SWNTs at ratios of both 0.25:1 and 0.5:1 DNA:SWNT. Bands indicate the presence of non-conjugated plasmid.

When performing the same agarose gel assay with our streptavidin-SWNT constructs, we observe that streptavidin-SWNTs synthesized at lower ratios of SWNT:streptavidin are better able to bind biotinylated DNA (Figure 4.3b). This effect is particularly pronounced when attempting to load higher amounts of plasmid.

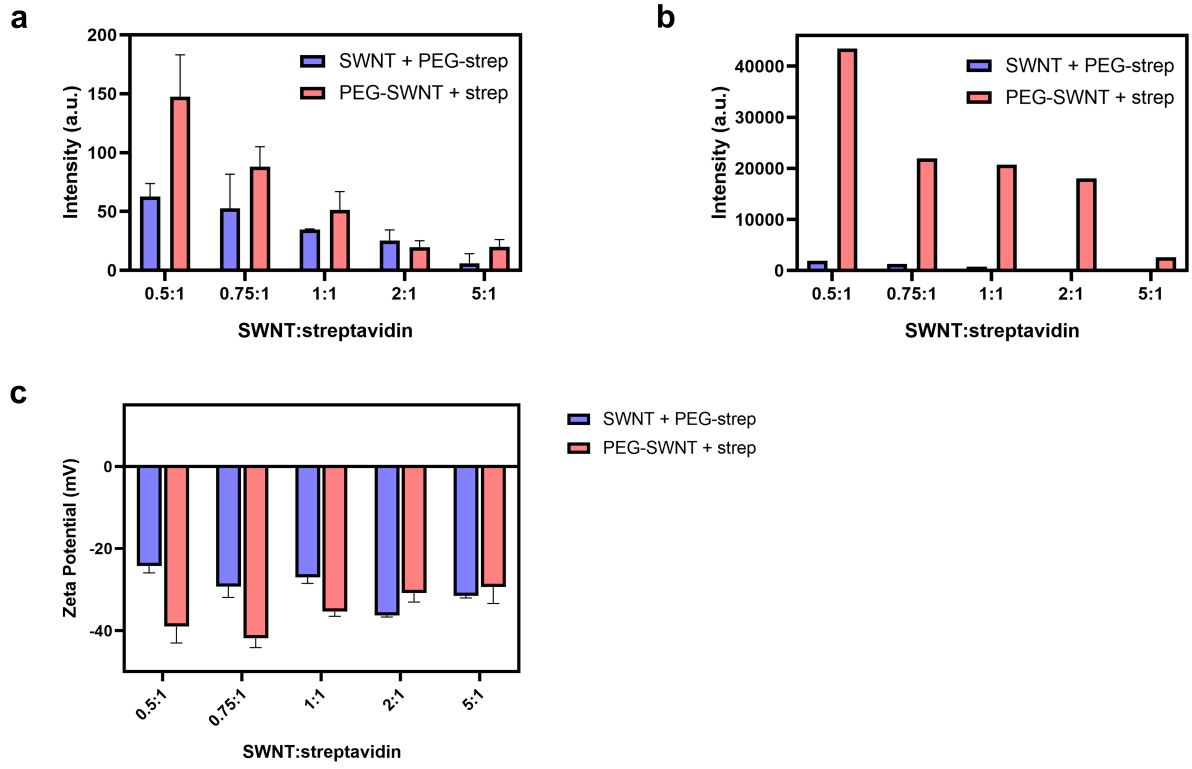

Figure 4.4: Assaying internalization of fluorescent streptavidin-SWNT in HEK cells. **(a)** Flow cytometry analysis quantifying fluorescence of fluorophore-labeled streptavidin-SWNT internalized in HEK cells (N=3). **(b)** *Ex vivo* assay of fluorophore-labeled streptavidin-SWNT on a plate reader. **(c)** Zeta potential measurements of fluorophore-labeled streptavidin-SWNTs. Error bars represent standard deviation of the mean (N=3).

To gauge the potential for these nanoparticles to successfully deliver their cargo to biological systems, we sought to demonstrate their internalization ability inside mammalian cells as a proof of concept. Using the synthesis process previously described, we covalently conjugated fluorophore-labeled streptavidin to SWNTs. These nanoparticles were then co-incubated with HEK cells, washed to remove non-internalized materials, and then assayed using flow cytometry. Our initial results suggest that these constructs are able to internalize

in these cells (Figure 4.4a). Across both synthetic routes, we observe an overall decrease in the amount of fluorescent signal at higher ratios of SWNT:streptavidin.

Based on our previous results, this can potentially be attributed to decreasing amounts of streptavidin to the SWNT surface, rather than differences in internalization efficiency. Further, we observe a greater signal for constructs synthesized using the PEG-SWNT+strep pathway, which may also be attributed to differences in synthesis efficiency. This is further confirmed by testing the fluorescence of these fluorophore-labeled streptavidin-SWNTs *ex vivo* on a plate reader (Figure 4.4b), where we observe substantially higher fluorescence for PEG-SWNT+strep constructs. We hypothesize that our observations may also be explained by the relative charge of our nanoparticles. Nanoparticles that exhibited higher internalization also had a (negative) zeta potential of greater magnitude, a phenomenon that is known to be key for nanoparticle internalization (Figure 4.4c)[205].

4.4 Conclusion

This study provides new insight into the development of a protein-mediated, covalent conjugation of pDNA to SWNTs, with the potential for improved biomolecule loading and stability. Our results demonstrate the successful conjugation and quantification of streptavidin to the SWNT surface, as well as loading of biotinylated DNA cargo. We also demonstrate that these constructs are able to internalize inside mammalian cells, though further efforts are needed to optimize and better understand their ability to deliver cargo. In particular, additional work to develop site-specific biotinylation of the plasmid cargo could lead to increased loading efficiency. With these improvements, this platform presents a number of exciting opportunities to explore the impact of new methods for DNA-loading on nanomaterials on internalization efficiency and mechanisms of DNA delivery inside cells.

4.5 Methods

Materials

All chemicals unless otherwise noted were purchased from Sigma-Aldrich. 4arm-PEG5K-NH2 (PEG) was purchased from Millipore Sigma. The 40k MWCO Zeba Spin Desalting Columns were purchased from Thermo Fisher. The Qubit Protein Assay Kits were purchased from Thermo Fisher.

Preparation of COOH-SWNTs

OOH-SWNTs were added to water in a 1 mg:1 mL ratio and dispersed *via* bath (10 min) and probe-tip (30 min, ˜30-40 W) sonication. The resulting solution was centrifuged at 18,000g for 1 h. Afterward, the supernatant was collected, and the concentration was measured *via* absorbance at 632 nm with an extinction coefficient of 0.036.

Streptavidin-SWNT synthesis: Pathway 1

4arm-PEG5K-NH2 (9.9 mg) was added to a solution of streptavidin dissolved in water (100 μg, 10 μL) at a 9:1 PEG:streptavidin molar ratio. N-(3-Dimethylaminopropyl)-N'-ethylcarbodiimide hydrochloride (EDC) (1 mg) and N-hydroxysulfosuccinimide sodium salt (NHS) (1 mg) were dissolved in nuclease free water (450 μL) and added to the PEG-streptavidin solution. This mixture was allowed to react on an orbital shaker at 150 rpm for 24 h at 4 °C. The mixture was then washed through a 40k MWCO Zeba Spin Desalting Column according to manufacturer guidelines.

EDC (1 mg) and NHS (1 mg) were dissolved in 100 μL of 100 mM MES buffer and added to an aliquot of suspended COOH-SWNT (30 μg). The mixture was allowed to react on an orbital shaker at 100 rpm for 45 min at room temperature. The product was then washed three times with 0.1x PBS *via* spin filtration at 300g for 4-8 min through a 100k MCWO filter. PEG-streptavidin was then added in the appropriate ratio and the mixture was placed on an orbital shaker at 150 rpm overnight at 4 °C. The mixture was then washed six times with water *via* spin filtration at 1000g for 3-5 min through a 100k MWCO filter. The SWNT concentration was measured *via* absorbance at 632 nm with an extinction coefficient of 0.036.

Streptavidin-SWNT synthesis: Pathway 2

EDC (5 mg) and NHS (5 mg) were dissolved in 1.25 mL of 100 mM MES buffer and added to an aliquot of suspended COOH-SWNT (1 mg). The mixture was allowed to react on an orbital shaker at 100 rpm for 30 min at room temperature. The product was then washed three times with 0.1x PBS *via* spin filtration at 300g for 8 min through a 100k MCWO filter. 20 mg PEG was dissolved in 1 mL water and added to the SWNT solution. The mixture was allowed to react on an orbital shaker at 100 rpm for 30 min at room temperature. The resulting PEG-SWNT mixture was then washed six times with water *via* spin filtration at 1000g for 3-5 min through a 100k MWCO filter. The SWNT concentration was measured *via* absorbance at 632 nm with an extinction coefficient of 0.036.

EDC (1 mg) and NHS (1 mg) were dissolved in 100 μL of 100 mM MES buffer and added to an aliquot of suspended PEG-SWNT (30 μg). The mixture was allowed to react on an orbital shaker at 100 rpm for 45 min at room temperature. The product was then washed three times with 0.1x PBS *via* spin filtration at 300g for 4-8 min through a 100k MCWO filter. Streptavidin was then added in the appropriate ratio and the mixture was placed on an orbital shaker at 150 rpm overnight at 4 °C. The mixture was then washed six times with water *via* spin filtration at 1000g for 3-5 min through a 100k MWCO filter. The SWNT concentration was measured *via* absorbance at 632 nm with an extinction coefficient of 0.036.

PAGE gel assay

To detect the presence of free streptavidin, 250 ng of streptavidin-SWNT was aliquoted and incubated at 95 °C for 5 minutes to denature the protein tetramers. Samples were then loaded into a PAGE gel and run at 120 V for 30 minutes. The gel was then stained with a Flamingo dye for imaging (Figure 4.2a).

Qubit protein assay

Concentrations of streptavidin both conjugated to SWNT and alone were measured using a Qubit protein assay. Samples were prepared according to manufacturer guidelines and a standard curve of streptavidin solutions with known concentrations ranging from 0.1 to 1.5 mg/L was used for calibration.

DNA conjugation assays

To assay conjugation of biotinylated-DNA to streptavidin (Figure 4.3a), 75 ng of DNA was added to PEG-streptavidin at varying ratios and allowed to incubate at room temperature for 30 min. Samples were loaded with 6X non-SDS containing loading dye and run in 1.2% agarose at 70 V for 2 h.

To assay conjugation of biotinylated-DNA to streptavidin-SWNT (Figure 4.3b), 30 ng of DNA was added to streptavidin-SWNT at varying ratios and allowed to incubate at room temperature for 30 min. Samples were loaded with 6X non-SDS containing loading dye and run in 1.2% agarose at 70 V for 2 h.

HEK cell internalization assay

HEK293T cells were plated in a 96-well plate to 10,000 cells/well and allowed to attach overnight. Fluorescently labeled streptavidin-SWNT (50 ng) was added to each well. Expression was checked 24 h post-infiltration using flow cytometry.

Zeta potential measurements

Zeta potential measurements were taken on a Zetasizer Nano ZS (Malvern Instruments). SWNT solutions were diluted in water to a concentration of 1 mg/L. Three replicates of at least 20 measurements were obtained for each sample after 2 min equilibration.

Chapter 5

Streamlining USDA regulation of gene editing to benefit US agriculture

5.1 Chapter abstract

Feeding a growing world population and adapting agricultural production to a changing climate is a significant challenge that can be mitigated through the use of new gene-editing technologies in crops. However, current regulatory processes are overly burdensome and confusing, limit scientific innovation, and unduly hinder the widespread production of genetically engineered crops. To address these shortcomings, we propose the consolidation of federal regulatory communication into the United States Department of Agriculture and a unified and detailed web platform for commercial approval applications.

5.2 Gene editing: an evolving technology that could feed the world

Agricultural production is increasingly strained by changing climate and population growth. With the global population expected to reach 9.8 billion by 2050, farmers will have to grow about 70% more food than current production[231]. Meeting this challenge will require scientific advances that bridge the gap between conventional techniques and new technologies in plant breeding.

Selective breeding has been used for thousands of years in the domestication of crops to artificially select desired traits in foods, including those which enable higher yield. The basis for these traits is the organism's genome, which comprises all of the genes encoded in its DNA. When the DNA sequence of a particular gene is altered, this can change the physical

Chapter 5 is reproduced from work previously published as Hartman, S.; Horner, W.; Jackson, C.T.; Kovak, E.; Velan, V. Streamlining USDA Regulation of Gene Editing to Benefit US Agriculture. Journal of Science Policy & Governance 2020, 17, 1. https://doi.org/10.38126/JSPG170108.

expression of that gene—the organism's phenotype. Recent breeding techniques have used chemicals to induce random DNA mutations; these mutations may modify a trait of interest, such as increased drought tolerance or disease resistance, but often have additional, unwanted effects which may require decades to remove through breeding. Although such human-guided changes in traits deliberately alter the genetics of crops, they are not considered to be genetically engineered (GE) in the United States (US). US law more narrowly defines genetic engineering as "techniques that use recombinant, synthesized, or amplified nucleic acids to modify or create a genome"[232].

In the past decade, efforts to select for desirable plant traits have drastically increased with new biotechnology to more quickly and precisely introduce changes at the genetic level[233]. New gene-editing techniques like CRISPR-Cas9 have revolutionized the field, allowing plant breeders to target genes governing traits of value with greater speed and precision. In 2016, a report from the National Academies of Sciences, Engineering, and Medicine found no evidence that foods from GE crops are less safe than foods from non-GE crops[181]. Despite this, the new and evolving nature of gene-editing technology has placed a disproportionate regulatory burden on GE crops.

Because some genetic engineering techniques allow for the introduction of genes from other species, regulators want to ensure that changes to an organism's genome will not produce deleterious effects on human or environmental health. While the likelihood of such a risk is low, these crops are subject to more regulation than chemically mutagenized crops. The USDA justifies this differential regulation based on breeding technique because "plants created through conventional breeding have a history of safe use related to plant pest risk"[232].

With assurances for human and environmental health, the US is poised to realize significant economic benefits from improved GE crop variety and yield in the agricultural sector[234]. The country grows the largest acreage of GE crops in the world (40% of the global total), and is a net exporter of agricultural products, particularly to developing countries[234]. Additionally, due to its market share, the US also houses much of the world's GE crop research.

Despite the enormous potential benefits, the development of GE crops in the US has not been able to reach its full potential[235], largely due to the onerous and speculative commercialization process[236]. The entire process of developing a single GE crop in the US is very costly, averaging $130 million for 6 years of research and development and 7 years for regulatory review and commercialization[237]. Furthermore, uncertainty regarding time delays in the complicated regulatory process causes financial burden on companies that consequently limits their investment decisions[237]. For example, the delay in approval by a single year is estimated to cost a biotechnology firm $22.7 million[237].

High barriers to market entry have excluded small and nascent businesses while also limiting commercial attention to only the largest of market opportunities, neglecting crops with lower market share which could benefit greatly from innovation[238,239]. Due to the high up-front costs and uncertain time horizon for returns on investment, GE research has thus far focused on staple crops like corn and wheat. However, the US exports a much larger variety of crops—in California alone, the grape, almond, and pistachio markets are significant contributors to the state's multibillion-dollar agriculture economy[233].

Issues around the regulation of GE plants have been highlighted by the proliferation of new, cheaper geneediting techniques that can be applied to these crops and by the rapid expansion of capable developers. Historically, the creation of GE crops has been largely performed by research universities and industrial agriculture companies[240]. With new geneediting techniques, however, these tasks are now increasingly undertaken by small- to medium-sized innovators such as start-ups and university research spin-offs targeting specialty crops[240]. At this time, regulatory processes have not sufficiently adapted to meet the needs of these new stakeholders.

5.3 Existing United States federal regulatory framework

GE plant regulatory policy is primarily created and implemented by three federal agencies: the Environmental Protection Agency (EPA), the Food and Drug Administration (FDA), and the United States Department of Agriculture (USDA). Their responsibilities regarding GE crops are outlined by the 2017 Update to the Coordinated Framework for the Regulation of Biotechnology[241] and the 2019 Executive Order on Modernizing the Regulatory Framework for Agricultural Biotechnology Products (EO13874)[242]. Broadly, the regulatory responsibilities of each agency for GE crops depends on the crop's specific use and method of production: the EPA is responsible for pesticide regulation; the FDA manages food safety, including food produced using biotechnology; and the USDA oversees products of biotechnology that may pose a risk to agricultural plant health[243].

Here, we focus on the USDA, as it is the agency given the most responsibility by, and has the most up-todate regulatory framework in response to, EO13874. Within the USDA, the Animal and Plant Health Inspection Service (APHIS) is the primary office responsible for regulating GE crops and other biotechnology products that may pose a risk to agricultural plant and animal health[243].

APHIS proposed an updated regulatory policy in June 2019 entitled "Movement of Certain Genetically Engineered Organisms," also referred to as the SECURE rule[244]. The subsequent final rule published in May 2020 aims to reduce "regulatory burden for developers of organisms that are unlikely to pose plant pest risks"[232]. To support this process, APHIS has created a publicly-accessible database containing the results of all completed regulatory status reviews, including each reviewed combination of plant, trait, and mechanism of action (MOA; the way a trait is expressed).

One key element of the new SECURE rule is allowing developers to self-determine exemption for their GE plant (Figure 5.1). GE plants are exempted if their genetic modification meets any of the following criteria: (1) it is solely a single base pair substitution or deletion, or (2) it introduces nucleic acid sequences from within or corresponding to sequences within the plant's natural gene pool. GE plants with a plant-trait-MOA combination that are the same as those of modified plants that APHIS has already approved can also be self-exempted,

with an option to request written confirmation from APHIS[232].

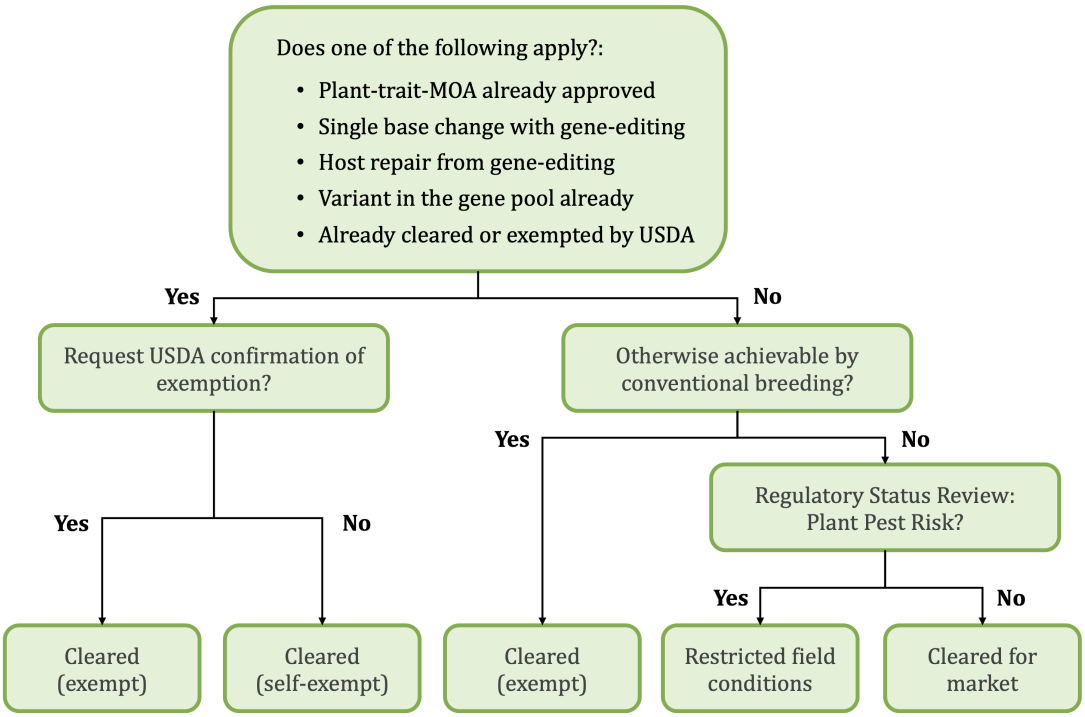

Figure 5.1: Regulatory pathway described in the 2020 APHIS SECURE rule. Figure adapted from Kuzma, 2020[245].

To ensure that developers can more easily navigate the regulatory process, EO13874 dictates that the USDA, EPA, and FDA must work together to establish a web-based platform providing links to different agency regulatory information[242]. This was meant to allow developers to submit inquiries and receive guidance through a centralized platform.

While these recent federal actions have sought to clarify and modernize regulation, significant barriers to scaling up the production of GE products still exist. Together, the 2017 Coordinated Framework Update, EO13874, and the SECURE rule outline the need for a unified and straightforward process for the approval of new biotechnologies, but the specific details of such a process are weakly defined at present. Given the rapidly changing landscape of agricultural genetic engineering and the entrance of small stakeholders targeting specialty crops, new policies must be implemented that are nimble enough to evolve alongside scientific advancements while balancing the needs of developers and public safety.

5.4 Policy recommendations

Two concrete measures can be taken by the USDA to address the aforementioned shortcomings and provide a clear path to safely and efficiently bring GE crops to market.

Facilitate application submissions through a web-based platform

The federal government, led by the USDA, should implement a clarifying web-based platform that facilitates product approval applications. EO13874's recommended Unified Biotechnology Web-Based Platform provides the foundation for improvement but does not go far enough. The platform should contain more than just descriptions for the regulatory roles of the USDA, FDA, and EPA as it does now[243]. The web platform currently states that "[each] regulatory agency has its own specific application procedures" but does little more than offer links to each website[243]. While the site also allows users to contact the agencies with questions regarding regulation, a far better use of the platform would be an avenue to submit an application for commercial approval of a biotechnology product. If the goal of the current regulatory modernization is to streamline and clarify the process of GE plant approval, then the unified web platform should serve as a tool to help small- and medium-sized producers begin the process of product approval.

Consolidate communication through a central office

The USDA should create an office to consolidate communication with crop developers regarding the GE plant approval process and manage a clearinghouse for inquiries. The SECURE rule, while it is an improvement, fails to simplify the regulatory process in a way that makes it accessible to small- to medium-sized innovators who have no previous experience with regulation but otherwise have the technical expertise and capacity to safely contribute to agricultural innovation. Federal agencies should coordinate their response to inquiries in addition to improvement of the aforementioned unified web platform. Since the USDA is currently the designated funder of the consolidated web-based platform (by EO13874), we propose that an office be created within the USDA to: manage communication between the three agencies, developers, farmers, and other stakeholders; determine which agency is most appropriate to regulate each product; and maintain the consolidated online platform. The US Congress has the power to establish this office and appropriate funding to it, in accordance with its existing authority[246].

5.5 Potential limitations of recommended policies

If the aforementioned proposals are implemented, the USDA will absorb new roles for the overall efficiency of the regulatory process. However, based on changes made in the recent SECURE rule, we expect the agency will also have a greatly decreased regulatory burden

since many new GE crops will be exempt from USDA regulation. Still, the USDA may not have sufficient capacity to handle all new requests. As a result, these proposals must be accompanied by an increase in Congressional appropriations, especially for the new clearinghouse office.

Furthermore, the proposed USDA clearinghouse office will not remedy all coordination issues. The more ambitious alternative to address these challenges would be the creation of a new agency, separate from the USDA, FDA, and EPA, to handle GE crop regulation. This would allow consolidation of communication, reporting, regulation, and policy changes into one agency. However, we do not recommend this for several reasons. First, the three existing agencies focus on different aspects of GE crops and this separation is valuable, allowing agencies to specialize within their areas of expertise. Second, the creation of another agency would be expensive and dramatically expand bureaucracy relative to the creation of a single office within the USDA. Third, the political effort required to create a new agency would be substantially greater than the creation of a new office within an existing Department. While imperfect, the proposed USDA office represents an acceptable and pragmatic approach to feasibly improve coordination.

5.6 Conclusion

We recommend a unified and detailed web platform for commercial approval applications and the consolidation of federal regulatory communication pertaining to genetic engineering technology to the USDA. If implemented, these steps will reduce regulatory burdens on companies and researchers seeking to bring new products to market without changing any safety or consumer protection standards. These proposals will also accommodate smaller firms and researchers who do not have dedicated legal staff or experience with handling federal regulations. These stakeholders will face lower financial and time constraints, which currently present major barriers of entry to the field[238,239,247].

With a clearer and more streamlined process, the US could see a proliferation of GE crops. By simplifying the GE regulatory requirements, the process of taking a GE crop to market will be more transparent and navigable for small- to medium-sized companies. Streamlining the information, submission, and communication processes should decrease the time required by developers to bring a GE crop to market, thereby making the process cheaper and more accessible to small stakeholders, including innovators who may find niche markets in editing specialty crops that lag in breeding efficiency.

The US agricultural sector also awaits innovations that will increase adaptation to the worsening threats of climate change, such as fire, drought, and flooding. If federal policy keeps pace with these advancements by streamlining and demystifying regulations, the US will benefit from crops that are more diverse, cheaper, and more resilient.

Chapter 6

Concluding remarks

Understanding the ways in which nanomaterials interact with biological molecules and systems, and developing chemical functionalizations to aid in that process, is essential to the development of new bioengineering tools and applications.

In this work, we have focused on the use of nanomaterials, particularly single walled carbon nanotubes (SWNTs), as a tool for CRISPR genome editing in plants. Particulary, we present mechanisms to optimize DNA loading on SWNTs *via* electrostatic interactions with covalently conjugated cationic polymers. While similar constructs are widely used in the research community, we present a unique assessment of the impact synthetic conditions and polymer selection can play on properties including DNA loading ability, polydispersity, and both chemical and colloidal stability. Turning to the practical application of these nanomaterials in plant systems, an area of significant research interest, we demonstrate that polymer hydrolysis from the SWNT surface is dependent on polymer selection, attachment chemistry, and storage conditions. We further explore the role that polymer selection plays in plant stress response upon introduction of these nanomaterials into leaf tissue and provide suggestions for polymer design to mitigate these impacts.

These findings are then applied towards a new system of streptavidin-functionalized SWNTs that enable the covalent attachment of DNA cargo *via* streptavidin-biotin chemistry. We demonstrate the successful conjugation and quantification of streptavidin to the SWNT surface, as well as loading of biotinylated DNA cargo. We also show that these constructs are able to internalize inside mammalian cells, providing a platform to better understanding the ways in which different DNA-loading strategies on nanomaterials can impact internalization efficiency and delivery mechanisms inside cells.

It is important to recognize that this scientific research does not occur in a vacuum and is motivated by the drastic needs to improve our global agricultural system. We end this thesis by exploring the federal regulatory challenges in the United States that limit scientific innovation and widespread production of genetically engineered crops, and make policy recommendations to safely streamline this process. By combining this scientific research with meaningful, hypothesis-driven and evidence-based policy, we can hope to address some of the most significant challenges of our time.

References

(1) Smith, A. M.; Mancini, M. C.; Nie, S. *Nature nanotechnology* **2009**, *4*, 710–711.

(2) Hong, G.; Antaris, A. L.; Dai, H. *Nature biomedical engineering* **2017**, *1*, 1–22.

(3) Zampetti, A.; Minotto, A.; Cacialli, F. *Advanced Functional Materials* **2019**, *29*, 1807623.

(4) Gong, Y.-J.; Zhang, X.-B.; Mao, G.-J.; Su, L.; Meng, H.-M.; Tan, W.; Feng, S.; Zhang, G. *Chemical science* **2016**, *7*, 2275–2285.

(5) Qian, G.; Gao, J. P.; Wang, Z. Y. *Chemical communications* **2012**, *48*, 6426–6428.

(6) Carr, J. A.; Franke, D.; Caram, J. R.; Perkinson, C. F.; Saif, M.; Askoxylakis, V.; Datta, M.; Fukumura, D.; Jain, R. K.; Bawendi, M. G., et al. *Proceedings of the National Academy of Sciences* **2018**, *115*, 4465–4470.

(7) Escobedo, J. O.; Rusin, O.; Lim, S.; Strongin, R. M. *Current opinion in chemical biology* **2010**, *14*, 64–70.

(8) Cosco, E. D.; Caram, J. R.; Bruns, O. T.; Franke, D.; Day, R. A.; Farr, E. P.; Bawendi, M. G.; Sletten, E. M. *Angewandte Chemie International Edition* **2017**, *56*, 13126–13129.

(9) Cosco, E. D.; Spearman, A. L.; Ramakrishnan, S.; Lingg, J. G.; Saccomano, M.; Pengshung, M.; Arús, B. A.; Wong, K. C.; Glasl, S.; Ntziachristos, V., et al. *Nature chemistry* **2020**, *12*, 1123–1130.

(10) Ding, B.; Xiao, Y.; Zhou, H.; Zhang, X.; Qu, C.; Xu, F.; Deng, Z.; Cheng, Z.; Hong, X. *Journal of Medicinal Chemistry* **2018**, *62*, 2049–2059.

(11) Li, B.; Lu, L.; Zhao, M.; Lei, Z.; Zhang, F. *Angewandte Chemie* **2018**, *130*, 7605–7609.

(12) Lei, Z.; Sun, C.; Pei, P.; Wang, S.; Li, D.; Zhang, X.; Zhang, F. *Angewandte Chemie* **2019**, *131*, 8250–8255.

(13) Wang, S.; Fan, Y.; Li, D.; Sun, C.; Lei, Z.; Lu, L.; Wang, T.; Zhang, F. *Nature communications* **2019**, *10*, 1–11.

(14) Antaris, A. L.; Chen, H.; Cheng, K.; Sun, Y.; Hong, G.; Qu, C.; Diao, S.; Deng, Z.; Hu, X.; Zhang, B., et al. *Nature materials* **2016**, *15*, 235–242.

(15) Yang, Q.; Ma, Z.; Wang, H.; Zhou, B.; Zhu, S.; Zhong, Y.; Wang, J.; Wan, H.; Antaris, A.; Ma, R., et al. *Advanced Materials* **2017**, *29*, 1605497.

(16) Yang, Q.; Hu, Z.; Zhu, S.; Ma, R.; Ma, H.; Ma, Z.; Wan, H.; Zhu, T.; Jiang, Z.; Liu, W., et al. *Journal of the American Chemical Society* **2018**, *140*, 1715–1724.

(17) Zhu, S.; Yang, Q.; Antaris, A. L.; Yue, J.; Ma, Z.; Wang, H.; Huang, W.; Wan, H.; Wang, J.; Diao, S., et al. *Proceedings of the National Academy of Sciences* **2017**, *114*, 962–967.

(18) Bai, L.; Sun, P.; Liu, Y.; Zhang, H.; Hu, W.; Zhang, W.; Liu, Z.; Fan, Q.; Li, L.; Huang, W. *Chemical Communications* **2019**, *55*, 10920–10923.

(19) Godard, A.; Kalot, G.; Pliquett, J.; Busser, B.; Le Guével, X.; Wegner, K. D.; Resch-Genger, U.; Rousselin, Y.; Coll, J.-L.; Denat, F., et al. *Bioconjugate Chemistry* **2020**, *31*, 1088–1092.

(20) Lei, Z.; Li, X.; Luo, X.; He, H.; Zheng, J.; Qian, X.; Yang, Y. *Angewandte Chemie International Edition* **2017**, *56*, 2979–2983.

(21) Algar, W. R. *Chemistry of Materials* **2020**, *32*, 4863–4883.

(22) Welsher, K.; Liu, Z.; Sherlock, S. P.; Robinson, J. T.; Chen, Z.; Daranciang, D.; Dai, H. *Nature nanotechnology* **2009**, *4*, 773–780.

(23) Pan, J.; Li, F.; Choi, J. H. *Journal of Materials Chemistry B* **2017**, *5*, 6511–6522.

(24) Bachilo, S. M.; Strano, M. S.; Kittrell, C.; Hauge, R. H.; Smalley, R. E.; Weisman, R. B. *science* **2002**, *298*, 2361–2366.

(25) Yamashita, S. *Apl Photonics* **2019**, *4*, 034301.

(26) Pinals, R. L.; Chio, L.; Ledesma, F.; Landry, M. P. *Analyst* **2020**, *145*, 5090–5112.

(27) Antaris, A. L.; Robinson, J. T.; Yaghi, O. K.; Hong, G.; Diao, S.; Luong, R.; Dai, H. *ACS nano* **2013**, *7*, 3644–3652.

(28) Danné, N.; Godin, A. G.; Gao, Z.; Varela, J. A.; Groc, L.; Lounis, B.; Cognet, L. *ACS photonics* **2018**, *5*, 359–364.

(29) Roxbury, D.; Jena, P. V.; Williams, R. M.; Enyedi, B.; Niethammer, P.; Marcet, S.; Verhaegen, M.; Blais-Ouellette, S.; Heller, D. A. *Scientific reports* **2015**, *5*, 1–6.

(30) Nißler, R.; Mann, F. A.; Preiß, H.; Selvaggio, G.; Herrmann, N.; Kruss, S. *Nanoscale* **2019**, *11*, 11159–11166.

(31) Bisker, G.; Dong, J.; Park, H. D.; Iverson, N. M.; Ahn, J.; Nelson, J. T.; Landry, M. P.; Kruss, S.; Strano, M. S. *Nature communications* **2016**, *7*, 1–14.

(32) Heller, D. A.; Jeng, E. S.; Yeung, T.-K.; Martinez, B. M.; Moll, A. E.; Gastala, J. B.; Strano, M. S. *Science* **2006**, *311*, 508–511.

(33) Salem, D. P.; Landry, M. P.; Bisker, G.; Ahn, J.; Kruss, S.; Strano, M. S. *Carbon* **2016**, *97*, 147–153.

(34) Jena, P. V.; Safaee, M. M.; Heller, D. A.; Roxbury, D. *ACS applied materials & interfaces* **2017**, *9*, 21397–21405.

(35) Bonis-O'Donnell, J. T. D.; Page, R. H.; Beyene, A. G.; Tindall, E. G.; McFarlane, I. R.; Landry, M. P. *Advanced Functional Materials* **2017**, *27*, 1702112.

(36) Brozena, A. H.; Kim, M.; Powell, L. R.; Wang, Y. *Nature Reviews Chemistry* **2019**, *3*, 375–392.

(37) Piao, Y.; Meany, B.; Powell, L. R.; Valley, N.; Kwon, H.; Schatz, G. C.; Wang, Y. *Nature chemistry* **2013**, *5*, 840–845.

(38) Kwon, H.; Furmanchuk, A.; Kim, M.; Meany, B.; Guo, Y.; Schatz, G. C.; Wang, Y. *Journal of the American Chemical Society* **2016**, *138*, 6878–6885.

(39) Kwon, H.; Kim, M.; Meany, B.; Piao, Y.; Powell, L. R.; Wang, Y. *The Journal of Physical Chemistry C* **2015**, *119*, 3733–3739.

(40) Berger, F. J.; Lüttgens, J.; Nowack, T.; Kutsch, T.; Lindenthal, S.; Kistner, L.; Müller, C. C.; Bongartz, L. M.; Lumsargis, V. A.; Zakharko, Y., et al. *ACS nano* **2019**, *13*, 9259–9269.

(41) Mann, F. A.; Herrmann, N.; Opazo, F.; Kruss, S. *Angewandte Chemie International Edition* **2020**, *59*, 17732–17738.

(42) Shi, J.; Chu, H.; Li, Y.; Zhang, X.; Pan, H.; Li, D. *Nanoscale* **2019**, *11*, 7287–7292.

(43) Xu, S.; Wang, F.; Zhu, C.; Meng, Y.; Liu, Y.; Liu, W.; Tang, J.; Liu, K.; Hu, G.; Howe, R. C., et al. *Nanoscale* **2016**, *8*, 9304–9309.

(44) Xu, S.; Cui, J.; Wang, L. *TrAC Trends in Analytical Chemistry* **2016**, *80*, 149–155.

(45) Li, C.; Chen, K.; Guan, M.; Wang, X.; Zhou, X.; Zhai, F.; Dai, J.; Li, Z.; Sun, Z.; Meng, S., et al. *Nature communications* **2019**, *10*, 1–9.

(46) Li, M.; Chen, T.; Gooding, J. J.; Liu, J. *ACS sensors* **2019**, *4*, 1732–1748.

(47) Tang, L.; Ji, R.; Li, X.; Bai, G.; Liu, C. P.; Hao, J.; Lin, J.; Jiang, H.; Teng, K. S.; Yang, Z., et al. *ACS nano* **2014**, *8*, 6312–6320.

(48) Li, Y.; Bai, G.; Zeng, S.; Hao, J. *ACS applied materials & interfaces* **2019**, *11*, 4737–4744.

(49) Weidman, M. C.; Beck, M. E.; Hoffman, R. S.; Prins, F.; Tisdale, W. A. *ACS nano* **2014**, *8*, 6363–6371.

(50) Moreels, I.; Justo, Y.; De Geyter, B.; Haustraete, K.; Martins, J. C.; Hens, Z. *ACS nano* **2011**, *5*, 2004–2012.

(51) Jeong, S.; Song, J.; Lee, W.; Ryu, Y. M.; Jung, Y.; Kim, S.-Y.; Kim, K.; Hong, S. C.; Myung, S. J.; Kim, S. *Nano Letters* **2017**, *17*, 1378–1386.

(52) Park, Y.; Jeong, S.; Kim, S. *Journal of Photochemistry and Photobiology C: Photochemistry Reviews* **2017**, *30*, 51–70.

(53) Santos, H. D.; Zabala Gutiérrez, I.; Shen, Y.; Lifante, J.; Ximendes, E.; Laurenti, M.; Méndez-González, D.; Melle, S.; Calderón, O. G.; López Cabarcos, E., et al. *Nature communications* **2020**, *11*, 1–12.

(54) Bruns, O. T.; Bischof, T. S.; Harris, D. K.; Franke, D.; Shi, Y.; Riedemann, L.; Bartelt, A.; Jaworski, F. B.; Carr, J. A.; Rowlands, C. J., et al. *Nature biomedical engineering* **2017**, *1*, 1–11.

(55) Zhang, M.; Yue, J.; Cui, R.; Ma, Z.; Wan, H.; Wang, F.; Zhu, S.; Zhou, Y.; Kuang, Y.; Zhong, Y., et al. *Proceedings of the National Academy of Sciences* **2018**, *115*, 6590–6595.

(56) Efros, A. L.; Nesbitt, D. J. *Nature Nanotechnology* **2016**, *11*, 661–671.

(57) Yuan, G.; Gomez, D. E.; Kirkwood, N.; Boldt, K.; Mulvaney, P. *ACS nano* **2018**, *12*, 3397–3405.

(58) Javaux, C.; Mahler, B.; Dubertret, B.; Shabaev, A.; Rodina, A.; Efros, A. L.; Yakovlev, D.; Liu, F.; Bayer, M.; Camps, G., et al. *Nature nanotechnology* **2013**, *8*, 206–212.

(59) Franke, D.; Harris, D. K.; Chen, O.; Bruns, O. T.; Carr, J. A.; Wilson, M. W.; Bawendi, M. G. *Nature communications* **2016**, *7*, 1–9.

(60) Zamberlan, F.; Turyanska, L.; Patane, A.; Liu, Z.; Williams, H.; Fay, M.; Clarke, P.; Imamura, Y.; Jin, T.; Bradshaw, T., et al. *Journal of Materials Chemistry B* **2018**, *6*, 550–555.

(61) Nadort, A.; Zhao, J.; Goldys, E. M. *Nanoscale* **2016**, *8*, 13099–13130.

(62) Kushida, T.; Marcos, H.; Geusic, J. *Physical Review* **1968**, *167*, 289.

(63) Fan, Y.; Zhang, F. *Advanced Optical Materials* **2019**, *7*, 1801417.

(64) Lei, X.; Li, R.; Tu, D.; Shang, X.; Liu, Y.; You, W.; Sun, C.; Zhang, F.; Chen, X. *Chemical science* **2018**, *9*, 4682–4688.

(65) Bünzli, J.-C. G. *Chemical reviews* **2010**, *110*, 2729–2755.

(66) Xie, X.; Li, Z.; Zhang, Y.; Guo, S.; Pendharkar, A. I.; Lu, M.; Huang, L.; Huang, W.; Han, G. *Small* **2017**, *13*, 1602843.

(67) Zou, W.; Visser, C.; Maduro, J. A.; Pshenichnikov, M. S.; Hummelen, J. C. *Nature Photonics* **2012**, *6*, 560–564.

(68) Shao, W.; Chen, G.; Kuzmin, A.; Kutscher, H. L.; Pliss, A.; Ohulchanskyy, T. Y.; Prasad, P. N. *Journal of the American Chemical Society* **2016**, *138*, 16192–16195.

(69) Zhang, W.; Chen, T.; Su, L.; Ge, X.; Chen, X.; Song, J.; Yang, H. *Analytical Chemistry* **2020**, *92*, 6094–6102.

(70) Song, D.; Chi, S.; Li, X.; Wang, C.; Li, Z.; Liu, Z. *ACS applied materials & interfaces* **2019**, *11*, 41100–41108.

(71) Vogler, A.; Kunkely, H. *Inorganica Chimica Acta* **2006**, *359*, 4130–4138.

(72) Tan, M.; Del Rosal, B.; Zhang, Y.; Rodrıguez, E. M.; Hu, J.; Zhou, Z.; Fan, R.; Ortgies, D. H.; Fernández, N.; Chaves-Coira, I., et al. *Nanoscale* **2018**, *10*, 17771–17780.

(73) Fan, Y.; Wang, P.; Lu, Y.; Wang, R.; Zhou, L.; Zheng, X.; Li, X.; Piper, J. A.; Zhang, F. *Nature nanotechnology* **2018**, *13*, 941–946.

(74) Wu, S.; Han, G.; Milliron, D. J.; Aloni, S.; Altoe, V.; Talapin, D. V.; Cohen, B. E.; Schuck, P. J. *Proceedings of the National Academy of Sciences* **2009**, *106*, 10917–10921.

(75) Dang, X.; Gu, L.; Qi, J.; Correa, S.; Zhang, G.; Belcher, A. M.; Hammond, P. T. *Proceedings of the National Academy of Sciences* **2016**, *113*, 5179–5184.

(76) Qu, Z.; Shen, J.; Li, Q.; Xu, F.; Wang, F.; Zhang, X.; Fan, C. *Theranostics* **2020**, *10*, 2631.

(77) Chernov, K. G.; Redchuk, T. A.; Omelina, E. S.; Verkhusha, V. V. *Chemical reviews* **2017**, *117*, 6423–6446.

(78) Blankenship, R. E. *Antonie van Leeuwenhoek* **1994**, *65*, 311–329.

(79) Fischer, A. J.; Lagarias, J. C. *Proceedings of the National Academy of Sciences* **2004**, *101*, 17334–17339.

(80) Shu, X.; Royant, A.; Lin, M. Z.; Aguilera, T. A.; Lev-Ram, V.; Steinbach, P. A.; Tsien, R. Y. *Science* **2009**, *324*, 804–807.

(81) Auldridge, M. E.; Forest, K. T. *Critical reviews in biochemistry and molecular biology* **2011**, *46*, 67–88.

(82) Auldridge, M. E.; Satyshur, K. A.; Anstrom, D. M.; Forest, K. T. *Journal of Biological Chemistry* **2012**, *287*, 7000–7009.

(83) Zeng, X.; Xiao, Y.; Lin, J.; Li, S.; Zhou, H.; Nong, J.; Xu, G.; Wang, H.; Xu, F.; Wu, J., et al. *Advanced Healthcare Materials* **2018**, *7*, 1800589.

(84) Yu, D.; Gustafson, W. C.; Han, C.; Lafaye, C.; Noirclerc-Savoye, M.; Ge, W.-P.; Thayer, D. A.; Huang, H.; Kornberg, T. B.; Royant, A., et al. *Nature communications* **2014**, *5*, 1–7.

(85) Shcherbakova, D. M.; Verkhusha, V. V. *Nature methods* **2013**, *10*, 751–754.

(86) Piatkevich, K. D.; Subach, F. V.; Verkhusha, V. V. *Nature communications* **2013**, *4*, 1–10.

(87) Matlashov, M. E.; Shcherbakova, D. M.; Alvelid, J.; Baloban, M.; Pennacchietti, F.; Shemetov, A. A.; Testa, I.; Verkhusha, V. V. *Nature communications* **2020**, *11*, 1–12.

(88) Shcherbakova, D. M.; Cox Cammer, N.; Huisman, T. M.; Verkhusha, V. V.; Hodgson, L. *Nature chemical biology* **2018**, *14*, 591–600.

(89) Yu, D.; Baird, M. A.; Allen, J. R.; Howe, E. S.; Klassen, M. P.; Reade, A.; Makhijani, K.; Song, Y.; Liu, S.; Murthy, Z., et al. *Nature methods* **2015**, *12*, 763–765.

(90) Oliinyk, O. S.; Shemetov, A. A.; Pletnev, S.; Shcherbakova, D. M.; Verkhusha, V. V. *Nature communications* **2019**, *10*, 1–13.

(91) Rumyantsev, K. A.; Turoverov, K. K.; Verkhusha, V. V. *Scientific Reports* **2016**, *6*, 1–10.

(92) Kamper, M.; Ta, H.; Jensen, N. A.; Hell, S. W.; Jakobs, S. *Nature communications* **2018**, *9*, 1–7.

(93) Shemetov, A. A.; Oliinyk, O. S.; Verkhusha, V. V. *Cell chemical biology* **2017**, *24*, 758–766.

(94) Donnelly, S. K.; Cabrera, R.; Mao, S. P.; Christin, J. R.; Wu, B.; Guo, W.; Bravo-Cordero, J. J.; Condeelis, J. S.; Segall, J. E.; Hodgson, L. *Journal of Cell Biology* **2017**, *216*, 4331–4349.

(95) Rodriguez, E. A.; Tran, G. N.; Gross, L. A.; Crisp, J. L.; Shu, X.; Lin, J. Y.; Tsien, R. Y. *Nature methods* **2016**, *13*, 763–769.

(96) Shcherbakova, D. M.; Baloban, M.; Emelyanov, A. V.; Brenowitz, M.; Guo, P.; Verkhusha, V. V. *Nature communications* **2016**, *7*, 1–12.

(97) Telford, W. G.; Shcherbakova, D. M.; Buschke, D.; Hawley, T. S.; Verkhusha, V. V. *PloS one* **2015**, *10*, e0122342.

(98) Janssen, A. F.; Tas, R. P.; van Bergeijk, P.; Oost, R.; Hoogenraad, C. C.; Kapitein, L. C. *Frontiers in Cellular Neuroscience* **2017**, *11*, 260.

(99) Piatkevich, K. D.; Suk, H.-J.; Kodandaramaiah, S. B.; Yoshida, F.; DeGennaro, E. M.; Drobizhev, M.; Hughes, T. E.; Desimone, R.; Boyden, E. S.; Verkhusha, V. V. *Biophysical journal* **2017**, *113*, 2299–2309.

(100) Richie, C. T.; Whitaker, L. R.; Whitaker, K. W.; Necarsulmer, J.; Baldwin, H. A.; Zhang, Y.; Fortuno, L.; Hinkle, J. J.; Koivula, P.; Henderson, M. J., et al. *Journal of neuroscience methods* **2017**, *284*, 1–14.

(101) Weinhard, L.; Di Bartolomei, G.; Bolasco, G.; Machado, P.; Schieber, N. L.; Neniskyte, U.; Exiga, M.; Vadisiute, A.; Raggioli, A.; Schertel, A., et al. *Nature communications* **2018**, *9*, 1–14.

(102) Qian, Y.; Piatkevich, K. D.; Mc Larney, B.; Abdelfattah, A. S.; Mehta, S.; Murdock, M. H.; Gottschalk, S.; Molina, R. S.; Zhang, W.; Chen, Y., et al. *Nature methods* **2019**, *16*, 171–174.

(103) Roman, W.; Martins, J. P.; Carvalho, F. A.; Voituriez, R.; Abella, J. V.; Santos, N. C.; Cadot, B.; Way, M.; Gomes, E. R. *Nature cell biology* **2017**, *19*, 1189–1201.

(104) Kaberniuk, A. A.; Shemetov, A. A.; Verkhusha, V. V. *Nature methods* **2016**, *13*, 591–597.

(105) Redchuk, T. A.; Kaberniuk, A. A.; Verkhusha, V. V. *Nature protocols* **2018**, *13*, 1121–1136.

(106) Chu, Y.; Ren, J.; Zhang, J.; Peng, G.; Yang, J.; Wang, P.; Yuan, L. *Scientific reports* **2016**, *6*, 1–9.

(107) Dan, H. K.; Qiu, J.; Zhou, D.; Jiao, Q.; Wang, R.; Le Thai, N. *Materials Letters* **2019**, *234*, 142–147.

(108) Dan, H. K.; Le, D.-N.; Nguyen-Truong, H. T.; Tap, T. D.; Vinh, H. X.; Ty, N. M.; Wang, R.; Zhou, D.; Qiu, J. *Journal of Luminescence* **2020**, *219*, 116942.

(109) Cheng, C.; Wang, F.; Cheng, X. *Optics & Laser Technology* **2020**, *122*, 105812.

(110) Ming, N.; Tao, S.; Yang, W.; Chen, Q.; Sun, R.; Wang, C.; Wang, S.; Man, B.; Zhang, H. *Optics express* **2018**, *26*, 9017–9026.

(111) Cheng, P. K.; Tang, C. Y.; Wang, X. Y.; Ma, S.; Long, H.; Tsang, Y. H. *Scientific Reports* **2019**, *9*, 1–7.

(112) Meng, Y.; Li, Y.; Xu, Y.; Wang, F. *Scientific reports* **2017**, *7*, 1–7.

(113) Fried, N. M.; Irby, P. B. *Nature Reviews Urology* **2018**, *15*, 563–573.

(114) Ren, D.; Ahtapodov, L.; Nilsen, J. S.; Yang, J.; Gustafsson, A.; Huh, J.; Conibeer, G. J.; Van Helvoort, A. T.; Fimland, B.; Weman, H. *Nano letters* **2018**, *18*, 2304–2310.

(115) Chen, S.; Yukimune, M.; Fujiwara, R.; Ishikawa, F.; Chen, W. M.; Buyanova, I. A. *Nano Letters* **2019**, *19*, 885–890.

(116) Wu, J.-J.; Gao, H.; Lai, R.; Zhuo, M.-P.; Feng, J.; Wang, X.-D.; Wu, Y.; Liao, L.-S.; Jiang, L. *Matter* **2020**, *2*, 1233–1243.

(117) Li, Z.; Wang, X.; Liu, S.; Yang, J.; Shi, K.; Wang, H.; Zhu, D.; Xing, X. *Optics & Laser Technology* **2018**, *99*, 81–85.

(118) Zheng, D.; Fang, H.; Long, M.; Wu, F.; Wang, P.; Gong, F.; Wu, X.; Ho, J. C.; Liao, L.; Hu, W. *ACS nano* **2018**, *12*, 7239–7245.

(119) Ma, Z.; Chai, S.; Feng, Q.; Li, L.; Li, X.; Huang, L.; Liu, D.; Sun, J.; Jiang, R.; Zhai, T., et al. *Small* **2019**, *15*, 1805307.

(120) Convertino, A.; Mussi, V.; Maiolo, L.; Ledda, M.; Lolli, M. G.; Bovino, F. A.; Fortunato, G.; Rocchia, M.; Lisi, A. *Nanotechnology* **2018**, *29*, 415102.

(121) Hu, Y.; Yu, Y.-J.; Yuan, Y.; Jiang, Z.-Q.; Liao, L.-s. *Advanced Optical Materials* **2020**, *8*, 1901917.

(122) Zhang, Y.; Li, Q.; Cai, M.; Xue, J.; Qiao, J. *Journal of Materials Chemistry C* **2020**, *8*, 8484–8492.

(123) Wei, Y.-C.; Wang, S. F.; Hu, Y.; Liao, L.-S.; Chen, D.-G.; Chang, K.-H.; Wang, C.-W.; Liu, S.-H.; Chan, W.-H.; Liao, J.-L., et al. *Nature Photonics* **2020**, *14*, 570–577.

(124) Shao, Q.; Ding, H.; Yao, L.; Xu, J.; Liang, C.; Jiang, J. *RSC advances* **2018**, *8*, 12035–12042.

(125) Shao, Q.; Ding, H.; Yao, L.; Xu, J.; Liang, C.; Li, Z.; Dong, Y.; Jiang, J. *Optics Letters* **2018**, *43*, 5251–5254.

(126) Xu, X.; Shao, Q.; Yao, L.; Dong, Y.; Jiang, J. *Chemical Engineering Journal* **2020**, *383*, 123108.

(127) Rajendran, V.; Lesniewski, T.; Mahlik, S.; Grinberg, M.; Leniec, G.; Kaczmarek, S. M.; Pang, W.-K.; Lin, Y.-S.; Lu, K.-M.; Lin, C.-M., et al. *Acs Photonics* **2019**, *6*, 3215–3224.

(128) Basore, E. T.; Xiao, W.; Liu, X.; Wu, J.; Qiu, J. *Advanced Optical Materials* **2020**, *8*, 2000296.

(129) Lai, S.; Zhao, M.; Qiao, J.; Molokeev, M. S.; Xia, Z. *The Journal of Physical Chemistry Letters* **2020**, *11*, 5680–5685.

(130) Tang, Z.; Zhang, Q.; Cao, Y.; Li, Y.; Wang, Y. *Chemical Engineering Journal* **2020**, *388*, 124231.

(131) Gao, Z.; Danné, N.; Godin, A. G.; Lounis, B.; Cognet, L. *Nanomaterials* **2017**, *7*, 393.

(132) Godin, A. G.; Setaro, A.; Gandil, M.; Haag, R.; Adeli, M.; Reich, S.; Cognet, L. *Science advances* **2019**, *5*, eaax1166.

(133) Jin, D.; Xi, P.; Wang, B.; Zhang, L.; Enderlein, J.; van Oijen, A. M. *Nature methods* **2018**, *15*, 415–423.

(134) Khush, G.; Virk, P., *IR Varieties and Their Impact*; International Rice Research Institute: 2005.

(135) Altpeter, F.; Springer, N. M.; Bartley, L. E.; Blechl, A. E.; Brutnell, T. P.; Citovsky, V.; Conrad, L. J.; Gelvin, S. B.; Jackson, D. P.; Kausch, A. P., et al. *The Plant Cell* **2016**, *28*, 1510–1520.

(136) Mahfouz, M. M.; Piatek, A.; Stewart Jr, C. N. *Plant biotechnology journal* **2014**, *12*, 1006–1014.

(137) Hamilton, J. R.; Doudna, J. A. *Science* **2020**, *367*, 976–977.

(138) Staahl, B. T.; Benekareddy, M.; Coulon-Bainier, C.; Banfal, A. A.; Floor, S. N.; Sabo, J. K.; Urnes, C.; Munares, G. A.; Ghosh, A.; Doudna, J. A. *Nature biotechnology* **2017**, *35*, 431–434.

(139) Lee, K.; Conboy, M.; Park, H. M.; Jiang, F.; Kim, H. J.; Dewitt, M. A.; Mackley, V. A.; Chang, K.; Rao, A.; Skinner, C., et al. *Nature biomedical engineering* **2017**, *1*, 889–901.

(140) Martin-Ortigosa, S.; Peterson, D. J.; Valenstein, J. S.; Lin, V. S.-Y.; Trewyn, B. G.; Lyznik, L. A.; Wang, K. *Plant physiology* **2014**, *164*, 537–547.

(141) Demirer, G. S.; Zhang, H.; Matos, J. L.; Goh, N. S.; Cunningham, F. J.; Sung, Y.; Chang, R.; Aditham, A. J.; Chio, L.; Cho, M.-J., et al. *Nature nanotechnology* **2019**, *14*, 456–464.

(142) Kwak, S.-Y.; Lew, T. T. S.; Sweeney, C. J.; Koman, V. B.; Wong, M. H.; Bohmert-Tatarev, K.; Snell, K. D.; Seo, J. S.; Chua, N.-H.; Strano, M. S. *Nature nanotechnology* **2019**, *14*, 447–455.

(143) Demirer, G. S.; Zhang, H.; Goh, N. S.; Pinals, R. L.; Chang, R.; Landry, M. P. *Science advances* **2020**, *6*, eaaz0495.

(144) Zhang, Y.; Malzahn, A. A.; Sretenovic, S.; Qi, Y. *Nature Plants* **2019**, *5*, 778–794.

(145) Liang, Z.; Chen, K.; Li, T.; Zhang, Y.; Wang, Y.; Zhao, Q.; Liu, J.; Zhang, H.; Liu, C.; Ran, Y., et al. *Nature communications* **2017**, *8*, 1–5.

(146) Woo, J. W.; Kim, J.; Kwon, S. I.; Corvalán, C.; Cho, S. W.; Kim, H.; Kim, S.-G.; Kim, S.-T.; Choe, S.; Kim, J.-S. *Nature biotechnology* **2015**, *33*, 1162–1164.

(147) Svitashev, S.; Schwartz, C.; Lenderts, B.; Young, J. K.; Mark Cigan, A. *Nature communications* **2016**, *7*, 1–7.

(148) Ellison, E. E.; Nagalakshmi, U.; Gamo, M. E.; Huang, P.-j.; Dinesh-Kumar, S.; Voytas, D. F. *Nature plants* **2020**, *6*, 620–624.

(149) Zhu, H.; Li, C.; Gao, C. *Nature Reviews Molecular Cell Biology* **2020**, *21*, 661–677.

(150) Gordon-Kamm, B.; Sardesai, N.; Arling, M.; Lowe, K.; Hoerster, G.; Betts, S.; Jones, T. *Plants* **2019**, *8*, 38.

(151) Lowe, K.; Wu, E.; Wang, N.; Hoerster, G.; Hastings, C.; Cho, M.-J.; Scelonge, C.; Lenderts, B.; Chamberlin, M.; Cushatt, J., et al. *The Plant Cell* **2016**, *28*, 1998–2015.

(152) Maher, M. F.; Nasti, R. A.; Vollbrecht, M.; Starker, C. G.; Clark, M. D.; Voytas, D. F. *Nature biotechnology* **2020**, *38*, 84–89.

(153) Eeckhaut, T.; Lakshmanan, P. S.; Deryckere, D.; Van Bockstaele, E.; Van Huylenbroeck, J. *Planta* **2013**, *238*, 991–1003.

(154) Zafar, K.; Sedeek, K. E.; Rao, G. S.; Khan, M. Z.; Amin, I.; Kamel, R.; Mukhtar, Z.; Zafar, M.; Mansoor, S.; Mahfouz, M. M. *Frontiers in Genome Editing* **2020**, *2*, 5.

(155) Komor, A. C.; Kim, Y. B.; Packer, M. S.; Zuris, J. A.; Liu, D. R. *Nature* **2016**, *533*, 420–424.

(156) Lin, Q.; Zong, Y.; Xue, C.; Wang, S.; Jin, S.; Zhu, Z.; Wang, Y.; Anzalone, A. V.; Raguram, A.; Doman, J. L., et al. *Nature biotechnology* **2020**, *38*, 582–585.

(157) Yin, X.; Biswal, A. K.; Dionora, J.; Perdigon, K. M.; Balahadia, C. P.; Mazumdar, S.; Chater, C.; Lin, H.-C.; Coe, R. A.; Kretzschmar, T., et al. *Plant cell reports* **2017**, *36*, 745–757.

(158) Hsu, P. D.; Scott, D. A.; Weinstein, J. A.; Ran, F. A.; Konermann, S.; Agarwala, V.; Li, Y.; Fine, E. J.; Wu, X.; Shalem, O., et al. *Nature biotechnology* **2013**, *31*, 827–832.

(159) Jinek, M.; East, A.; Cheng, A.; Lin, S.; Ma, E.; Doudna, J. *elife* **2013**, *2*, e00471.

(160) Naim, F.; Shand, K.; Hayashi, S.; O'Brien, M.; McGree, J.; Johnson, A. A.; Dugdale, B.; Waterhouse, P. M. *PLoS One* **2020**, *15*, e0227994.

(161) Arndell, T.; Sharma, N.; Langridge, P.; Baumann, U.; Watson-Haigh, N. S.; Whitford, R. *BMC biotechnology* **2019**, *19*, 1–12.

(162) Liang, Y.; Eudes, A.; Yogiswara, S.; Jing, B.; Benites, V. T.; Yamanaka, R.; Cheng-Yue, C.; Baidoo, E. E.; Mortimer, J. C.; Scheller, H. V., et al. *Biotechnology for biofuels* **2019**, *12*, 1–15.

(163) Rhee, S. Y.; Mutwil, M. *Trends in plant science* **2014**, *19*, 212–221.

(164) Kersey, P. J. *Current opinion in plant biology* **2019**, *48*, 1–8.

(165) Hrbáčková, M.; Dvořák, P.; Takáč, T.; Tichá, M.; Luptovčiak, I.; Šamajová, O.; Ovečka, M.; Šamaj, J. *Frontiers in plant science* **2020**, 592.

(166) Ladics, G. S.; Bartholomaeus, A.; Bregitzer, P.; Doerrer, N. G.; Gray, A.; Holzhauser, T.; Jordan, M.; Keese, P.; Kok, E.; Macdonald, P., et al. *Transgenic Research* **2015**, *24*, 587–603.

(167) Torney, F.; Trewyn, B. G.; Lin, V. S.-Y.; Wang, K. *Nature nanotechnology* **2007**, *2*, 295–300.

(168) Mitter, N.; Worrall, E. A.; Robinson, K. E.; Li, P.; Jain, R. G.; Taochy, C.; Fletcher, S. J.; Carroll, B. J.; Lu, G.; Xu, Z. P. *Nature plants* **2017**, *3*, 1–10.

(169) Zhang, H.; Demirer, G. S.; Zhang, H.; Ye, T.; Goh, N. S.; Aditham, A. J.; Cunningham, F. J.; Fan, C.; Landry, M. P. *Proceedings of the National Academy of Sciences* **2019**, *116*, 7543–7548.

(170) Thagun, C.; Chuah, J.-A.; Numata, K. *Advanced Science* **2019**, *6*, 1902064.

(171) Santana, I.; Wu, H.; Hu, P.; Giraldo, J. P. *Nature communications* **2020**, *11*, 1–12.

(172) Hu, P.; An, J.; Faulkner, M. M.; Wu, H.; Li, Z.; Tian, X.; Giraldo, J. P. *ACS nano* **2020**, *14*, 7970–7986.

(173) Nguyen, D. N.; Roth, T. L.; Li, P. J.; Chen, P. A.; Apathy, R.; Mamedov, M. R.; Vo, L. T.; Tobin, V. R.; Goodman, D.; Shifrut, E., et al. *Nature biotechnology* **2020**, *38*, 44–49.

(174) Diez, P.; Sanchez, A.; Torre, C. d. l.; Gamella, M.; Martınez-Ruız, P.; Aznar, E.; Martinez-Manez, R.; Pingarron, J. M.; Villalonga, R. *ACS Applied Materials & Interfaces* **2016**, *8*, 7657–7665.

(175) Su, Y.; Ashworth, V.; Kim, C.; Adeleye, A. S.; Rolshausen, P.; Roper, C.; White, J.; Jassby, D. *Environmental Science: Nano* **2019**, *6*, 2311–2331.

(176) Du, W.; Sun, Y.; Ji, R.; Zhu, J.; Wu, J.; Guo, H. *Journal of Environmental Monitoring* **2011**, *13*, 822–828.

(177) Al-Salim, N.; Barraclough, E.; Burgess, E.; Clothier, B.; Deurer, M.; Green, S.; Malone, L.; Weir, G. *Science of the total environment* **2011**, *409*, 3237–3248.

(178) Zhu, Z.-J.; Wang, H.; Yan, B.; Zheng, H.; Jiang, Y.; Miranda, O. R.; Rotello, V. M.; Xing, B.; Vachet, R. W. *Environmental science & technology* **2012**, *46*, 12391–12398.

(179) Milewska-Hendel, A.; Zubko, M.; Karcz, J.; Stróż, D.; Kurczyńska, E. *Scientific Reports* **2017**, *7*, 1–13.

(180) Cunningham, F. J.; Goh, N. S.; Demirer, G. S.; Matos, J. L.; Landry, M. P. *Trends in biotechnology* **2018**, *36*, 882–897.

(181) *Genetically Engineered Crops: Experiences and Prospects*; tech. rep.; National Academies of Sciences, Engineering, and Medicine, 2016.

(182) Prado, J. R.; Segers, G.; Voelker, T.; Carson, D.; Dobert, R.; Phillips, J.; Cook, K.; Cornejo, C.; Monken, J.; Grapes, L., et al. *Annual review of plant biology* **2014**, *65*, 769–790.

(183) *Importation, Interstate Movement, and Environmental Release of Certain Genetically Engineered Organisms*; tech. rep.; Animal and Plant Health Inspection Service, USDA, 2017.

(184) Waltz, E. *Nature biotechnology* **2018**, *36*, 6–8.

(185) Gupta, M.; Gerard, M.; Padmaja, S. S.; Sastry, R. K. *World Patent Information* **2020**, *60*, 101944.

(186) Zhang, D.; Hussain, A.; Manghwar, H.; Xie, K.; Xie, S.; Zhao, S.; Larkin, R. M.; Qing, P.; Jin, S.; Ding, F. *Plant biotechnology journal* **2020**, *18*, 1651–1669.

(187) Callaway, E. *Nature* **2018**, *560*, 16–17.

(188) Holme, I. B.; Gregersen, P. L.; Brinch-Pedersen, H. *Frontiers in Plant Science* **2019**, *10*, 1468.

(189) Kostarelos, K. *Nature biotechnology* **2008**, *26*, 774–776.

(190) Pikula, K.; Chaika, V.; Zakharenko, A.; Markina, Z.; Vedyagin, A.; Kuznetsov, V.; Gusev, A.; Park, S.; Golokhvast, K. *Nanomaterials* **2020**, *10*, 485.

(191) Kermanizadeh, A.; Gosens, I.; MacCalman, L.; Johnston, H.; Danielsen, P. H.; Jacobsen, N. R.; Lenz, A.-G.; Fernandes, T.; Schins, R. P.; Cassee, F. R., et al. *Journal of Toxicology and Environmental Health, Part B* **2016**, *19*, 1–28.

(192) Heller, D. A.; Jena, P. V.; Pasquali, M.; Kostarelos, K.; Delogu, L. G.; Meidl, R. E.; Rotkin, S. V.; Scheinberg, D. A.; Schwartz, R. E.; Terrones, M., et al. *Nature nanotechnology* **2020**, *15*, 164–166.

(193) Silva, A. T.; Nguyen, A.; Ye, C.; Verchot, J.; Moon, J. H. *BMC plant biology* **2010**, *10*, 1–14.

(194) Finiuk, N.; Buziashvili, A.; Burlaka, O.; Zaichenko, A.; Mitina, N.; Miagkota, O.; Lobachevska, O.; Stoika, R.; Blume, Y.; Yemets, A. *Plant Cell, Tissue and Organ Culture (PCTOC)* **2017**, *131*, 27–39.

(195) Lakshmanan, M.; Kodama, Y.; Yoshizumi, T.; Sudesh, K.; Numata, K. *Biomacromolecules* **2013**, *14*, 10–16.

(196) Akinc, A.; Thomas, M.; Klibanov, A. M.; Langer, R. *The Journal of Gene Medicine: A cross-disciplinary journal for research on the science of gene transfer and its clinical applications* **2005**, *7*, 657–663.

(197) Sharma, V. K.; Thomas, M.; Klibanov, A. M. *Biotechnology and bioengineering* **2005**, *90*, 614–620.

(198) Putnam, D.; Gentry, C. A.; Pack, D. W.; Langer, R. *Proceedings of the National Academy of Sciences* **2001**, *98*, 1200–1205.

(199) Thomas, M.; Ge, Q.; Lu, J. J.; Chen, J.; Klibanov, A. *Pharmaceutical research* **2005**, *22*, 373–380.

(200) Thomas, M.; Lu, J. J.; Zhang, C.; Chen, J.; Klibanov, A. M. *Pharmaceutical research* **2007**, *24*, 1564–1571.

(201) Grant, E. V.; Thomas, M.; Fortune, J.; Klibanov, A. M.; Letvin, N. L. *European journal of immunology* **2012**, *42*, 2937–2948.

(202) Thomas, M.; Klibanov, A. M. *Proceedings of the National Academy of Sciences* **2002**, *99*, 14640–14645.

(203) Thomas, M.; Klibanov, A. M. *Proceedings of the National Academy of Sciences* **2003**, *100*, 9138–9143.

(204) Song, W.-J.; Du, J.-Z.; Sun, T.-M.; Zhang, P.-Z.; Wang, J. *Small* **2010**, *6*, 239–246.

(205) Wong, M. H.; Misra, R. P.; Giraldo, J. P.; Kwak, S.-Y.; Son, Y.; Landry, M. P.; Swan, J. W.; Blankschtein, D.; Strano, M. S. *Nano letters* **2016**, *16*, 1161–1172.

(206) Lew, T. T. S.; Park, M.; Wang, Y.; Gordiichuk, P.; Yeap, W.-C.; Mohd Rais, S. K.; Kulaveerasingam, H.; Strano, M. S. *ACS Materials Letters* **2020**, *2*, 1057–1066.

(207) Wang, J. W.; Cunningham, F. J.; Goh, N. S.; Boozarpour, N. N.; Pham, M.; Landry, M. P. *Current opinion in plant biology* **2021**, *60*, 102052.

(208) Demirer, G. S.; Zhang, H.; Goh, N. S.; González-Grandıo, E.; Landry, M. P. *Nature Protocols* **2019**, *14*, 2954–2971.

(209) Chio, L.; Pinals, R. L.; Murali, A.; Goh, N. S.; Landry, M. P. *Advanced Functional Materials* **2020**, *30*, 1910556.

(210) Wang, F.; Deng, K.-J.; Zhou, L.; Zhao, J.-B.; Ke, X.-H.; Wen, L.-L. *Journal of Inorganic and Organometallic Polymers and Materials* **2012**, *22*, 1182–1188.

(211) Intrchom, W.; Thakkar, M.; Hamilton, R. F.; Holian, A.; Mitra, S. *Scientific reports* **2018**, *8*, 1–11.

(212) Skalar, T.; Jelen, E.; Novosel, B.; Marinšek, M. *Journal of Thermal Analysis and Calorimetry* **2017**, *127*, 265–271.

(213) Tchoul, M. N.; Ford, W. T.; Lolli, G.; Resasco, D. E.; Arepalli, S. *Chemistry of Materials* **2007**, *19*, 5765–5772.

(214) Rinaldi, A.; Frank, B.; Su, D. S.; Hamid, S. B. A.; Schlögl, R. *Chemistry of Materials* **2011**, *23*, 926–928.

(215) Shao, L.; Tobias, G.; Salzmann, C. G.; Ballesteros, B.; Hong, S. Y.; Crossley, A.; Davis, B. G.; Green, M. L. *Chemical Communications* **2007**, 5090–5092.

(216) Hu, H.; Zhao, B.; Itkis, M. E.; Haddon, R. C. *The Journal of Physical Chemistry B* **2003**, *107*, 13838–13842.

(217) González-Grandıo, E.; Demirer, G. S.; Jackson, C. T.; Yang, D.; Ebert, S.; Molawi, K.; Keller, H.; Landry, M. P. *Journal of nanobiotechnology* **2021**, *19*, 1–15.

(218) Ziebarth, J. D.; Wang, Y. *Biomacromolecules* **2010**, *11*, 29–38.

(219) Pompeo, F.; Resasco, D. E. *Nano letters* **2002**, *2*, 369–373.

(220) Pinals, R. L.; Yang, D.; Rosenberg, D. J.; Chaudhary, T.; Crothers, A. R.; Iavarone, A. T.; Hammel, M.; Landry, M. P. *Angewandte Chemie International Edition* **2020**, *59*, 23668–23677.

(221) Pinals, R. L.; Yang, D.; Lui, A.; Cao, W.; Landry, M. P. *Journal of the American Chemical Society* **2019**, *142*, 1254–1264.

(222) Strojan, K.; Lojk, J.; Bregar, V. B.; Veranič, P.; Pavlin, M. *Toxicology in Vitro* **2017**, *41*, 12–20.

(223) Goodin, M. M.; Zaitlin, D.; Naidu, R. A.; Lommel, S. A. *Molecular plant-microbe interactions* **2008**, *21*, 1015–1026.

(224) Ohshima, M.; Itoh, H.; Matsuoka, M.; Murakami, T.; Ohashi, Y. *The plant cell* **1990**, *2*, 95–106.

(225) Amor, B. B.; Wirth, S.; Merchan, F.; Laporte, P.; d'Aubenton-Carafa, Y.; Hirsch, J.; Maizel, A.; Mallory, A.; Lucas, A.; Deragon, J. M., et al. *Genome research* **2009**, *19*, 57–69.

(226) Jackson, C. T.; Wang, J. W.; González-Grandıo, E.; Goh, N. S.; Mun, J.; Krishnan, S.; Geyer, F. L.; Keller, H.; Ebert, S.; Molawi, K., et al. *ACS nano* **2021**.

(227) Wieland, J. A.; Houchin-Ray, T. L.; Shea, L. D. *Journal of Controlled Release* **2007**, *120*, 233–241.

(228) Ali, Z.; Serag, M. F.; Demirer, G. S.; Torre, B.; di Fabrizio, E.; Landry, M. P.; Habuchi, S.; Mahfouz, M. *ACS Applied Nano Materials* **2022**.

(229) Beals, N.; Kasibhatla, N.; Basu, S. *ACS Applied Bio Materials* **2019**, *2*, 717–727.

(230) Beals, N.; Thiagarajan, P. S.; Soehnlen, E.; Das, A.; Reizes, O.; Lathia, J. D.; Basu, S. *ACS omega* **2017**, *2*, 7702–7713.

(231) (AFBF), A. F. B. F. Fast Facts About Agriculture Food. https://www.fb.org/newsroom/fast-facts (accessed 09/30/2020).

(232) Department of Agriculture, A.; (APHIS), P. H. I. S. Final Rule: Movement of Certain Genetically Engineered Organisms., https://www.govinfo.gov/content/pkg/FR-2020-05-18/pdf/2020-10638.pdf, Accessed: 2020-09-30, 2020.

(233) Kuzma, J. *Issues in Science and Technology* **2018**, *35*, 80–85.

(234) For International Food, B.; Agricultural Development (BIFAD) International Food Policy Research Institute (IFPRI), A. o. P.; (APLU), L.-G. U. *How the United States benefits from agricultural and food security investments in developing countries*; tech. rep.; International Food Policy Research Institute, 2019.

(235) James, C. ISAAA Briefs brief 49 Global Status of Commercialized Biotech/GM Crops: 2014., 2014.

(236) Qaim, M. *Annu. Rev. Resour. Econ.* **2009**, *1*, 665–694.

(237) Smyth, S. J.; McDonald, J.; Falck-Zepeda, J. *GM Crops & Food* **2014**, *5*, 44–57.

(238) Schmidt, S. M.; Belisle, M.; Frommer, W. B. *EMBO reports* **2020**, *21*, e50680.

(239) Potrykus, I. *Nature* **2010**, *466*, 561–561.

(240) Waltz, E. *Nature Biotechnology* **2019**, 1251–1253.

(241) Of the President (EOP), E. O. Modernizing the Regulatory System for Biotechnology Products: Final Version of the 2017 Update to the coordinated Framework for Regulation of Biotechnology., https://obamawhitehouse.archives.gov/sites/default/files/microsites/ostp/2017_coordinated_framework_update.pdf, Accessed: 2020-09-30, 2017.

(242) Of the President (EOP), E. O. Executive Order on Modernizing the Regulatory Framework for Agricultural Biotechnology Products Declared by Executive Order No.13874 of June 11, 2019., https://www.federalregister.gov/documents/2019/06/14/2019-12802/modernizing-the-regulatory-framework-for-agricultural-biotechnology-products, Accessed: 2020-09-30, 2019.

(243) USDA, F.; EPA The Unified Website for Biotechnology Regulation. https://www.fb.org/newsroom/fast-facts (accessed 09/30/2020).

(244) Department of Agriculture, A.; (APHIS), P. H. I. S. Proposed Rule: Movement of Certain Genetically Engineered Organisms., https://www.govinfo.gov/content/pkg/FR-2019-06-06/pdf/2019-11704.pdf, Accessed: 2020-09-30, 2019.

(245) Kuzma, J. USDA Oversight Past to Present., https://mediasite.wolfware.ncsu.edu/online/Channel/ges-center/watch/dfb1f865e8e84f108a29c915b94116cc1d, 2020.

(246) *Congress's Authority to Influence and Control Executive Branch Agencies*; tech. rep.; Congressional Research Service, 2018.

(247) Of the President (EOP), E. O. National Strategy for Modernizing the Regulatory System for Biotechnology Products., `https://www.fda.gov/media/102667/download`, Accessed: 2020-09-30, 2016.